Preparation and Characterization of Activated Biochar for Lithium-Sulfur Battery Application

by

Sourov Kar Sajib

A thesis submitted to the Graduate Faculty of
Auburn University
in partial fulfillment of the
requirements for the Degree of
Master of Science

Auburn, Alabama
December 16, 2017

Keywords: Activated biochar, Li-S battery, Pyrolysis

Approved by

Sushil Adhikari, Chair, Professor of Biosystems Engineering
James Radich, Assistant Professor of Chemical Engineering
Timothy McDonald, Professor of Biosystems Engineering
Xinyu Zhang, Associate Professor of Chemical Engineering

Abstract

Utilization of low-value, abundant and sustainable biomass materials for high-value energy storage application was the main goal of this thesis. Energy storage for vehicle electrification and intermittent renewable energy sources such as solar and wind energy made it an urgent necessity to look for next generation energy storage beyond lithium-ion batteries. Lithium-sulfur (Li-S) battery is one of the most promising candidates for the next generation energy storage solutions due to its high theoretical specific capacity (1675 mAh g^{-1}), high energy density (2567Wh kg^{-1}) and low-cost. However, the commercialization of this battery has been hindered due to several reasons such as the insulating nature of sulfur, intermediate polysulfide dissolution, low Coulombic efficiency and short cycle life. Confining sulfur and polysulfides using porous and conductive carbon materials have gained wide attention to improve Li-S battery performance. Porous carbon structures can physically adsorb sulfur molecule and prevent polysulfide dissolution, whereas nitrogen doping can adsorb polysulfides chemically to improve the Li-S battery performance. Biochar is a carbon-rich, inexpensive and porous material produced as a by-product during biomass pyrolysis for bio-oil production. Being highly porous, carbon-rich and conductive make activated biochar an excellent candidate to be used for sulfur-carbon (S/C) cathode composite.

This thesis work was performed focusing on two objectives. The first objective was to investigate the influence of biomass pyrolysis method on physical and chemical properties of chemically activated biochar/carbon. The second goal was to utilize fast pyrolysis biochar derived from inexpensive and abundant canola meal and Douglas-fir wood for the preparation of high-valued lithium-sulfur battery cathode composite. Fast pyrolysis biochar is obtained as a low-value byproduct of high-valued liquid fuel through fast pyrolysis of biomass. Some studies with biomass biochar have been performed for lithium sulfur battery. However, fast pyrolysis derived biochar has rarely investigated for any battery application. Additionally, the protein content of canola meal biomass acts as a source of natural nitrogen-doping of activated biochar. Thus, our focus was on investigating the applicability of fast pyrolysis biochar for Li-S battery and to compare the performance with slow pyrolysis biochar and commercial conductive carbon black.

For achieving the goals, biochars were prepared using fast pyrolysis and slow pyrolysis method with canola meal and Douglas-fir wood at 500°C temperature. The biochars were further activated using potassium hydroxide (KOH) at 800°C temperature as KOH activation enhanced the carbon content, surface area and pore volume of the activated biochars. Total four types of activated biochars were prepared from two biomass such as CF-AB, CS-AB, DF-AB, and DS-AB. CF-AB and DF-AB were the activated biochars derived from fast pyrolysis biochar of canola meal

and Douglas-fir wood, respectively. CS-AB and DS-AB were the activated biochars derived from slow pyrolysis of canola meal and Douglas-fir wood, respectively.

Physical and chemical characterizations were performed to evaluate physical and chemical characteristics of the samples (moisture content measurement, elemental analysis, thermogravimetric analysis for ash content and sulfur loading measurement, Raman and FTIR spectroscopy, scanning electron microscopy, and surface area and porosity analysis). CF-AB, CS-AB, and DF-AB activated biochars were selected based on the surface area and pore volume to synthesize S/C composite following melt-diffusion strategy at 155°C. For comparison, S/C composite was synthesized by following the same method using commercial conductive carbon black (CB). Samples were denoted as CF-AB-S, CS-AB-S, DF-AB-S, and CB-S. Additionally, CF-AB-S was washed with toluene to remove the sulfur that existed on the surface of CF-AB-S composite and developed another composite named as CF-AB-S-T. For electrochemical characterizations, such as galvanostatic charge-discharge measurement and cyclic voltammetry, lithium-sulfur cells were assembled in 2032 coin cells. Lithium chips and S/C composites were used as anode and cathode materials, respectively.

Activated biochars derived from fast pyrolysis biochars exhibited significantly higher surface area (3355-3277 $m^2 g^{-1}$) and pore volume (1.58-1.49 $cm^3 g^{-1}$) in comparison to activated biochars derived from slow pyrolysis biochars. CF-AB-S-T cathode composite exhibited superior initial discharge capacity of 1507 mAh g^{-1} at the 0.05 C rate (83.75 mA g^{-1}). All the prepared five cells had exhibited initial discharge capacity higher than 1000 mAh g^{-1} at the 0.05 C rate. Activated biochar derived S/C composite cathodes exhibited stable performance at 40^{th} cycle, and even at the very high 2 C rate. These results indicated the applicability of canola meal and Douglas-fir derived activated biochar as cathode material for Li-S battery and excellent potential of fast pyrolysis derived biochars.

Dedicated to them whom I miss the most

Dedicated to

Abhimanyu, Baba, and Chotomama

Acknowledgments

I would like to express my appreciation and gratitude to everyone who has helped me to complete my thesis work. The last two years that I have spent at Auburn University was one of the most enriching experiences of my life. I consider myself blessed and thankful to have Dr. Sushil Adhikari as my mentor and supervisor, who motivated, guided and supported extraordinarily through tough personal and professional time during my M.S. pursuit. I would also like to thank Dr. James Radich and Dr. Majid Beidaghi for their guidance and allowing me to work in their lab to assemble and test coin cells. I am grateful to Dr. Xinyu Zhang, who have inspired and guided me exceptionally through his classes and our conversation outside of the class. I would also like to thank Dr. Timothy McDonald for his time, interest and thoughtful comments. I would also like to thank Dr. Carlos Carrero, Dr. Matthew Waters, Dr. Brian Via and Dr. Michael Miller to provide the instrument support that was crucial to finish the thesis work.

I am especially grateful to Dr. Saravanan Ramiah Shanmugam, Dr. Hyungseok Nam, Dr. Zhouhong Wang and Mr. Ujjain Pradhan for their invaluable support, time and guidance throughout my thesis work. I greatly appreciate the help, time and advice I have received from Rohit, Armin, Alex, Lixia, and Jorge to complete my research work. I have a great appreciation for all my colleagues in the Biosystems Engineering Department, especially for Sanjeev, Rajdeep, Vivek, Khalida, Thomas, Anshu, and Dr. Narendra Sadhwani.

Finally, I would like to thank my family for their constant guidance and support. I am grateful to my parents, Mrs. Molina Rani Dey and Late Sankar Kumar Kar, for guiding me, for being my constant source of inspiration and supporting me to become who I am today. I am also thankful to my parents-in-law, Mrs. Rekharani Sarma and Mr. Deb Kumar Sarma, for their tremendous support and inspiration. I do not have enough words to express my gratitude my beloved wife, Saptarshi Sarma, for encouraging and supporting me through all the tough moments, and for bringing so much happiness to my life. Without their guidance and support, none of my achievements would be possible.

Table of Contents

List of Tables

List of Figures

List of Abbreviations

%	Weight percentage, unless specified otherwise
BET	Brunauer–Emmett–Teller
C	Carbon
Cl	Chlorine
C-BM	Canola meal biomass
CF-BC	Fast pyrolysis biochar from canola meal
CS-BC	Slow pyrolysis biochar from canola meal
CF-AB	Activated biochar from CF-BC using KOH
CF-ABZ	Activated biochar from CF-BC using $ZnCl_2$
CS-AB	Activated biochar from CS-BC using KOH
CB	Carbon Black, Super-P
CF-AB-S	Composite of CF-AB and sulfur
CF-AB-S-T	CF-AB-S washed with toluene
CS-AB-S	Composite of CS-AB and sulfur
CB-S	Composite of CB and sulfur
DF-AB-S	Composite of DF-AB and sulfur
D-BM	Douglas-fir biomass
DF-BC	Fast pyrolysis biochar from Douglas-fir
DF-AB	Activated biochar from DF-BC using KOH
DS-AB	Activated biochar from DS-BC using KOH
DF-BC	Slow pyrolysis biochar from Douglas-fir
DFT	Density functional theory

Eq	Equation
F	Farad (Unit of Capacitance)
h	Hour
HCl	Hydrochloric acid
kg	Kilogram
KOH	Potassium hydroxide
LIB	Lithium-ion battery
Li	Lithium
LPM	Liter per minute
MC	Moisture Content
min	Minute
ml	Milliliter or 10^{-3} liter
N	Nitrogen
NL-DFT	Non-local density functional theory
nm	Nanometer or 10^{-9} m
PSD	Pore size distribution
PV	Pore volume
RT	Room temperature
STP	Standard temperature (273 K) and pressure (1 atm)
S	Sulfur
S/C composite	Sulfur and carbon (either activated biochar or carbon black) composite
SEM	Scanning Electron Microscopy
SSA	Specific surface area

TGA	Thermogravimetric Analysis
Wh	Watt-hours
$ZnCl_2$	Zinc chloride

CHAPTER 1: INTRODUCTION

The rationale for the research work performed in this thesis is discussed in the beginning of this chapter. The motivation behind selecting the biomass sources, biochar preparation method and application of prepared activated biochar is discussed. The research objectives and goals are presented in the latter part of this chapter. Finally, the structure of the thesis is presented in the last section of this chapter.

1.1 RATIONALE FOR THE RESEARCH

Humanity is now facing two emerging problems. The first one is the predictable depletion of fossil fuels and the growing severe energy crisis. The second one is the global climate changes due to increased utilization of fossil fuels. The recent steady economic development in China, India and other southeastern Asian countries has increased the severity of these problems. In order to solve these problems, renewable and sustainable energy sources have gained wide interest to produce energy and clean fuel. For decades, various types of renewable and sustainable energy sources are explored and investigated to be prepared for the future energy and environmental crisis. Among them, biomass is the only renewable and sustainable source to produce liquid fuels and chemicals. Biomass-derived energy possesses carbon neutral cycle. During power generation from biomass, CO_2 consumed during photosynthesis process is recycled into the atmosphere resulting net zero carbon emissions. With the sustainable supply of biomass, the carbon neutral cycles resolve the environmental challenges CO_2 emissions produced from fossil fuel. The

thermochemical conversion of biomass has gained important attraction as a platform for economically producing energy and chemicals from bio-renewable and sustainable resources recently. The composition of these biomass derived products varies with reaction conditions (such as temperature, heating rate, and heating method), and includes non-condensable gases (syngas or producer gas), condensable vapors/liquids (bio-oil and tar), and solids (char and ash).

Biochar or char is a carbon-rich solid residue material obtained from the thermochemical reactions of biomass under oxygen-limited environment [1–6]. Biochar is an excellent precursor for preparation of activated carbon. Thousands of investigations have been performed on conversion of various biomass sources to activated carbons using different pre-treatment and activation conditions. Two of the most common biochar preparation methods are slow pyrolysis and fast pyrolysis. Numerous investigations have been performed on studies of preparation of activated carbon using slow pyrolysis and fast pyrolysis biochar. However, no comparative studies have been found on the influence of these pyrolysis processes on physisorption properties (such as surface area, pore volume, and pore size distribution) of activated carbon. In adsorption studies (such as heavy metal adsorption, odor adsorption, and industrial contaminant adsorption) and energy storage application (such as supercapacitor, lithium batteries and sodium batteries) of activated carbon, physisorption properties play a vital role in desired performance achievement. Therefore, it is essential to investigate the influence of these pyrolysis methods on physisorption properties of activated biochar/carbon. The first goal of this thesis work is to meet this necessary investigation requirement.

Most of the research work that has been conducted in the utilization of biomass-derived carbon for energy storage application (such as supercapacitors and batteries) have prepared the carbon mostly through slow pyrolysis or microwave pyrolysis process. No significant

investigations were performed in the utilization of fast pyrolysis derived biomass carbon for energy storage applications. Among all the pyrolysis methods, the fast pyrolysis is the industrially viable process. Tons of biochar as a byproduct of bio-refineries are produced, which can be converted for high-value application into highly porous carbons for energy storage application. The second goal of this thesis work is to investigate the performance of fast pyrolysis derived biomass carbon for the lithium-sulfur battery application.

Additionally, for large-scale industrial application, sufficient supply of precursor materials is essential. However, this undeniable requirement is rarely considered in previous research works for utilization of biochar for energy storage applications. Another biomass source, Douglas-fir is chosen as woody biomass which is also widely available in North America. Douglas-fir has a soft wood structure with very low ash and nitrogen content. In this thesis work, canola meal and Douglas-fir were selected as the biomass sources to prepare activated biochar. Canola is the most available mustard crop in the world, which is an offspring of rapeseed (Brassica napus and Brassica campestris/rapa). After extracting canola oil from the canola seed by pressing, canola meal is obtained as a solid byproduct of canola oil. Due to its excellent amino acid profile along with high vitamin and mineral contents, canola meal is widely commercialized as high-protein livestock feed in cattle, swine, fish, and poultry farms[7]. Canola production has grown rapidly worldwide over the last 40 years, rising from the sixth largest oil crop to the second largest[8]. Canola meal is the second largest feed meal after soybean meal now. To meet the demand of food and fuel industries, production of canola is increasing rapidly both in Canada and United States. This growth of consumption of canola oil in upcoming years will not only produce byproducts such as canola meal but also result in immense pressure for their utilization[9]. Canola meal has several anti-nutritional factors such as glucosinolates, tannins, sinapine, and phytic acid, which are considered

as unfavorable toward its use for animal and human nutrition. [10,11] Glucosinolate is an organic compound that contains sulfur and nitrogen, which breaks down into toxic metabolites such as aglucones, isothiocyanates, thiocyanates, and nitriles in the digestive tract of animals that cause sickness, hypothyroidism, and liver damage[12]. Canola meal has substantial fiber content comparing with another sources of meals, which makes it less digestive than others.[11]. Additionally, canola meal has to compete with higher-protein sources, such as dry distiller's grains (DDGs) which is a byproduct of ethanol industry[9]. The issue of oversupply and the related price volatility, as well as the reduced profitability from the sale of the byproducts from bioenergy processing plants, drive the necessity of utilizing canola meal for renewable energy.[9] Other than as feedstock, canola meal is also used in the production of industrial enzymes, antibiotics, biopesticides, vitamins, and other bio-chemicals[13]. Successful investigation of these two biomass sources for high-value application with good performance will ease the large-scale commercial application.

1.2 RESEARCH OBJECTIVES

Fast pyrolysis is developing rapidly as a mean of producing advanced biofuels and other bio-based products since this thermochemical conversion process favors liquid production. Biochar is one of the byproducts of the process that represents 10-20 % of the total products. However, the current applications of biochar are low valued that includes combusting for heat and power, or applying as a soil amendment with an estimated wholesale value around $100 per ton[14]. However, biochar has very high potential for high valued application due to its carbon-rich and porous nature. Additionally, value-added applications for the biochar produced during fast pyrolysis process would increase the overall economic viability of fast pyrolysis technologies and

biomass utilization. The objective of the thesis work is to improve the value of biochar and utilize solid by-products of biorefineries for high-valued energy storage application. The overall goal of this project is to utilize by-products of bio-refineries to fabricate electrode materials for energy storage. The purpose of the whole work has been divided into two tasks, such as:

1.2.1 Investigation of the influence of biomass pyrolysis method on physical and chemical properties of chemically activated biochar/carbon.

This study was focused on identifying the effect of biochar preparation methods on physical and chemical properties of activated biochar/carbon. For this purpose, biochar samples were prepared through fast pyrolysis and slow pyrolysis methods at 500˚C from woody biomass Douglas-fir and food-industry by-product canola meal. Later, these biochar samples were activated using potassium hydroxide (KOH) as the chemical agent at 800˚C. The effect of biochar preparation using fast and slow pyrolysis methods was evaluated by comparing the physisorption properties (surface area, pore volume, average pore diameter, pore size distribution, micropore and mesopore volume and area), elemental analysis, and Raman and FTIR spectroscopy of activated biochar.

1.2.2 Investigation of the applicability of fast pyrolysis biochar derived from Canola meal and Douglas-fir biomass for Li-S battery.

This study was focused on the synthesis of sulfur-porous carbon composite utilizing the micro-mesoporous carbon samples prepared at the previous objective. Suitable carbon structure with high surface area, pore volume, and nitrogen content were chosen for fabrication of Li-S cell. Selected amount of sulfur was loaded for each cell following by melt-diffusion strategy at 155˚C.

The performance of the batteries was evaluated by galvanostatic charge-discharge measurements and cyclic voltammetry.

To summarize, this thesis studied the influence of biomass pyrolysis method on physical and chemical properties of chemically activated biochar/carbon. On Chapter 1, the rationale and objectives and structure of thesis are presented. A review of the literature on preparation, properties, and application of biochar is provided in the first part of Chapter 2. On the latter part of Chapter 2, a review of the literature on principle, advantages, challenges and recent research works performed in the development of cathode of the Li-S batteries is presented. Chapter 3 presents the methods of preparation of Li-S battery cathode from raw biomass sources, and characterization methods to analyze the properties and performance of the samples. Obtained results and related discussions are included in Chapter 4. Chapter 5 summarizes the overall study with the principal finding and involves the direction for future research work.

References

1. Ronsse, F., van Hecke, S., Dickinson, D. & Prins, W. Production and characterization of slow pyrolysis biochar: Influence of feedstock type and pyrolysis conditions. *GCB Bioenergy* **5,** 104–115 (2013).
2. Crombie, K., Mašek, O., Sohi, S. P., Brownsort, P. & Cross, A. The effect of pyrolysis conditions on biochar stability as determined by three methods. *GCB Bioenergy* **5,** 122–131 (2013).
3. Yoder, J., Galinato, S., Granatstein, D. & Garcia-Pérez, M. Economic tradeoff between biochar and bio-oil production via pyrolysis. *Biomass Bioenergy* **35,** 1851–1862 (2011).
4. Sohi, S. P., Krull, E., Lopez-Capel, E. & Bol, R. A review of biochar and its use and function in soil. *Advances in Agronomy* **105,** (Elsevier Inc., 2010).
5. Qian, K., Kumar, A., Zhang, H., Bellmer, D. & Huhnke, R. Recent advances in utilization of biochar. *Renew. Sustain. Energy Rev.* **42,** 1055–1064 (2015).
6. Suliman, W., Harsh, J. B., Abu-Lail, N. I., Fortuna, A. M., Dallmeyer, I., & Garcia-Perez, M. Influence of feedstock source and pyrolysis temperature on biochar bulk and surface properties. *Biomass Bioenergy* **84,** 37–48 (2016).
7. Canola Meal Feeding Guide, 5th Edition. *Canola Council of Canada* (2015).

8. USDA, Economic Research Service - Canola. Available at: https://www.ers.usda.gov/topics/crops/soybeans-oil-crops/canola/.
9. Azargohar, R., Nanda, S., Rao, B. V. S. K. & Dalai, A. K. Slow pyrolysis of deoiled canola meal: Product yields and characterization. *Energy and Fuels* **27,** 5268–5279 (2013).
10. Khattab, R. Y. & Arntfield, S. D. Functional properties of raw and processed canola meal. *LWT - Food Sci. Technol.* **42,** 1119–1124 (2009).
11. Mailer, R. J., McFadden, A., Ayton, J. & Redden, B. Anti-nutritional components, fibre, sinapine and glucosinolate content, in Australian Canola (Brassica napus L.) meal. *JAOCS, J. Am. Oil Chem. Soc.* **85,** 937–944 (2008).
12. Rambabu, N., Rao, B. V. S. K., Surisetty, V. R., Das, U. & Dalai, A. K. Production, characterization, and evaluation of activated carbons from de-oiled canola meal for environmental applications. *Ind. Crops Prod.* **65,** 572–581 (2015).
13. Ramachandran, S., Singh, S. K., Larroche, C., Soccol, C. R. & Pandey, A. Oil cakes and their biotechnological applications - A review. *Bioresour. Technol.* **98,** 2000–2009 (2007).
14. Galinato, S. P., Yoder, J. K. & Granatstein, D. The economic value of biochar in crop production and carbon sequestration. *Energy Policy* **39,** 6344–6350 (2011).

CHAPTER 2: LITERATURE REVIEW

2.1 INTRODUCTION

This chapter includes a literature review on two topics such as biochar and lithium-sulfur cell. At first, different thermochemical conversion processes for biochar production are discussed. Among these processes, different pyrolysis process and the effect of pyrolysis conditions on biochar properties are discussed in detail. Application of biochar with and without activation is also discussed along with activation processes of biochar. Two chemical activation methods namely KOH and $ZnCl_2$ activation are discussed. On the latter part, different types of batteries are discussed along with an introduction to the lithium-sulfur battery. Mechanism and commercialization challenges are discussed followed by various investigated strategies to meet those challenges. Also, cathode composite prepared using different types of porous carbon such as micro-, meso- and hierarchical porous carbons are discussed with the previous research performed on enhancing lithium sulfur cathode utilizing heteroatoms (N-doping). Finally, utilization of activated biochar as a porous carbon source and related research works are discussed.

According to the projection of the U.S. Energy Information Administration (EIA), electricity generation in the U.S. from renewable energy sources (such as the wind, solar, and wave) is increasing significantly, and it will be the second major source of electricity generation by 2030 (shown in Figure 2.1) [1]. Due to the continuous decrease in cost, wind and solar are now cost competitive with fossil fuels in favorable locations. However, this trend may reverse as the

energy that is not available on-demand but only at specific times, such as when the wind is blowing. Thus, energy storage plays an essential role in storage and distribution of energy from the intermittent energy sources such as the wind and solar. Furthermore, energy storage is going to play a major role in the upcoming future than any other time in the past due to sharp upward trend (shown in Figure 2.2)[1] in the electrification of vehicles and need for storing energy obtained from renewable sources.

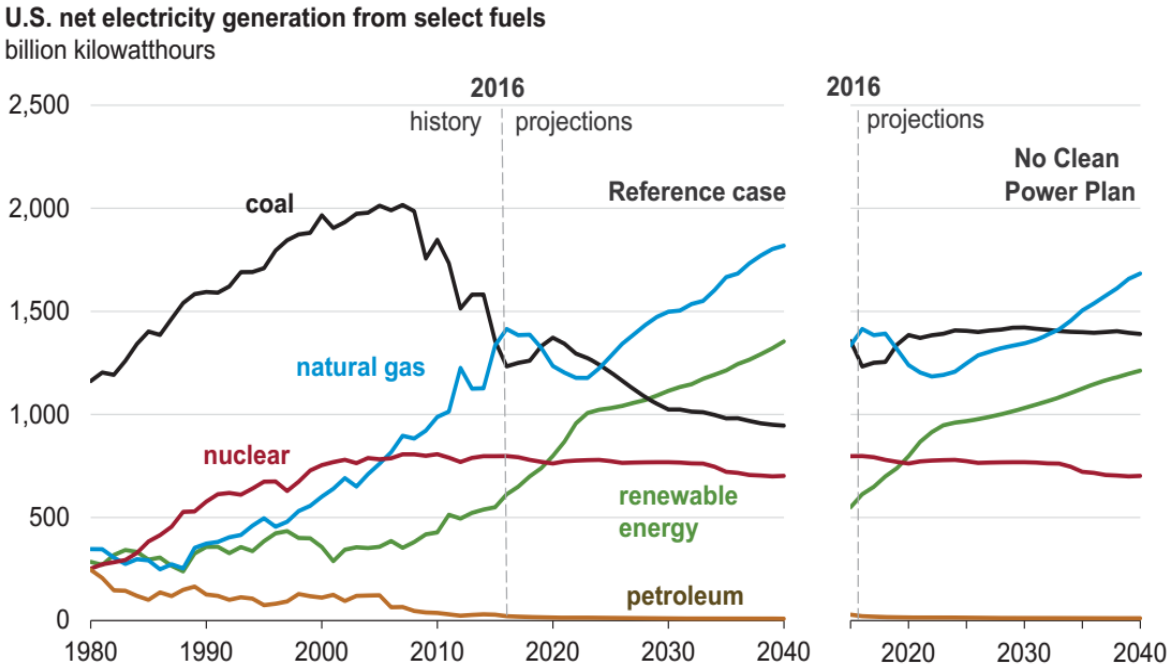

Figure 2.1: Statistics and projection of U.S. net electricity generation from different fuels.[1]

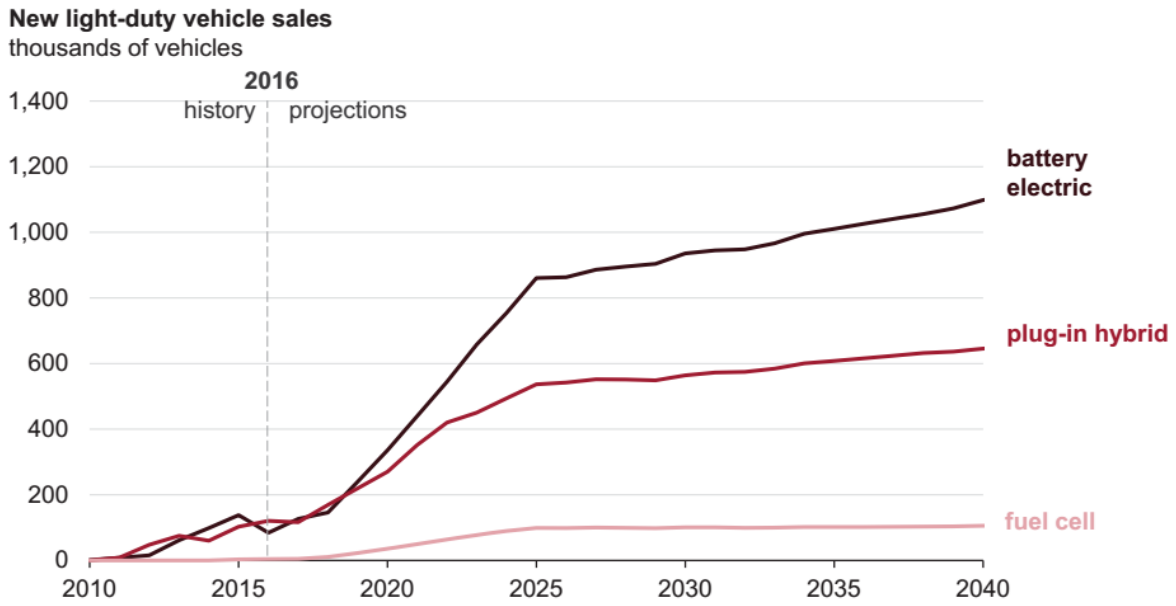

Figure 2.2: Statistics and projection of new light-duty vehicles sales in U.S.[1]

Among the various energy storage technologies, lithium batteries are expected to play a significant role because of their high specific energy (energy per unit weight) and energy density (energy per unit volume). Rechargeable lithium-ion batteries (LIBs) are already playing an important role in cutting-edge portable electronic devices and electric vehicles. Since their first introduction in 1991, LIBs have transformed portable electronic devices dramatically. However, even when fully developed, the highest energy storage that LIBs can deliver is not enough to meet the demand of an extended range of electric vehicles. So, it is essential to explore new chemistry, especially electrochemistry, and new materials for new generation of lithium batteries to reach beyond the limitations of LIBs. Among the few options to go beyond the energy storage limitations of LIBs, the lithium-sulfur (Li-S) battery has an excellent potential to meet the high-energy storage demand. The current LIBs provide theoretical specific energy of 387 Wh kg^{-1}, the theoretical energy density of 1015 Whl^{-1}, and a cell voltage of 3.8 V. On the other hand, the Li-S battery provides theoretical specific energy of 2587 Wh kg^{-1}, the theoretical energy density of 2199

Whl^{-1}, and a cell voltage [2] of 2.2 V. However, the commercialization of Li-S batteries is hindered due to several challenges such as poor cycling life, low sulfur utilization and volume expansion of sulfur during cycling [3]. These problems are caused by the insulating nature of S and its end discharge product Li_2S, and dissolution of reaction intermediates of polysulfide.

Among the various strategies investigated to overcome the commercialization challenges associated to Li-S batteries, the application of electrically conductive porous carbon to confine sulfur and lithium polysulfides has received wide attention. For instance, porous carbon-sulfur nanocomposite cathode can enhance the electrical conductivity of the composite cathode, restrict the dissolution of polysulfides, and accommodate volume expansion of the active materials during charge and discharge process[4]. However, the synthesis process for porous carbon materials typically requires elaborate procedures, involving high-temperature process and very corrosive acid for template synthesis[5–8]. For example, synthesis process of commercial mesoporous carbon[8] CMK-3 is complicated, and thereby, it is costly (US $220 per 1 g according to ACS Material, LLC), lacks scalability and consistency.[9] Therefore, it is essential to obtain porous carbon host by facile, environment-friendly and cost-effective synthesis process. Since many biomass materials have natural hierarchical structures with organic/inorganic composite, well-designed carbonization or activation process can transform these into microporous, mesoporous or hierarchical porous carbon materials with the very high surface area and high pore volume [10]. Additionally, many biomass carbons can be derived from originally waste materials, which are renewable, cheap and environment-friendly. These advantages make them a promising candidate for Li-S battery development and other numerous applications such as other types of batteries, supercapacitors, fuel cell, hydrogen storage, sensors, catalysis, separation, and adsorbent.

Biochar is a biomass-derived carbon-rich material, which is prepared through oxygen-limited thermochemical conversion of biomass. As an inexpensive, electrically conductive, readily available, environmentally friendly, and sustainable carbonaceous material, biochar has been widely studied for the application in supercapacitors, battery and hydrogen storage. Biochar can have high surface area and pore volume, which can be tailored through the activation process. Chemical activation such as KOH or $ZnCl_2$ can significantly enhance the surface area, pore volume and introduce various pore size distribution. Additionally, biochar derived from nitrogen-rich biomass can be used an excellent porous carbon with readily available nitrogen-doping to encapsulate sulfur to fabricate sulfur-carbon composite for Li-S sulfur batteries with excellent electrochemical performance.

2.2 THERMOCHEMICAL CONVERSION PROCESSES FOR BIOCHAR PRODUCTION

Biochar is a carbon-rich solid residue material obtained from the thermochemical reactions of biomass under oxygen-limited environment [11–16]. A wide range of biomass feedstocks is available to prepare biochar including wood, agricultural residue, poultry residue, forest residue, food industry waste, and animal waste[9,17–22]. Woody biomass is a major source for biochar preparation worldwide. Woody biomass consists of various amounts of hemicellulose, cellulose, lignin, and small quantities of other organic extractives (such as fats, phytosterols, and phenolics) and inorganic compounds (such as nitrogen, phosphorous, sulfur, silicon, alkali and alkaline earth metals, and various trace minerals)[16]. Depending upon the feedstock source conditions (such as botanical species, plant part, soil type, climate conditions, and the time of harvest), the biochar structure can significantly vary.[16,21,23] Biochar can be prepared in solid form through pyrolysis or gasification of biomass, and in slurry form through hydrothermal carbonization of biomass under

pressure[15,24]. Typical operating conditions and char yields of different thermochemical processes are shown in Table 2.1.

Pyrolysis is the most common method to produce biochar. In this process, biomass is thermochemically converted into bio-oil, biochar, and gas using either conventional heating systems or microwave heating systems at different temperature and vapor residence time in the oxygen-free inert environment. Pyrolysis is mainly performed to produce liquid bio-oil, but biochar is obtained as a byproduct. Gasification is carried out by supplying a controlled amount of oxidizing agent under high temperature (greater than 700˚C) to produce primarily a gaseous mixture (syngas containing CO, H_2, CO_2, CH_4, and smaller quantities of higher hydrocarbons). A small amount of biochar is also produced as a byproduct. The conventional oxidizing agent used in gasification can be oxygen, air, steam or mixtures of these gases. Unlike other processes, hydrothermal carbonization (HTC) of biomass takes place in water at elevated temperatures (160–800˚C) and elevated pressure (more than 1 atm). Elevated pressure is required to maintain the water in a liquid form above 100˚C[15,25]. It is noteworthy mentioning that the properties of biochar produced from different processes will be different.

Table 2.1: Conditions and char yields obtained by different thermochemical conversion methods of biomass

Thermochemical Conversion Process	**Conditions**			**Char Yield (%)**	**Ref.**
	Temperature (˚C)	Vapor residence time	Reaction medium		
Fast pyrolysis	400-600	0.5-10s	Inert	10-20	26–28
Slow pyrolysis	300-800	min to days	Inert	20-40	23,27,29

Microwave pyrolysis	400-800	1-22min	Inert	20-60	30,31
Gasification	800-1000	5-20s	Air/O_2 /Steam/CO_2	~10	28, 32–34
Hydrothermal carbonization	160-800	1-12h	Water	30-60	15,25

2.3 INTRODUCTION OF PYROLYSIS BIOCHAR

Among the various biomass conversion technologies, pyrolysis is a relatively straightforward technique, and the most common method to produce biochar because of its yield and properties. This process dates back to at least ancient Egyptian times when tar for caulking boats and certain embalming agents were produced through pyrolysis [35]. Since then pyrolysis processes have been widely applied to produce coke and charcoal. Pyrolysis is the most common method of biochar production[15]. The necessary heat energy for endothermic pyrolysis reactions is usually supplied by direct heating or indirect heating from hot gases, hot solids, liquid heat transfer medium, oxidation and partial oxidation reactions[30].

During the pyrolysis process, hemicellulose is the first component to decompose at a temperature of 220-315˚C[36]. Cellulose decomposes at temperatures of 315-400˚C. Among the three component, lignin requires a higher temperature to break down completely. The lignin decomposition happens slowly from ambient to 900˚C temperature range[36,37]. For maximizing the yield of liquid products from biomass pyrolysis, a moderate temperature(450-500˚C), high heating rate, and short gas residence time process would be required[37]. A low temperature (300-450˚C) and low heating rate process would be necessary for high yield of solid products (i.e. char)[37].

Pyrolysis can be classified into slow pyrolysis and fast pyrolysis based on the heating rate and residence time.

2.3.1 Slow Pyrolysis Biochar

Slow pyrolysis, also called conventional carbonization, is the conventional method for charcoal production and has been used to produce charcoal for centuries. Slow pyrolysis has relatively low heating rate and long residence time. Biomass is heated slowly in the oxygen-limited environment at 300-500°C and vapor residence time varies in between few minutes to several days. Unlike fast pyrolysis, vapors and aerosol components remain in contact with solids and participate in the secondary reactions to produce more carbonaceous solids (biochar), and favor the production of biochar [38].

2.3.2 Fast Pyrolysis Char

Fast pyrolysis has been actively explored to produce renewable liquid fuels that can be used as an alternative fuel oil or chemical feedstock[39]. In this process, dried biomass (less than 10% by weight moisture content) is heated at a higher heating rate (above 200˚C min^{-1}) and shorter residence time (less than 10 s) for gas-phase products, which can lead to higher bio-oil yield. [40,41]. This process is typically performed at 400-600°C and results in vapor residence time at 0.5-10 sec. Here, vapors and aerosol components are rapidly removed from the solids and favors more bio-oil production as compared to biochar [38]. In fast pyrolysis, biomass yields 60%-70% by weight liquid bio-oil, 15%-25% by weight biochar and 10%-20% by weight non-condensable gases [40].

In a fluidized-bed fast-pyrolysis reactor with char separation system, two types of biochar can be collected such as (i) the char remained inside of reactor mixed with bed materials and (ii)

the char separated from the gaseous part outside the reactor. The latter one is the char collected from high-temperature char separation system or filter (HTF biochar). The unreacted alkali and alkali earth metals (AAEMs) in the raw materials during pyrolysis process remain in the products, which concentrates them in the char leading to an increase in ash content. The high-temperature biochar filters or separators are typically heated up to 400˚C to prevent the condensation of vapor products. Several secondary reactions take places in the hot filter, which lead mainly to the evaporation of hydrocarbons from char particles not separated from the cyclone or to the formation of a secondary char from the product vapor [41]. As a result, most of the AAEMs present in the feedstock remains in the HTF biochar due to the char separation system, which results in high-quality bio-oils due to low concentrations of alkali and alkaline earth metals.[41,42]

2.3.3 Effect of Pyrolysis Conditions on Biochar Properties

The characteristics of biochar vary with feedstock and pyrolysis conditions. Raw biochar yield decreases with pyrolysis conditions such as residence time and treatment temperature as well as the ash content of the feedstock biomass.[11] The ash and fixed carbon contents of the biochar also increase with pyrolysis temperature, whereas the mass fraction of volatile matter, oxygen, the ratios of oxygen to carbon (O/C) and hydrogen to carbon (H/C) linearly reduce [11,16,23]. Additionally, total alkaline content increases with pyrolysis temperature leading to higher pH and electrical conductivity. [16] The feedstock properties along with the pyrolysis temperature are the main factors influencing biochar bulk and surface properties. [43] The surface area of the biochar gradually increases with pyrolysis temperature due to micropore formation on the biochar surface[16]. Biomass with high lignin and mineral contents results in higher yield of biochar[44]. The carbon content of biochar can be varied by altering the feedstock or pyrolysis conditions. Woody

and herbaceous biomass usually provide a more carbon-rich biochar compared to other biomasses such as sewage sludge and animal manures at high pyrolysis temperatures[16,45]. In various research studies, it has been reported that biochar yield, aliphatic carbons, oxygenated functional groups, and contents of nitrogen, oxygen, and hydrogen in biochar decreased with increasing reaction temperature. [43,45–48]

2.4 APPLICATIONS OF BIOCHAR

Biochar can be combusted for heat and power[28], but biochar has received a wide attention due to its potential in other high value and environment-friendly applications[28]. The most attractive feature of biochar is that it represents an inexpensive, sustainable and facile production process that allows the production of materials with extensive applications at a lower cost compared to the materials produced from the non-renewable sources and by a complicated process. Although most of the applications are still in their infancy, biochar can already be used in many applications with extraordinary effects[15].

The most common application of biochar is a soil amendment due to its potential to enhance soil fertility and carbon sequestration. This application as the soil amendment dates back to the Amazonian Dark Earths (known as Terra Preta) in the Amazon basin where charred organic materials appear to have been applied intentionally to the soil to enhance its fertility[14,49]. However, the brittleness, broad range of particle sizes and low density of biochar make its very challenging to handle, transport to the field, and apply them in the soil. Approximately 25% of biochar is lost during spreading to the soil, and 20%-53% is washed by rain water [50]. Making nutrient-rich biochar pellets shows a durable and economical way of slow-release fertilizer (SRF). Slow-release fertilizer (SRF) releases the nutrients gradually according to nutrient requirements of a plant

without leaching losses [51], which can save a good portion of the nutrient cost, and the environment from the potential damage from added nutrients [52]. Several investigations have been performed to engineer biochar as SRF or to make SRF composite with biochar [53–55]. Oh et al.[53] reported that the biochar impregnated by anaerobically digested slurry nutrients has the potential to be an effective slow-release K^+ fertilizer. They also found that impregnated biochar has similar water-soluble K^+, Ca^{2+} and Mg^{2+} release behavior as commercial SRF. Biochar-SRF also showed good water retention capacity of the soil. Kim et al.[55] blended lignin, switchgrass biochar and K and P fertilizer together and processed pellets at different temperature using 10%-30% by weight lignin as a binding agent. They showed that nutrient release rate of biochar pellets could be controlled by controlling lignin content and pellet processing temperature. Therefore, nutrient-rich biochar pellets can be an effective economic and durable SRF.

Another promising application of biochar is as a sorbent for several environmental contaminants, including heavy metals. Biochar has excellent adsorption capabilities which can reduce the number of harmful pollutants from soil and water. In comparison with the commercial activated carbon, biochar has a much lower surface area, but this drawback is counterbalanced by the presence of a high number of oxygenated groups such as carboxyl, hydroxyl, and phenolic surface functional groups on the surface or biochar. Studies have shown that these oxygenated groups are binding sites for soil contaminants [56]. Some investigations have been done to study biochar for the reduction of heavy toxic metals from water. Mohan et al..[57] investigated the biochar derived from the pine wood, pine bark, oak wood and oak bark prepared by pyrolysis process at 400 to 450˚C. The high surface area (25.4 $m^2 g^{-1}$) and total pore volume (0.86 $cm^3 g^{-1}$) along with higher calcium content of Oak bark derived biochar resulted in higher adsorption of Pb(II), Cd(II) and As(III) than the other biochars.

Biochars also has been investigated for adsorption of odorous and environmentally hazardous gas such as hydrogen sulfide (H_2S) that can be released in gasification, oil or gas production process, wastewater treatment plants and landfills[58]. Due to higher surface area and pore volume, activated carbon is an effective sorbent to dissociate H_2S. Extensive studies have been done related to this [59,60]. Shang et al. have investigated H_2S breakthrough time, saturation time, and breakthrough capacity of activated carbon (AC), camphor (SC), bamboo (SB), and rice hull (SR) biochar at 400^oC by oxygen-limited pyrolysis. The breakthrough capacities and removal rate of SR were superior to those of SB, SC, and AC because SR possessed a higher pH (10.56) value. The biochar samples were basic with higher quantities of oxygen-containing functional groups than commercial AC.

Recently, biochar has also been investigated for energy storage applications such as supercapacitor, lithium batteries, and hydrogen storage. Producing high quality and inexpensive electrode materials with high surface area, high pore volume, and desired pore size distribution are critical for the development of the energy storage industry. Carbon that has high surface area and porous structure is the primary raw material for making supercapacitors due to its broad availability and low environmental impacts[62]. Recently, several researchers used biochar derived from different biomass sources (such as woods, sludge, soybean meal, pig bone, rice husk, rice straw and bamboo) as raw materials for the electrode of supercapacitor, lithium-sulfur cells, lithium-ion batteries and hydrogen storage. Biochars are chemically activated by mixing with an activating reagent such as H_3PO_4, $ZnCl_2$, KOH or HNO_3 to enhance surface area, pore volume, and the number of surface oxygen groups. For supercapacitor application, the microstructure of electrode materials and the presence of surface oxygen groups in electrode materials can influence the performance of supercapacitor greatly [15]. Wood derived biochar has a potential window of 1.3

V and a fast charge-discharging behavior with 14 F g^{-1} gravimetric capacitance[63]. HNO_3 activation can increase the capacitance of biochar by 7 times by increasing the number of surface oxygen groups[63]. Supercapacitor electrode made from biochar in the shape of mini-chunk and thin film shows the capacitive performance of 32 F g^{-1} and no degradation after 2600 cycles. Mini-chunk biochar electrode without any binding agents offers a fast and straightforward technique for making low-cost electrode for supercapacitor [64]. However, there is still more space to improve capacitance with low-cost and high-performance biochar supercapacitors. Woody biochar with high surface area, good conductivity, excellent electrochemical stability and unique porous structure can be promising materials for broad applications in energy and environment field [63]. Biochars has been investigated as inexpensive, porous and conductive carbon materials to encapsulate insulating sulfur to fabricate cathode of lithium-sulfur cells[9,65]. Application of biochar in lithium-sulfur batteries has been further discussed in section 2.9.3 and 2.94.

2.5 ACTIVATED CARBON OR ACTIVATED BIOCHAR

Another promising application of biochar is as the raw materials for activated carbon[66]. Activated carbon is a generic term for a family of porosity (space) enclosed carbon material, none of which can be characterized by a structural formula or by chemical analysis.[67–69] Activated carbon exhibits high surface area and high porosity. The pore volume of activated carbon is greater than 0.2 cm^3 g^{-1}, and the internal surface area is larger than 400 m^2 g^{-1} as measured by N_2 Brunauer–Emmett–Teller (BET) method. The width of pores varies from 0.3 nm to several thousand nanometers[68]. Activated carbons prepared from biomass sources are also known as activated biochar. Azargohar and Dalai[60] evaluated biochar produced through fast pyrolysis and activated the biochar using KOH. Activated carbon generated by this method has an internal surface area at

least 50 times of starting material. BET surface area of activated carbon produced by this material can be as large as 1500 $m^2 g^{-1}$.

Activated biochar provides good adsorptive capacities due to its high surface area and pore volume. Activated carbon has a broad range of application in agriculture, water purification, energy storage, and gas adsorbents due to its adsorption capability. Most of the commercial applications (such as water purification and gas adsorption) of activated carbons are due to its adsorption abilities. However, activated carbon has been investigated for additional applications, such as catalysts, membranes, carbon fibers, nanoparticles, and electrodes for energy storage. Research has been focused on understanding surface characteristics and adsorption mechanisms, selectivity and capacity for removal of various contaminants, and the use of activated carbon for novel chemical applications. Also, the production of activated carbon from other feedstocks such as olive stones, waste plastics, municipal waste sludge, coke and rice husk have been an important topic in recent years. The benefits of leveraging the economics of the pyrolysis platform through the production of inexpensive activated carbon could significantly impact the industrial and agricultural sectors of the economy.

2.5.1 The Porosity of Activated Carbon

Based on pore width, pores are classified as micropores, mesopores, and macropores. Micropores are the pores with pore width less than 2 nm. Pores with a width in between 2 and 50 nm are called mesopores. Macropores are pore with 50 to 2000 nm pore width. Macropores mainly depend on the nature of the carbonaceous feedstock materials employed, and the preliminary manufacturing process (i.e. grinding and agglomeration of the raw materials). Macropores typically contribute very little to the internal surface area, whereas mesopores and micropores account for about 5 and 95% respectively.[68] Activated carbons are filled with pores of the size of

molecules, and those pores are of zero electron density. The pores possess intensive van der Waals forces (from the proximity of carbon atoms), and these are responsible for the adsorption process[69].

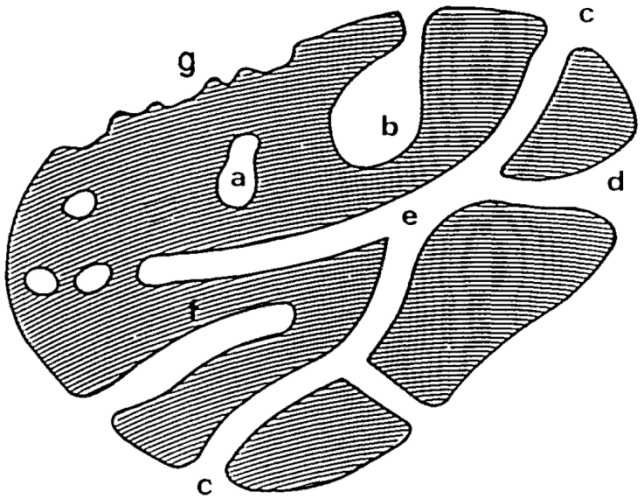

Figure 2.3: Schematic cross-sectional representation of a porous solid (Rouquerol et al.[70])

Pores can be categorized depending on their accessibility to an external fluid. Closed pores (a) are inaccessible to an external fluid and isolated from their neighbors (Figure 2.3). This type of pores influence macroscopic properties (such as bulk density, elasticity, mechanical strength, and thermal conductivity), but they are inactive in adsorption of gases or fluid flow processes[70,71]. On the other hand, open pores have a navigable channel of communication with the external surface of the body (like b, c, d, e, and f)[71]. Open pores are further classified into "through pores" and "blind pores." Through pores have an open channel that starts at one location on the surface, extends into the particle, and re-emerges on the surface at another location (like the pore channels c-e-c and c-e-d)[71]. Blind pores (also known as dead-end or saccate pores) are open to the surface only at one end (like b and f). However, if the width of surface irregularities is smaller than the depth, those are called surface roughness rather than pore (like g).[70,71] Based on their shape, pores

can be further categorized as cylindrical (open c or blind f), ink-bottle (b), funnel (d), and slit shapes. [70,71]

2.6 ACTIVATION METHOD OF BIOCHAR

Activated carbon can be prepared from any carbonaceous raw materials[68]. Numerous carbon sources have been explored for processing of activated carbon from various sources such as coal (peat, lignite, bituminous and anthracite), coconut shells, apricot stones, waste tires, wood, animal waste, heavy petroleum oil, cellulose, risk straw and husks, corn cobs and bamboo [9,63,66,68,72–80]. Biomass has been widely investigated as a precursor for activated carbon, which typically requires two steps to prepare activated carbon or biochar from biomass. Firstly, raw biomass is subjected to a thermal conversion under the oxygen-limited environment to produce biochar [77]. Secondly, biochar is subjected to chemical or physical activation method [67–69,81]. The final physicochemical characteristics and potential uses of activated carbon are greatly influenced by the biomass feedstock, feedstock pretreatments, carbonization method, and activating conditions(temperature, pressure, gas type and flow rates, heating rates, holding times, and quenching conditions) [82].

2.6.1 Physical Activation

Physical activation is a performed in two steps. The first step is to carbonize the carbonaceous material to produce char. The purpose of the carbonization is to reduce the volatile content of the precursor material to convert the resulting char with higher content of fixed carbon for activation purpose[68]. Carbonization process involves the pyrolytic decomposition of the starting material and non-carbon species elimination. The volatiles with low molecular weight are

released at first followed by light aromatics and hydrogen gas. The tarry pyrolysis residues fill the pores which formed during the carbonization step[83]. The second step is to physically activate the resulting char at high temperatures (600-1200°C) in the presence of oxidizing gasifying agents such as oxygen, carbon dioxide, steam, air or their mixtures[75]. The pores and vessels are formed due to the entrance of the oxidizing gases into the char and removal of the reaction products through particles[83]. The gasification process at first removes the more reactive carbon atoms hence forming porosity. Further gasification increases the porosity of the activated carbon[83].

Physical activation process does not require any corrosive chemicals to activate the biochar. Thus, it is clean, environment-friendly and easy to control the activation process [15,32,75]. Biomass sources such as rice husk, rice straw, rice hull, jute stick, coconut shell, sugarcane bagasse, walnut shell, olive stone, hazelnut shell, oak, pecan shell, palm shell, almond husk, pistachio-nut shell and corn cob were the raw biomass materials studied to prepare activated carbon by this method [75,83,84].

2.6.2 Chemical Activation

Chemical activation method also involves two steps (such as carbonization and activation) that can be carried out simultaneously or sequentially. Chemical activation is performed by mixing carbonaceous materials (e.g. biochar) with chemical activating agents (e.g. KOH, H_3PO_4, $ZnCl_2$), followed by the carbonization at 400–900°C. The product is later washed to remove activating agents. Compared with simultaneously performed or one step chemical activation and physical activation, sequentially performed two-step chemical activation has the advantage of producing highly microporous activated carbon with high surface area[15].

In comparison with the physical activation process, chemical activation has excellent benefits such as lower activation temperatures, higher yields, less activation time, and greater surface area and pore volume[69,77]. The porous carbon obtained with chemical activation process can have a surface area over 2000 $m^2 g^{-1}$ and large pore volume mainly made up of micropores and some small mesopores[69,77]. Additionally, parts of chemicals used in chemical activation can be recovered easily[75]. For energy storage applications, chemical activation is preferred over physical activation due to the scope of obtaining comparatively higher surface area and micro/mesopore volumes.

(i) KOH Activation

Among various chemical activation reagents, KOH is widely used because of its ability to result in porous carbons with defined micropore size distribution, high micropore volume, and a huge surface area of up to 3000 $m^2 g^{-1}$. [85] KOH activation has been known since Wennerberg et al.[85] prepared famous commercially available AX21 and Maxsorb activated carbons using fossil-based carbon sources.

In KOH activating technique, the surface area and porosity development are due to the synergistic and comprehensive actions including chemical activation, physical activation, and carbon lattice expansion by the metallic K intercalation[77]. However, the real reaction processes and activation mechanisms are variables depending on the activation parameters (such as the mass of KOH, activation temperature and time) as well as on the reactivity of various carbon sources. Both the activation parameters and carbon sources play very significant role in the pore microstructure and surface chemistry, which further affects the performance of KOH-activated carbons in many applications from adsorption to the energy storage. [77]

Numerous investigations have been performed altering activation parameters and using different carbon sources (e.g. coals, pitches, natural biomass, synthetic organic polymers) to prepare the

activated carbons. Additionally, KOH activation technique also applied to efficiently generate micropores and small mesopores into the framework of various carbon structures, such as carbon fibers (CFs), carbon nanofibers (CNFs), CNTs, templated porous carbons (TPCs), carbide-derived carbons (CDCs), carbon aerogels (CAs), and graphene. These KOH-activated carbons with increased surface area and porosity have been applied in H_2 storage, supercapacitors and batteries to obtain the optimal porous carbons for high-power energy storage applications.[66,75,77]

In the KOH activation process, the reaction between carbons and KOH starts with solid–solid reactions and then proceeds through solid–liquid reactions including the reduction of potassium (K) compound to form metallic K, the oxidation of carbon to CO_2 and carbonate, and other reactions among various active intermediates[77]. Otowa et al.[86] proposed KOH activation mechanism that included several simultaneous/consecutive reactions. Some of these reactions are mentioned in Eq 1-4.

$$2\ KOH \rightarrow K_2O + H_2O \quad \text{(dehydration at 400°C)} \qquad \text{(Eq.1)}$$

$$C + H_2O \rightarrow CO + H_2 \quad \text{(water-gas reaction)} \qquad \text{(Eq. 2)}$$

$$CO + H_2O \rightarrow CO_2 + H_2 \qquad \text{(Eq. 3)}$$

$$CO_2 + K_2O \rightarrow K_2CO_3 \qquad \text{(Eq. 4)}$$

Lillo-Ródenas et al.[87] proposed a prominent universal reaction combining the experimental data and theoretical calculations, which is stoichiometrically occurring between carbon and KOH during the KOH activation process. The reaction is shown in Eq. 5.

$$6\ KOH + 2\ C \rightarrow 2\ K + 3H_2 + 2\ K_2CO_3 \qquad \text{(Eq. 5)}$$

However, the reaction further proceeds via the reaction of metallic K with KOH to K_2O. During KOH activation, KOH reacts with C to form K_2CO_3 at about 400°C. KOH is completely consumed at about 600°C temperature. The as-formed K_2CO_3 (in Eq. 4 and 5), significantly decomposes into CO_2 and K_2O at temperatures higher than 700°C (Eq. 6) and completely disappears at about 800°C. Furthermore, the resulting CO_2 can be further reduced by C to form CO at high temperature (Eq. 7). When the temperature is higher than 700°C, the K compounds (K_2O and K_2CO_3) also can be reduced by carbon to produce metallic K[77] (Eq. 8 and 9).

$$K_2CO_3 \rightarrow K_2O + CO_2 \quad \text{(Eq. 6)}$$

$$CO_2 + C \rightarrow 2\ CO \quad \text{(Eq. 7)}$$

$$K_2CO_3 + 2\ C \rightarrow 2\ K + 3\ CO \quad \text{(Eq. 8)}$$

$$C + K_2O \rightarrow 2\ K + CO \quad \text{(Eq. 9)}$$

Three major KOH activation mechanism for carbon are concluded based on above observation and discussions. [77]

(a) Etching the carbon framework by the redox reactions between various potassium compounds as chemical activating reagents with carbon as shown in Eq. 5, 8 and 9, is called chemical activation[77]. This is responsible for generating the pore network.

(b) The formation of H_2O (Eq. 1) and CO_2 (Eq. 3 and 6) in the activation system positively contributes to the further development of the porosity through the gasification of carbon, is named as physical activation (Eq. 2 and 7).

(c) The as-prepared metallic K (Eq. 5, 8 and 9), efficiently intercalating into the carbon lattices of the carbon matrix during the activation process, causes the expansion of the carbon

lattices in Figure 2.4. The expanded carbon lattices cannot return to their previous non-porous structure after the washing out of the intercalated metallic K and other K compounds by acids and water. This results in the high microporosity that is essential for the high surface area and pore volume.

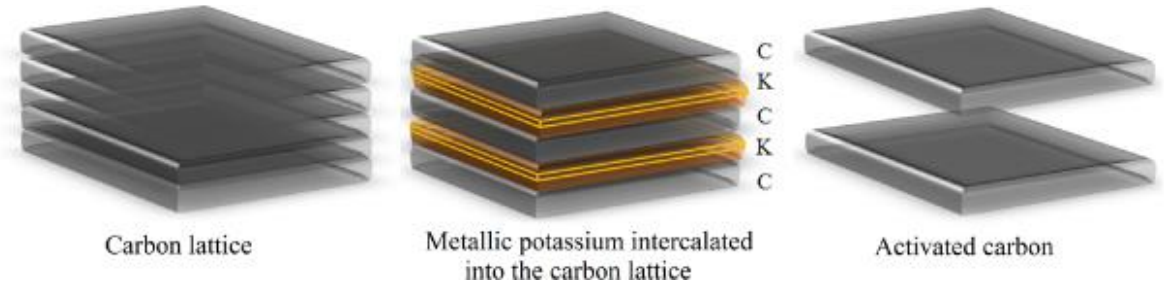

Figure 2.4: KOH activation mechanism by the penetration of metallic K into the carbon (C) lattices, the expansion of the lattices by the intercalated metallic K, and the removal of the intercalated K from the carbon matrix. [88]

The alkali metal (such as KOH) compounds work effectively as activating reagents above 600˚C[89]. The surface area increases in between the temperature of 500 and 800˚C and then decrease with further increase in temperature from 800 to 900˚C. The pore volume of the activated carbons prepared using alkali metal compounds generally increases with carbonization temperature of up to about 800˚C. This indicated that the pore enlarges up to this temperature. Above 800˚C, the excess enlargement induces the combination of pores, resulting in an increase in mesopores for all alkali metal salts and a decrease of micropore volume and surface area[89].

In laboratory scale, KOH activation is generally performed in a horizontal stainless tube furnace under an inert gas flow. The carbon source i.e. biomass materials is pre-treated with processes such as hydrothermal carbonization and pre-calcination to form chars before activation.

Then the chars are mixed with KOH either physically (by grinding or ball milling) or by impregnation with KOH aqueous solution. Typically, the preferable KOH and carbon mass ratio ranges from 2.5 to 3.5[77]. When the impregnation with KOH solution is adopted, an extra step for evaporation of water at low temperature is required. Later, the resulting mixture is put into a crucible or a tube and carbonized at high temperatures, e.g. 650–950°C under an inert environment. In some research work, the activation process consisted of a two-stage heat treatment. The first step is the dehydration at 370–400°C for 0.5 to 1.5 h which is performed to reduce carbon loss. The final stage is the activation at 750–900°C for 0.5 to 2 h. After cooling, the activation product is thoroughly washed with an aqueous acid solution and distilled water to remove any soluble impurities including remaining KOH, salts, and K formed during the activation, and then dried to obtain the activated carbon.[77]

(ii) $ZnCl_2$ Activation

The mechanism of $ZnCl_2$ activation is different as compared to the KOH activation. $ZnCl_2$ can act as a strong dehydrating agent, catalyzing the scission of glycosidic bonds and the elimination of hydroxyl and carbonyl groups presented in the biopolymer in biomass during the heat treatment. Thus, a large number of short biopolymer chains that have weaker interaction with other chains can be generated, and a carbonaceous thermoplastic phase can be formed due to the slippage of the polymer chains[90].

$ZnCl_2$ can be fused at its melting point (290˚C), then evenly mixed with the above thermoplastic phase. Furthermore, the fused $ZnCl_2$ can react with H_2O generated from the cleavage of the biopolymer, leading to the formation (Eq. 10) of zinc oxide chloride hydrate ($Zn_2OCl_2.2H_2O$). Most importantly, $ZnCl_2$ gas can be generated from the decomposition of

$Zn_2OCl_2.2H_2O$ with the increasing temperature[91](Eq. 11), and the gas diffusion developed pathways through the thermoplastic phase, creating the pore structure of the final product. The reactions are as follows, and the activation processes of KOH and $ZnCl_2$ were also illustrated by a schematic diagram in Figure 2.5.

$$\text{Lignocellulose}\left(C_xH_yO_z\right) + 2\,ZnCl_2 \xrightarrow{\Delta} C_xH_{y-6}O_{z-3} + Zn_2OCl_2.2H_2O + 2HCl + \text{Tar} \quad \text{(Eq. 10)}$$

$$Zn_2OCl_2.2H_2O \xrightarrow{\Delta} ZnCl_2 + ZnO + 2H_2O \quad \text{(Eq. 11)}$$

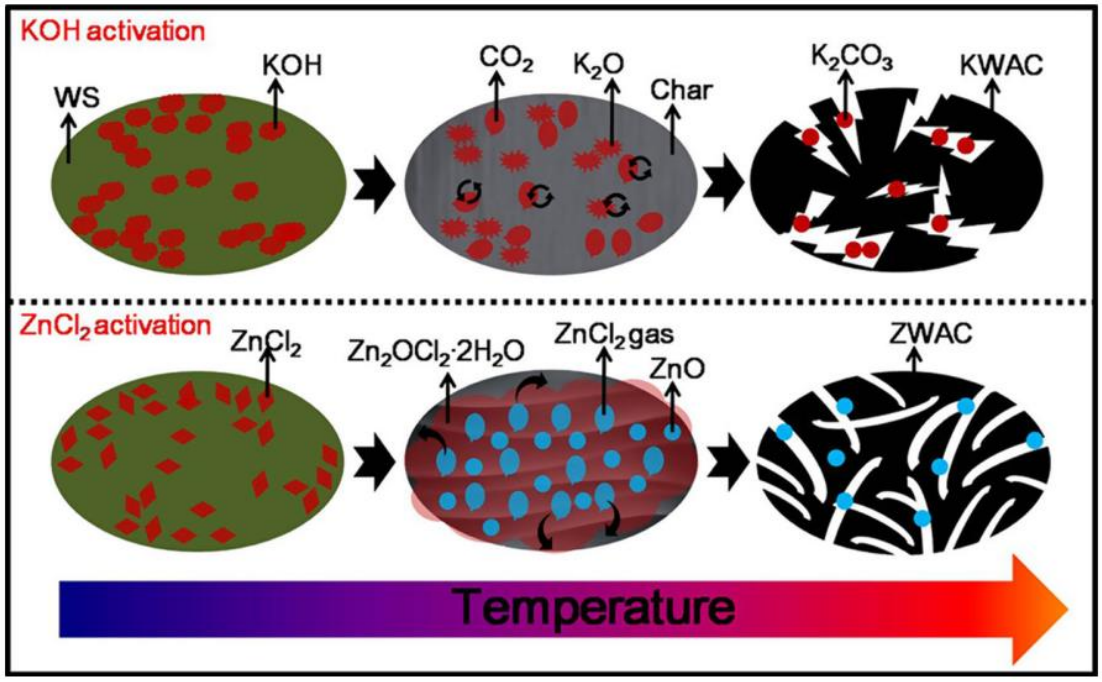

Figure 2.5: Schematic diagram of the KOH and $ZnCl_2$ activation processes[91] (Legends: WS= wheat straw biomass, KWAC= KOH-activated carbon, ZWAC= $ZnCl_2$ activated carbon)

Activation parameters such as impregnation weight ratio ($ZnCl_2$ to activated carbon precursor) and activation temperature have a significant influence on the porosity of resultant activated carbon. With the increase in impregnation ratio, the mesopore volume of activated carbon

increases significantly, and the micropore volume decreases slightly[92]. The enlargement of the existing micropores into mesopores predominates over the development of further micropores as a result of additional $ZnCl_2$[92,93]

$ZnCl_2$ works as a dehydrating agent and restricts the formation of tar and promotes the charring of the carbon below the carbonization temperature of 600˚C. It effectively works as activating agent below 500˚C and the maximum surface area, and pore volume can be obtained at 600˚C typically[89,93]. Above 600˚C, $ZnCl_2$ does not function as an activation agents. Accordingly, surface area and pore (micropore + mesopore) volume decrease due to heat shrinkage in carbon structure[89,93].

2.7 INTRODUCTION TO BATTERY

A battery or cell is an electrochemical device that converts chemical energy contained in its active materials into electric energy directly using an electrochemical oxidation-reduction (redox) reaction[94]. The term ‘‘battery’’ is often used to refer to the basic electrochemical unit ‘‘cell”. A cell consists of an assembly of electrodes, electrolyte, separators, container, and terminals. A battery consists of one or more electrochemical cells, electrically connected in an appropriate parallel/series arrangement to provide the required operating voltage and current levels, including, if any, monitors, controls and other ancillary components (e.g. fuses, diodes), case, terminals, and markings[94]. A cell has three main elements:

i. The negative electrode or anode—the reducing or fuel electrode—which gives up electrons to the external circuit and is oxidized during the electrochemical reaction.
ii. The positive electrode or cathode—the oxidizing electrode—which accepts electrons from the external circuit and is reduced during the electrochemical reaction.

iii. The electrolyte or the ionic conductor provides the medium for transfer of charge, as ions, inside the cell between the anode and cathode. The electrolyte is generally a liquid, such as water or other solvents, with dissolved alkalis, salts or acids to impart ionic conductivity. Some cells use solid electrolytes, which are ionic conductors at the operating temperature of the cell.

2.7.1 Operation of a Cell

The operation of a cell during discharge and charge is shown schematically in Figure 2.6. Discharge process starts when the cell is connected to an external load. During the discharge process (Figure 2.6a), electrons flow from the negative electrode, which is oxidized, through the external load to the positive electrode, where the electrons are accepted, and the positive electrode material is reduced[94]. The electric circuit is completed in the electrolyte by the flow of negative ions (anions) and positive ions (cations) to the negative and positive electrode, respectively. On the other hand, the current flow is reversed, and oxidation takes place at the positive electrode and reduction at the negative electrode during the recharge of a rechargeable cell (Figure 2.6b). By definition, the anode is the electrode at which oxidation occurs, and the cathode is the one where reduction takes place. Thus, the positive electrode is the anode, and the negative is the cathode during charging process[94].

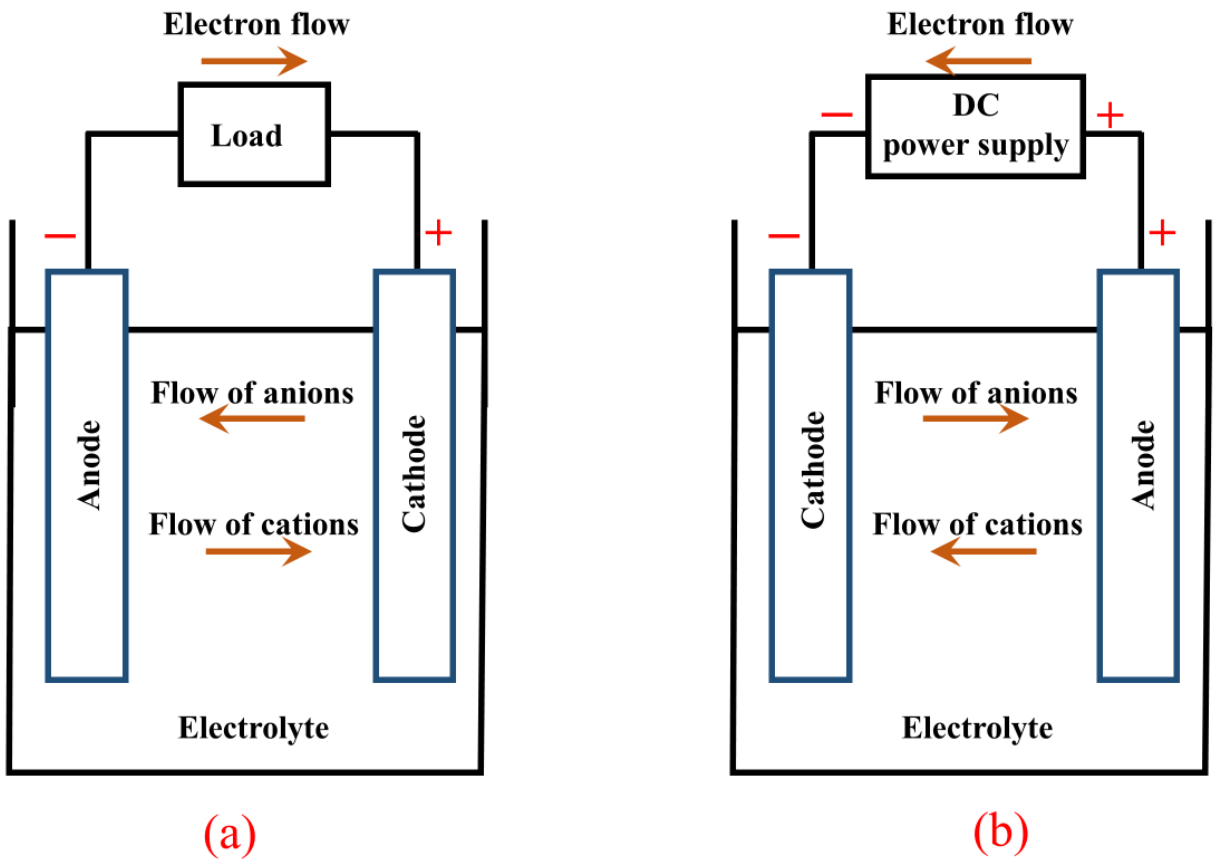

Figure 2.6: Electrochemical operation of a cell: (a) discharge process and (b) charge process (Redrawn from Linden et al.[94]).

2.7.2 Different Types of Battery

Based on the capability of being electrically recharged, electrochemical cells and batteries are categorized as primary (non-rechargeable) or secondary (rechargeable). Primary cells are not capable of being easily or efficiently recharged electrically and, hence, are discharged once and discarded. Few examples of primary batteries are zinc-air, silver-oxide, and alkaline MnO_2 batteries. On the other hand, secondary or rechargeable cells or batteries can be recharged electrically to their original condition by passing current through them in the opposite direction to that of the discharge current. Few examples of rechargeable batteries are Li-ion, Li-S, Na-ion,

lead-acid, Ni-Cd and nickel-metal hydride batteries. In Figure 2.2, examples of few popular cells along with their cell voltage, theoretical capacity, theoretical specific energy, theoretical energy density and overall reaction are presented.

Table 2.2: Different types of cells[94,95]

Cell	Cell Voltage (V)	Theoretical Capacity (mAh g^{-1})	Theoretical Specific Energy (Wh kg^{-1})	Theoretical Energy Density (Wh L^{-1})	Overall Reaction	Ref.
Conventional Li-ion	3.80	155	387	1015	$Li(C) + CoO_2 \leftrightarrow LiCoO_2$	2, 95
Li-S	2.20	1672	2567	2199[b]	$2\ Li + S \leftrightarrow Li_2S$	2
Li-air (non-aqueous)	3.00	3862	11248[a]	3436[c]	$2\ Li + O_2 \leftrightarrow Li_2O_2$	2, 96
Li-air (aqueous)	3.20	1861	5789[a]	2234[d]	$2\ Li + ½\ O_2 + H_2O \leftrightarrow 2\ LiOH$	2, 96
Zn-air	1.65	820	1086	6091[e]	$Zn + ½\ O_2 \leftrightarrow ZnO$	2, 97
Al-air	2.70	2980	8100	NA	$4\ Al + 3\ O_2 + 6\ H_2O \leftrightarrow 4\ Al(OH)_3$	97, 98
Mg-air	3.10	2200	6800	NA	$Mg + ½\ O_2 + H_2O \leftrightarrow Mg(OH)_2$	97

[a] the calculations do not include the molecular mass of O_2.
[b] based on the sum of the volumes of Li at the beginning and Li_2S at the end of discharge.
[c] based on the sum of the volumes of Li at the start and Li_2O_2 at the end of discharge.
[d] assuming alkaline conditions and the product is anhydrous LiOH.
[e] based on the volume of ZnO at the end of discharge.

2.8 Li-S BATTERY

The concept of utilizing sulfur as the positive electrode for the electrochemical energy storage in an alkali metal as negative electrode cell dates back to the 1960s[99]. However, investigations on Li-S battery ceased in the 1990s with the triumph of Li-ion batteries (LIBs). After 2000, the rapid development of portable electronic devices and electrification of vehicles made it essential to go beyond LIBs and develop batteries with higher energy density, which leads to the resurgent of Li-S batteries. Li-S batteries have theoretical energy density of 2600 Wh kg^{-1}, calculated based on Li anode and S cathode, which is about five times higher than that of commercial LIBs (387 W h kg^{-1} for $LiCoO_2$/C battery). Additionally, sulfur is abundant, cheap and non-toxic. Furthermore, in the case of overcharge at Li-S cell, polysulfides intermediates located in the cathodes are converted to more highly oxidized species which are transported to the anode where they are reduced back and move to the cathode. This phenomenon acts as a protective mechanism and maintains the cell voltage at a low level. All these qualities make Li-S batteries very attractive for energy storage among the batteries mentioned in Table 2.2, specifically for vehicle electrification and energy storage for the intermittent renewable energy sources such as solar and wind. After Nazar et al.[8] reported Li-S battery with enhanced cycling performance in 2009, Li-S batteries have gained significant attention as promising candidates for next-generation energy storage. Since 2009, more than 1650 research works have been published on Li-S batteries (based on the search result on “Li-S battery” at Web of Science, Thomson Reuters) to investigate and improve electrochemical performance of Li-S batteries for commercialization.

2.8.1 Principles of Li-S Battery

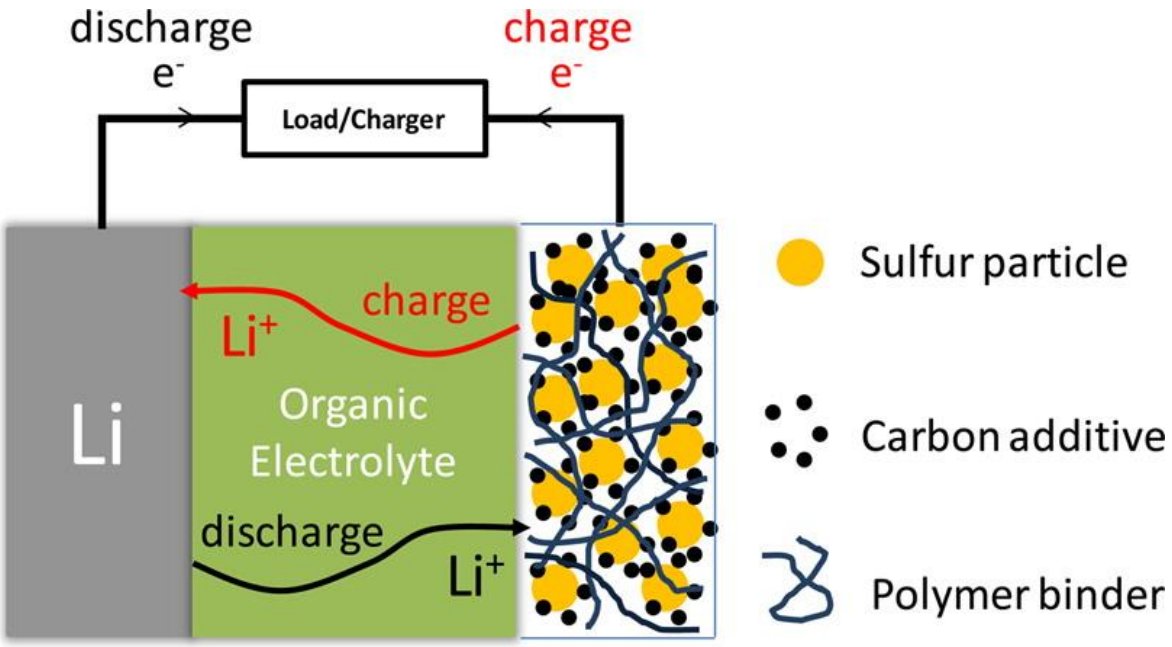

Figure 2.7: Schematic diagram of Li-S cell with its charge-discharge process [100]

Li-S cell is an electrochemical storage device composed of lithium metal anode, sulfur composite cathode, and a solid/liquid electrolyte. The cell operation starts with discharge process as sulfur is in the charged state. The theoretical capacity of Li-S cell is as 1167 mAh g^{-1}, which is calculated based on the theoretical capacities of lithium and sulfur of 3861 and 1672 mAh g^{-1}, respectively[100]. The discharge reaction has an average cell voltage of 2.15 V [100]. Thus, the theoretical gravimetric energy density[101–104] of Li-S cell is 2.51 Wh g^{-1} (Calculations are shown in Appendix A).

Li-S cell has different reaction mechanism than commercial LIBs which follows intercalation-deintercalation mechanism. During discharge process of Li-S cell, lithium metal is oxidized at the negative electrode to produce lithium ions and electrons. The following reaction takes places at the anode or negative electrode:

$2\ Li \rightarrow 2Li^{+} + 2\ e^{-}$ anodic reaction (oxidation, loss of electrons) (Eq. 12)

Produced lithium ions transport to the cathode (positive electrode) through electrolyte internally while electrons travel to the cathode through the external electric circuit, and this is how an electric current is generated. Sulfur gets reduced to generate lithium sulfide by taking the lithium ions and electrons at the cathode. However, this discharge process is a multistage process[105,106]. The overall reactions happen during the discharge process at the cathode, or positive electrode is mentioned below:

$S + 2\ Li^{+} + 2\ e^{-} \rightarrow Li_2S$ cathodic reaction (reduction, gaining of electrons) (Eq. 13)

Overall cell reaction during discharge at Li-S cell:

$2\ Li + S \rightarrow Li_2S$ (Eq. 14)

The backward reaction happens during the charging process.

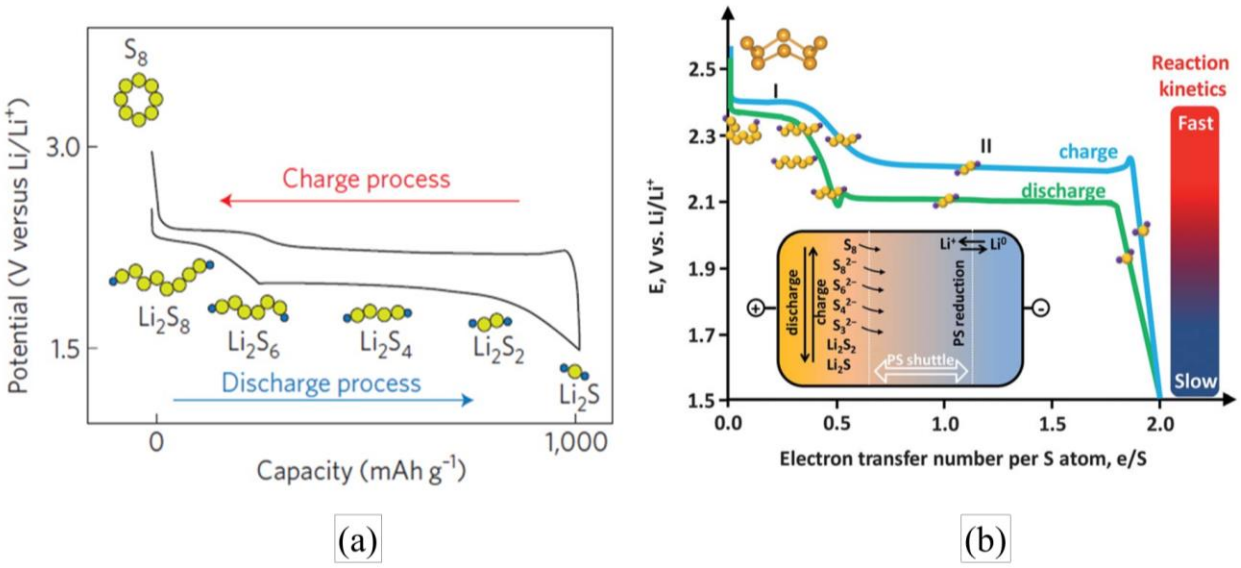

Figure 2.8: (a) Voltage profiles of a Li−S cell[2], (b) electrochemistry of sulfur showing an ideal charge–discharge profile[107] and (inset of b) polysulfides shuttle[107].

The ring-structured cyclo-octasulfur (S_8) is the most stable form of sulfur among the 30 or higher allotropes of sulfur available in the nature[108]. Sulfur atoms are prone to catenation, creating long homoatomic chains or homocyclic rings of various sizes.[109] During ideal discharge process of the fresh Li-S cell, an S–S covalent bond of S_8 is first broken to form a chain-structured polysulfide anion (S_8^{2-}). As the discharge continues, the polysulfide chain length is further shortened as the sulfur is reduced into final discharge product lithium sulfide (Li_2S) through multistage reactions (Figure 2.8a) [105,106]. Different polysulfide anions or radicals, S_8^{2-}, S_7^{2-}, S_6^{2-}, S_5^{2-}, S_4^{2-}, S_3^{2-}, S_2^{2-}, S^{2-}, S_2^{-} and S^{-}, have been observed during the reduction of sulfur in organic solution with different stability and solubility[110]. Higher order lithium polysulfide (Li_2S_x, $4 \leq x \leq 8$) intermediates are soluble in most of the common organic solvents, whereas the lower order lithium sulfides (Li_2S_2 and Li_2S) are insoluble in nature[110–113]. Higher order lithium polysulfides have faster reaction kinetics in comparison with the lower order polysulfides due to the solubility (Figure 2.8a)[107].

2.8.2 Challenges toward Practical Application of Li-S Battery

Although Li-S battery has considerable benefits, the electrochemistry brings noticeable challenges that hinder the practical application of the battery. First, sulfur and its various discharge products (Li_2S_x, x=1–8) exhibit very poor ionic and electronic conductivities, which increase the internal resistance of the battery. This increase results in a significant polarization lead to the poor energy efficiency of the battery. During discharge, insoluble insulation layer composed of Li_2S_2 and Li_2S forms on the surface of the S particles which reduces the conductivity further, and impedes their further reduction, which leads to a poor active material utilization and low capacity[113,114].

The second challenge is associated with the solubility of the long chain polysulfide (PS) ions (S_n^{2-}) formed on the reduction of S_8 or upon oxidation of the end-member sulfides (i.e. Li_2S or Li_2S_2)[115]. The dissolved PS ions (S_n^{2-}) can easily diffuse from the cathode in solution, through the separator to the lithium anode where they are reduced to form insoluble Li_2S or Li_2S_2 [116]. After the lithium anode is fully coated, the next S_n^{2-} reacts with these fully reduced sulfides to form lower order polysulfides (S_{n-x}^{2-}) which become concentrated at the negative electrode side, diffuse back to the cathode and are then re-oxidized into S_n^{2-}.[113] This whole parasitic process takes place repeatedly, which is known as "shuttle phenomenon" (Figure 2.8b-inset)[113]. At the end of each discharge cycle, the soluble polysulfides are reduced and deposit as Li_2S_2/Li_2S precipitates on the cathode. Over prolonged charges and discharges, insoluble and electrochemically insulating agglomerates are thus formed on the cathode surface regardless of the initial cathode morphology. The agglomerates cause an active mass loss at the cathode side and the build-up of impedance layers that leads to capacity fading.[113] Overall, the shuttle phenomenon causes the following drawbacks: (a) the active mass loss from the cathode thus poor active material utilization in the discharge process, (b) significant reduction of Coulombic efficiency in the charging process, and (c) poor capacity retention upon cycling[107,113,117].

The third challenge is associated with the volume variation of the sulfur cathode during lithiation and de-lithiation. The density of sulfur is 2.03 g cm^{-3}, whereas that of Li_2S is 1.67 g cm^{-3}, which causes in an approximate 80% volume expansion during cycling process which leads to fast capacity fading[118,119]. All these limitations lead to poor cycle life, poor active materials utilization, and low Columbic efficiency[4,118–120].

2.8.3 Strategies to Solve the Problem

The role of sulfur as a potential cathode material for the rechargeable battery was first revealed in the early 1960s[121]. Since then, the Li-S battery has been regarded as very promising energy storage with high energy density. However, the development of Li-S is limited due to several challenges such as low utilization of active material, insulating nature of sulfur, volume changes and dissolution of the intermediate products. In recent years, numerous strategies have been developed based on various perspective to overcome the challenges toward achieving high energy density and long cycle life. Some researchers have developed new organic electrolytes for larger capacity [122–124], high Coulombic efficiency [125–127], safer application[128] and long cycle life[129–133]. Other groups have worked on a modification of separator to block soluble polysulfides [134–136] or used the surface coating for Li metal anode protection from the solid electrolyte interface (SEI) layer formation [137–139]. Among all the Li-S battery research works, developing novel S cathode materials and composite attained the highest attention.

2.9 CATHODE MATERIAL FOR Li-S BATTERY

Numerous efforts have been devoted to improving S cathode following various strategies. One of the methods is to compose sulfur with conductive materials to enhance the conductivity and overcome insulating nature of sulfur which increases sulfur utilization[140]. Conductive materials applied to prepare cathode composite electrodes are carbon nanotubes,[141], graphene,[142,143] porous carbon,[9,17,144–148], carbon black [100,149] and conductive polymers.[150–153]. Additionally, others have worked on improving binder portion to introduce conductive binder [154–160], flexible binder [155,158,159,161], binder-free electrode [162,163] or to improve electrode films [149,164–168]. Research has been conducted to design various structures to overcome the Li-S battery challenges

such as yolk-shell or hollow structured cathode material to accommodate the volume expansion of S during cycling [152,169,170], surface coating to block the polysulfides dissolution [118,171–174], introduction of the hosts like metal oxides (TiO_2, Ti_4O_7) and metal organic frameworks (MOFs) to improve the adsorption for sulfur species[175–180]. Some groups also investigated partial charge–discharge methods to control the electrochemical reaction depth for longer cycle life [181–183].

2.9.1 The Role of Porous Materials in Li-S Battery Cathode

Porous materials have gained huge attention in various scientific research fields including materials, chemistry, physics, and biology with the rapid developments made in nanotechnology and nanoscience. In the development of energy storage systems such as Li-ion batteries, Li-air batteries, Li-S batteries, Na-ion cells and supercapacitors, and porous carbons have been investigated widely due to their properties including good conductivity, high specific surface areas, high pore volumes, tunable pore sizes, and abundant frameworks[184,185]. When used as sulfur hosts for Li–S batteries, porous carbon matrix can significantly enhance the electronic conductivity of the composite cathode, trap the dissolved polysulfides and accommodate the volume expansion of the active materials during charge-discharge cycles. [2,8,186,187].

Porous carbon materials can be categorized based on the variation in morphology, pore sizes and pore symmetry into three classes: (a) microporous carbon, (b) mesoporous carbon, and (c) hierarchical porous carbon. The micropores are demonstrated as the ideal container for accommodating and immobilizing the active material[188]. On the other hand, the mesopore can improve sulfur encapsulation as the designed pore size is small or can facilitate lithium ion and electrolyte transport as well as raise the tolerance toward high sulfur loading due to the large pore size.[8,189,190]

(i) Sulfur-Mesoporous Carbon Composites

Most recent research on cathodes focused on utilizing mesoporous carbons[186,190–193], following the early work where small carbon mesopores[8] (3–4 nm) effectively confined of sulfur to reach a reversible capacity of about 1200 mAh g^{-1}. The large pore volume of mesoporous carbon can provide enough space for high sulfur loading rate up to 84% in the composite, and offers better constraint on polysulfides with stronger interactions between the porous channels and sulfur[8,120,193] Moreover, sulfur confined in mesoporous channels exhibits enhanced electrochemical performance due to a much-diminished particle size. Among the various mesoporous substrates available, mesoporous carbon materials are especially promising due to being lightweight, elastic[120] and conductive. Thus, the combination of sulfur and mesoporous carbon has been widely investigated[8,120,186,190–193]. Ji et al.[8] used highly ordered mesoporous carbon (CMK-3) with 2.1 cm^3 g^{-1} pore volume as the sulfur hosts to confine sulfur within resident nanochannels by a melting-diffusion strategy. They mixed and heated the sulfur and CMK-3 together at 155°C. At 155°C, the liquid sulfur had the lowest viscosity, which was easily diffused into the mesopores by capillary action. The CMK-3/S composite had enough space to accommodate the volume expansion of sulfur during lithiation and de-lithiation. The amount of sulfur in the composite was optimized to 60–70%, which was lower than the highest theoretical value (79%). The composite materials exhibited a high initial discharge capacity of 1005 mAh g^{-1}. With the addition of thin-layer polymer of polyethylene glycol (PEG) coating, the composite showed an initial reversible capacity of 1320 mAh g^{-1} and improved cycle performance. Li et al.[190] systematically explored the influences of several pore sizes, pore volumes, and sulfur filling levels on the electrochemical performance of sulfur–mesoporous carbon composite cathode. They reported that mesoporous carbon with different pore volumes exhibited very similar overall battery performance, although,

mesoporous carbon with larger pore volume can hold higher maximum sulfur loading. In comparison with a maximum filling of pores with sulfur, partial filling leads to an improved initial discharge capacity and cycle stability, which could be due to enhanced electrical and ionic transport during electrochemical reactions. He et al.[191] demonstrated that optimizing the parameters of mesoporous carbon, such as the ratio of small pore volume *vs.* the total pore volume and size expansion of large pores could result in unique electrochemical characteristics.

(ii) Sulfur-Microporous Carbon Composite

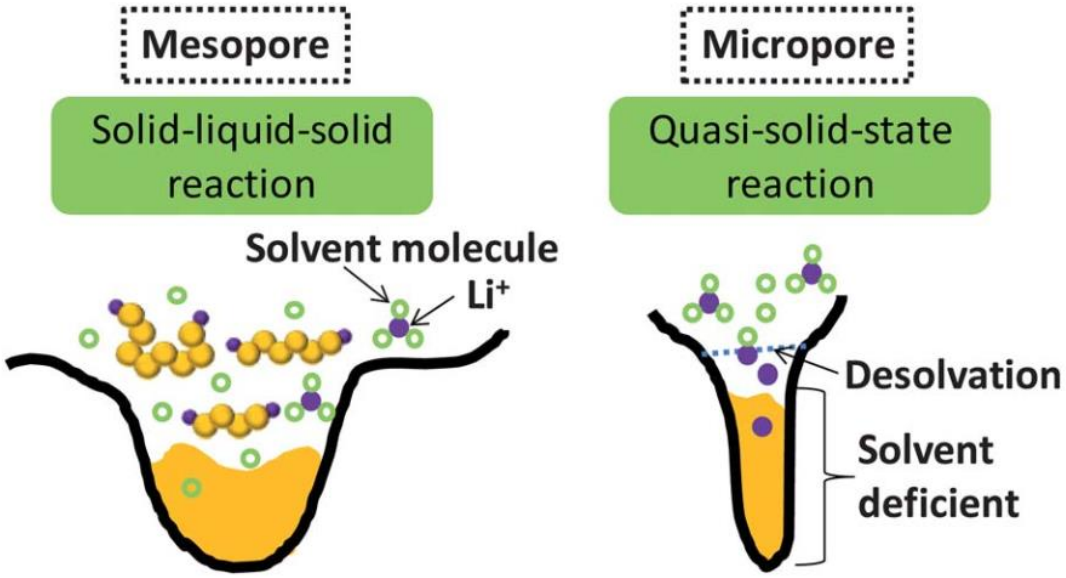

Figure 2.9: **Illustration of the different lithiation mechanisms of sulfur encapsulated in mesopores and micropores.[107]**

Although the mesoporous carbon materials have managed to prepare stable sulfur cathodes with high sulfur loading, the challenges of polysulfide dissolution and shuttles cannot be eliminated due to the presence of the electrochemistry of cyclo-S_8 in the systems[120]. Recently, microporous carbon materials have been widely investigated for an optimal confinement of sulfur

and polysulfides[9,62,188,194–198]. Microporous carbon structure has pore sizes up to 2 nm and can encapsulate smaller sizes of sulfur[198]. Additionally, the developed microporous structure improves both the diffusion and adsorption of the molten sulfur during the melt-diffusion process and the facile distribution of the electrolyte throughout the porous structure of carbon during cycling. Moreover, micropores in the composite act as microporous reactors and restrict the dissolution of lithium polysulfides in the organic electrolyte [9]. Through several investigations, researchers have observed that all the sulfur–microporous carbon electrodes show the similar electrochemical characteristics, such as lower voltage discharge plateau and the electrolyte adaptability, and so on, which are very different from other nano-sized sulfur materials[196]. In comparison with conventional S-based electrodes, S–microporous carbon composite exhibits very different electrochemical characteristics when the pore size of carbon matrix decreases to micropore scale, especially around 0.5 nm. This S-microporous carbon composite cathode system shows a lower voltage discharge plateau, and the S content in the composite should be less than a certain level to obtain good electrochemical performance [196]. Melt or amorphous state elemental sulfur is in a linear chain configuration at high temperature[199]. Therefore, the narrow micropores of carbon structure can accommodate several S_8 crown rings or/and short chains of elemental sulfur in the low molecular forms, [194,195] which can assure a high dispersion of elemental sulfur inside the micropores[188]. However, the challenges resulted from the electrochemistry of cyclo-S_8 still could not be fully eliminated. Guo et al.[198] fabricated carbon nanotube backbone based carbon nanofibers with tiny 0.5–0.6 nm micropores to confine metastable sulfur allotropes $S_{2–4}$. They proposed that the sulfur encapsulated in the micropores exists in small molecular forms as $S_{2–4}$ due to the space limitation. Thus, the microporous carbon–$S_{2–4}$ composite could avoid the unfavorable transition between large S_8 and $S_4^{2–}$ and deliver a very stable electrochemical performance. Wang et al.[197]

observed the greater binding energy of Li–S bond confined in micropores due to the strong adsorption. They also proposed a desolvation effect to understand the unusual stability (up to 800 cycles at 1.8°C rate) of micropore confined sulfur composite they prepared. Micropores smaller than 1 nm caused the desolvation of the electrolyte ions and, that prevented or slowed the dissolution of polysulfide as the solvent concentration is very low or likely to be close to zero in these micropores, which suggests a quasi-solid-state reaction of the sulfur under solvent-limited conditions[200] (Figure 2.9). The low Li^+ conductivity in S and solid sulfides could also explain the retarded lithiation of sulfur in micropores[200].

(iii) Sulfur–Hierarchical Porous Carbon Composites

Hierarchical porous carbon combines the advantages of micropores in regards to better stability and mesopore that enhances rapid ion transport[189]. Liang et al. [189] prepared bimodal porous carbon with a uniform distribution of mesopores of 7.3 nm and micropores of less than 2 nm. At first, they created the mesopores following soft-template method and later, added micropores through KOH activation process. The mesoporosity provided high surface area, and the micropore volume functioned as a retainer that contained the sulfur species at the cathode region. Additionally, the mesoporosity provided a facile pathway for the mass transport of Li ions and thus, resulted in a high ionic conductivity to the cathode. Therefore, the cells could discharge and charge at a high current density without sacrificing the cell capacity. Ding et al. [201] fabricated a sucrose derived 3D hierarchical porous carbon with mesoporous walls and interconnected macropores using self-assembly of colloidal polymer and silica spheres. With 50% sulfur loading, the composite delivered a high initial specific capacity of 1193 mAh g^{-1} at 0.1 C rate and 884 mAh g^{-1} after 50 cycles. They attributed this electrochemical performance to the integration

of the mesopores and macropores. The mesoporous walls functioned as solvent-restricted reactors for the redox reaction of sulfur and helped in restraining the diffusion of polysulfide species into the electrolyte[201]. Additionally, the "open" ordered interconnected macropores and windows enhance the transportation of electrolyte and solvated Li^+ ions during the cycling process.

2.9.1 Effect of Heteroatoms-Doping

The high electrical conductivity of porous carbon can conquer the electrical insulation of sulfur and its discharge products. Further addition of ultra-high conductive carbon additive (e.g. Super-P carbon black) can further increase the electronic conductivity and in addition to that the utilization of sulfur in the underlying electrochemical process. The large pore volume of porous carbon can provide sufficient space to accommodate volume expansion of sulfur during cycling. Most importantly, the micro-, meso-, macro- or hierarchical pore structures and abundant porosity of porous carbon materials can trap lithium polysulfides (PS) by physical adsorption. However, physical adsorption through weak van der Waals interactions is not strong enough to restrict the dissolution of PS very long because the migration of soluble PS anions is driven by the strong electrical field, eventually leading to the capacity fading over medium-term cycling.

Besides the structural characteristics (such as pore shapes, pore size, pore volume and surface area), the intrinsic properties (such as electronic conductivity, surface chemistry, and surface polarization) also play a significant role in the electrochemical performance of porous carbon–sulfur composite cathodes. Recently, chemical modifications of porous carbon materials by introducing heteroatoms (such as N, O, B, S, and P) doping have been exhibited great potential for lithium polysulfides immobilization through strong chemical binding and altering the electrochemical performance of Li-S cell.[202–206]

(i) Effect of Nitrogen-Doping

The nitrogen (N) atoms, possessing a comparable atomic size and five valence electrons for bonding with carbon atoms, have been widely used for the doping of carbon-based materials. The well-bonded N atom provides more active sites to increase the interaction between carbon and adsorbents. Thus, it is expected to enhance the electrochemical performance. Recently, N-doping of carbon matrix has shown noticeable potential for immobilizing sulfur and reducing the dissolution of polysulfide intermediates through strong Li-N interactions as well as for enhancing the electrical conductivity and wettability of carbon materials [20,144,207–215]. Sun et al.[216] reported that the sulfur reduction potential and current density were much higher in the N-doped mesoporous carbon-sulfur composite than those without N-doping, which indicated easy and enhanced sulfur reduction activities in the N-doped composite. They also found that N-doped composite had much lower charge-transfer resistance and offered faster charge-transfer kinetics. Sun et al.[217] prepared a series of mesoporous carbons with tunable N content (0.0 to 11.9%) by a colloid silica nano-casting method. They found that N-doping only within an appropriate level (e.g. 4.0-8.0%) can improve the electronic conductivity of the carbon matrix and offer faster charge transfer kinetics. They also concluded that N-doping could enhance the surface interaction between the core nitrogen functionalities and polysulfide species, and the dopant N can assist mesoporous carbon to restrict the shuttling phenomenon. Song et al.[212] demonstrated that N-doping promotes the formation of chemical bonds between sulfur atoms and oxygen functional groups on the carbon. This facilitates the uniform initial distribution and re-deposition of sulfur in the carbon structure during sulfur loading at 155°C and improves cycle stability. On their later work, Song et al.[214] directly utilized the functional groups of N-doped carbon to adsorb soluble Li_2S_x in the absence of a thermal treatment of the sulfur and doped carbon material. They demonstrated that

the adsorption mechanism to be related to the electron-donating ability of the doped nitrogen atoms. They also suggested that the doping of electron-rich elements can further enhance the performance of Li-S battery in future. Qiu et al.[218] reported that among the three type of N doping (such as pyridinic-N, pyrrolic N, and graphitic N) which can be detected using XPS, pyridinic-N and pyrrolic N are more effective in forming $S_xLi•••N$ interactions via the N lone pair electrons. This strong interaction may alleviate the dissolution of lithium polysulfides in the electrolyte and improve their re-deposition process upon discharge/charge, thereby enhancing the performance of the Li-S cells[218–220]. They also observed that the strong interaction is mainly caused by the ionic attractions between N and Li cations, rather than that between N and S anions.

2.9.3 Biomass-Derived Porous Carbon for Li-S Battery Cathode

Many research works have been performed in the last few years to develop facile, environment-friendly and cost effective biomass carbon with a high electrochemical performance for Li-S battery. Wei et al. [17] fabricated hierarchical porous carbons from renewable and inexpensive pig bone, which is a kind of natural organic–inorganic composite. They investigated the effects of activation temperature on the textural properties of the pig bone based carbons. Pig bones were washed, dried and carbonized at 450°C, followed by mixing with KOH (1:1 weight ratio) and activating at temperature varied from 650 to 950°C. During the activation, the organic component acts as the carbon source, while the inorganic component plays the role of a natural template for the formation of hierarchical pores. Pore sizes were ranging from micropores (0.6–2.0 nm), mesopores (2–10 nm) to macropores (~100 nm). Depending on activation temperature, the specific surface area and average pore volume varied from 703 to 2157 $m^2 g^{-1}$ and 0.57 to 2.26 $cm^3 g^{-1}$, respectively. The cathode composite was prepared by ball milling of 63% elemental

sulfur, 7% gelatin binder, 24 % acetylene black and 6% pig boned derived carbon. Pig bone derived carbon prepared at 850°C was used since it had highest surface area and pore volume. For temperature, greater than 750°C, the surface area and micropore volume dramatically increased, which was due to the production of CO_2 from K_2CO_3 decomposition at temperatures above 700°C to further porosity development through carbon gasification. The composite in the Li–S batteries exhibited a high initial capacity of 1265 mAh g^{-1} and retained 643 mAh g^{-1} after 50 cycles. Other than pig bone, several other biomass derived carbons are also investigated for Li-S battery such as bamboo[9], rice husk[221], soybean hulls and residue, gelatin and soluble starch.

2.9.4 Nitrogen-Rich Biomass Derived Porous Carbons for Li-S Battery

Incorporation of nitrogen into the carbon matrix often involves the procedures of hydrothermal, ultrasonic and electrochemical approaches, which cause some challenges. Besides, the use of toxic reagents results in severe environmental issues. To resolve this problem, preparation of nitrogen-containing carbon from abundant natural sources with ample amounts of nitrogen seems more appealing.[222] Recently, several investigations have been performed to synthesize heteroatoms doped (especially nitrogen) porous carbon from biomass for batteries and supercapacitors applications. Protein is a biopolymer contains the highest concentration of nitrogen in bio-organisms[72]. Biomass sources with high protein content are utilized as the precursor for N-doped porous carbon. A high N content without any doping can afford strong electronegativity and interactions between the Li and the carbon network, which enhances the electronic conductivity and electrochemical stability[223] The electrochemical performance of porous carbons can be further enhanced by surface functionalities (such as P, N and B)[223]. Chen et al.[65] fabricated a honeycomb-like nitrogen and oxygen dual-doped porous carbon from soybean

residue, with a large specific surface area (2690.3 $m^2 g^{-1}$), high pore volume (1.34 $cm^3 g^{-1}$), through carbonizing at 400˚C followed by KOH-activation at 750˚C. Soybean residue with 50% of proteins served as carbon, nitrogen, and oxygen rich precursors. The X-ray photoelectron spectroscopy (XPS) result showed the presence of three different compositions of nitrogen groups such as graphitic N, pyrrolic N, and pyridinic N. Carbon, nitrogen, and oxygen contents obtained from XPS results in the porous carbon were 89.93 at%, 2.02 at%, and 8.04 at%, respectively. This composite with 51.6% sulfur content exhibited the first and the 600th cycle discharge capacities of 698.5 mAh g^{-1} and 435.7 mAh g^{-1}, respectively at the 1 C rate. Some of the significant research works that have been performed using biomass derived carbon for Li-S battery cathode have been shown in Table 2.3.

Table 2.3: Summary of biomass-derived carbon for Li–S batteries

Biomass	Carbon structure	Preparation	Electrode Preparation	S load[a]	SSA[b]	PV[c]	S[d]	Electrolyte and voltage range[e]	Electrochemical Performance	Ref
Pig bone	Hierarchical	KOH activation at 850°C	Ball milling; 63% S and 6% porous carbon	-	2157	2.26	63	1 M $LiClO_4$ in DME /DOL (v/v =2/1); 1.5-2.8V	1265 mAh g^{-1} initial discharge capacity; 643 mAh g^{-1} after 50 cycles	17
White part of pomelo peel	Bimodal micro-mesoporous activated carbon foam with PD 2nm and 3nm	KOH activation at 600°C;	Solution infiltration method by toluene; later heated at 155°C for 24h followed by 2h at 300°C.	5.1	1533	0.83	60	1M LiTFSI and 0.1 M $LiNO_3$ in DME	1258 mAh g^{-1} initial discharge capacity at 0.2C; 750mAh g^{-1} after 100 cycles	79
Soluble starch	Mesoporous	Sol-gel route using colloidal silica template; carbonized at 1000°C; Removed template by HF	Melting-infusion process using CS_2; heated at 155°C for 12h followed by 2h at 250°C; 80% composite	1.3	950	3.14	81.3	1M LiTFSI and 0.1 M $LiNO_3$ in DME /DOL (v/v =1/1); 1.8-3.0V	922 mAh g^{-1} initial discharge capacity; 683 mAh g^{-1} after 100 cycles at 0.5 C; 483 mAh g^{-1} after 300 cycles at 1C	224
Bam-boo	Microporous	KOH activation at 700°C	Melt-diffusion at 155°C; 70% composite	4	792	0.38	50	1M LiTFSI and 0.1 M $LiNO_3$ in DME /DOL (v/v =1/1); 1.5-3.0V	1295 mAh g^{-1} initial discharge capacity at 160mA g^{-1}; 550 mAh g^{-1} after 150 cycles 800mA g^{-1}	9

[a] sulfur loading in the electrode in mg cm^{-2}; [b] BET specific surface area in m^2 g^{-1}; [c] pore volume in cm^3 g^{-1}; [d] sulfur loading in total electrode
[e] the voltage range at which charge-discharge cycles were performed; **PD is Pore diameter or pore width in nm

Table 2.3: Summary of biomass-derived carbon for Li–S batteries (Continued)

Biomass	Carbon structure	Preparation	Electrode Preparation	S load[a]	SSA[b]	PV[c]	S[d]	Electrolyte and voltage range[e]	Electrochemical Performance	Ref
Coconut shells	microporous structure with small mesoporous inclusion; 2.246 APD	KOH activation at 750°C;	Melt-diffusion at 155°C; 80% composite;	-	2258	1.23	62	1M LiTFSI and 0.25 M $LiNO_3$ in DME /DOL (v/v =1/1); 1.7-2.8V	1233 mAh g^{-1} initial discharge capacity at 200mA g^{-1}; 929 mAh g^{-1} after 100 cycles	78
Soybean hulls	Micro-mesoporous carbon	KOH activation at 700°C;	Melt-diffusion at 155°C; 70% composite;	1.5	1232	0.54	63.7	1M LiTFSI and 1% $LiNO_3$ in DME /DOL (v/v =1/1); 1.7-2.8V	1231 mAh g^{-1} initial discharge capacity at 0.5C; 450mAh g^{-1} after 200 cycles	225
Banana peel	Micropores and Small Mesopores; 0.6 to 5nm PD	KOH activation at 800°C; washed with HF.	Melt-diffusion at 155°C; 80% composite; 0.4mm thickness	-	2741	1.23	65	1M LiTFSI and 0.1% $LiNO_3$ in DME /DOL (v/v =1/1);	1200 mAh g^{-1} initial discharge capacity; 570 mAh g^{-1} after 500 cycles at 1C	226
Soybean residue	Honeycomb like N,O-dual doped micro-mesoporous with 2.01 APD	KOH activation at 750°C	Melt-diffusion at 155°C for 20h followed by 2h at 220°C; 80% composite	1.2-1.5	2690	1.34	64.5	1M LiTFSI and 0.1 M $LiNO_3$ in DME /DOL (v/v =1/1); 1.7-2.8V	1185 mAh g^{-1} initial discharge capacity at 0.2C; 435.7 mAh g^{-1} after 600 cycles	65
Bamboo Leaves	Hierarchical	Annealed at 800°C; 5% HF to remove SiO_2	Melt-diffusion at 155°C; 80% composite; 15 µm thickness	1.8	284	0.6	70.3	1M LiTFSI and 1% $LiNO_3$ in DME /DOL (v/v =1/1); 1.7-2.8V	1487 mAh g^{-1} initial discharge capacity at 0.05C; 707 mAh g^{-1} after 200 cycles at 1C	227

References:

1. *Annual Energy Outlook 2017*. (2017).
2. Bruce, P. G., Freunberger, S. a., Hardwick, L. J. & Tarascon, J.-M. Li–O2 and Li–S batteries with high energy storage. *Nat. Mater.* **11,** 172–172 (2011).
3. Chen, L. & Shaw, L. L. Recent advances in lithium-sulfur batteries. *J. Power Sources* **267,** 770–783 (2014).
4. Li, Z., Huang, Y., Yuan, L., Hao, Z. & Huang, Y. Status and prospects in sulfur–carbon composites as cathode materials for rechargeable lithium–sulfur batteries. *Carbon N. Y.* **92,** 41–63 (2015).
5. Schuster, J., He, G., Mandlmeier, B., Yim, T., Lee, K. T., Bein, T., & Nazar, L. F. Spherical ordered mesoporous carbon nanoparticles with high porosity for lithium-sulfur batteries. *Angew. Chemie - Int. Ed.* **51,** 3591–3595 (2012).
6. Jayaprakash, N., Shen, J., Moganty, S. S., Corona, A. & Archer, L. A. Porous hollow carbon@sulfur composites for high-power lithium-sulfur batteries. *Angew. Chemie - Int. Ed.* **50,** 5904–5908 (2011).
7. He, G., Ji, X. & Nazar, L. High 'C' rate Li-S cathodes: sulfur imbibed bimodal porous carbons. *Energy Environ. Sci.* **4,** 2878 (2011).
8. Ji, X., Lee, K. T. & Nazar, L. F. A highly ordered nanostructured carbon-sulphur cathode for lithium-sulphur batteries. *Nat. Mater.* **8,** 500–506 (2009).
9. Gu X, Wang Y, Lai C, Qiu J, Li S, Hou Y, Martens W, Mahmood N & Zhang S. Microporous bamboo biochar for lithium-sulfur batteries. *Nano Res.* **8,** 129–139 (2014).
10. Liang, Y. *et al.* Ultrahigh surface area hierarchical porous carbons based on natural well-defined macropores in sisal fibers. *J. Mater. Chem.* **21,** 14424 (2011).
11. Ronsse, F., van Hecke, S., Dickinson, D. & Prins, W. Production and characterization of slow pyrolysis biochar: Influence of feedstock type and pyrolysis conditions. *GCB Bioenergy* **5,** 104–115 (2013).
12. Crombie, K., Mašek, O., Sohi, S. P., Brownsort, P. & Cross, A. The effect of pyrolysis conditions on biochar stability as determined by three methods. *GCB Bioenergy* **5,** 122–131 (2013).
13. Yoder, J., Galinato, S., Granatstein, D. & Garcia-Pérez, M. Economic tradeoff between biochar and bio-oil production via pyrolysis. *Biomass Bioenergy* **35,** 1851–1862 (2011).
14. Sohi, S. P., Krull, E., Lopez-Capel, E. & Bol, R. *A review of biochar and its use and function in soil*. *Advances in Agronomy* **105,** (Elsevier Inc., 2010).
15. Qian, K., Kumar, A., Zhang, H., Bellmer, D. & Huhnke, R. Recent advances in utilization of biochar. *Renew. Sustain. Energy Rev.* **42,** 1055–1064 (2015).
16. Suliman, W. *et al.* Influence of feedstock source and pyrolysis temperature on biochar bulk and surface properties. *Biomass Bioenergy* **84,** 37–48 (2016).
17. Wei, S. *et al.* Pig bone derived hierarchical porous carbon and its enhanced cycling performance of lithium–sulfur batteries. *Energy Environ. Sci.* **4,** 736 (2011).
18. Vu, D.-L., Seo, J.-S., Lee, H.-Y. & Lee, J.-W. Activated carbon with hierarchical micro–mesoporous structure obtained from rice husk and its application for lithium–sulfur batteries. *RSC Adv.* **7,** 4144–4151 (2017).
19. Jiang, Q. *et al.* Biomass carbon micro/nano-structures derived from ramie fibers and corncobs as anode materials for lithium-ion and sodium-ion batteries. *Appl. Surf. Sci.* **379,** 73–82 (2016).

20. Qu, J. *et al.* Nitrogen-doped porous 'green carbon' derived from shrimp shell: Combined effects of pore sizes and nitrogen doping on the performance of lithium sulfur battery. *J. Alloys Compd.* **671,** 17–23 (2016).
21. Imtiaz, S. *et al.* Biomass-derived nanostructured porous carbons for lithium-sulfur batteries. *Sci. China Mater.* **59,** 389–407 (2016).
22. Guo, J. *et al.* Microporous carbon nanosheets derived from corncobs for lithium–sulfur batteries. *Electrochim. Acta* **176,** 853–860 (2015).
23. Kloss, S. *et al.* Characterization of slow pyrolysis biochars: effects of feedstocks and pyrolysis temperature on biochar properties. *J. Environ. Qual.* **41,** 990–1000 (2011).
24. Ahmad, M. *et al.* Biochar as a sorbent for contaminant management in soil and water: A review. *Chemosphere* **99,** 19–23 (2014).
25. Hu, B. *et al.* Engineering carbon materials from the hydrothermal carbonization process of biomass. *Adv. Mater.* **22,** 813–828 (2010).
26. a.V. Bridgwater, Meier, D. & Radlein, D. An overview of fast pyrolysis of biomass. *Org. Geochem.* **30,** 1479–1493 (1999).
27. Basu, P. *Biomass gasification and pyrolysis: practical design and theory*. (Academic press, 2010).
28. Brewer, C. E., Schmidt-Rohr, K., Satrio, J. A. & Brown, R. C. Characterization of biochar from fast pyrolysis and gasification systems. *Environ. Prog. Sustain. Energy* **28,** 386–396 (2009).
29. Azargohar, R., Nanda, S., Rao, B. V. S. K. & Dalai, A. K. Slow pyrolysis of deoiled canola meal: Product yields and characterization. *Energy and Fuels* **27,** 5268–5279 (2013).
30. Li, J. *et al.* Biochar from microwave pyrolysis of biomass: A review. *Biomass Bioenergy* **94,** 228–244 (2016).
31. Lei, H., Ren, S. & Julson, J. The effects of reaction temperature and time and particle size of corn stover on microwave pyrolysis. *Energy and Fuels* **23,** 3254–3261 (2009).
32. Sadhwani, N., Adhikari, S., Eden, M. R., Wang, Z. & Baker, R. Southern pines char gasification with CO2-Kinetics and effect of alkali and alkaline earth metals. *Fuel Process. Technol.* **150,** 64–70 (2016).
33. Roddy, D. J. & Manson-Whitton, C. *Biomass gasification and pyrolysis*. *Comprehensive Renewable Energy* **5,** (2012).
34. Sadhwani, N., Adhikari, S. & Eden, M. R. Biomass Gasification Using Carbon Dioxide: Effect of Temperature, CO2/C Ratio, and the Study of Reactions Influencing the Process. *Ind. Eng. Chem. Res.* **55,** 2883–2891 (2016).
35. Mullaney, H., Farag, I., LaClaire, C. & Barrett, C. Technical, environmental and economic feasibility of bio-oil in New Hampshire's north country. *UNH Proj.* (2002).
36. Yang, H., Yan, R., Chen, H., Lee, D. H. & Zheng, C. Characteristics of hemicellulose, cellulose and lignin pyrolysis. *Fuel* **86,** 1781–1788 (2007).
37. Demirbas, A. & Arin, G. An overview of biomass pyrolysis. *Energy sources* **24,** 471–482 (2002).
38. Ahmad, M. *et al.* Biochar as a sorbent for contaminant management in soil and water: A review. *Chemosphere* **99,** 19–23 (2014).
39. Demirbas, A. & Arin, G. An Overview of Biomass Pyrolysis. *Energy Sources* **24,** 471–482 (2002).
40. Mohan, D., Pittman, C. U. & Steele, P. H. Pyrolysis of Wood / Biomass for Bio-oil : A Critical Review. *Energy & Fuesl* **20,** 848–889 (2006).

41. Kang, B. S., Lee, K. H., Park, H. J., Park, Y. K. & Kim, J. S. Fast pyrolysis of radiata pine in a bench scale plant with a fluidized bed: Influence of a char separation system and reaction conditions on the production of bio-oil. *J. Anal. Appl. Pyrolysis* **76,** 32–37 (2006).
42. Jung, S. H., Kang, B. S. & Kim, J. S. Production of bio-oil from rice straw and bamboo sawdust under various reaction conditions in a fast pyrolysis plant equipped with a fluidized bed and a char separation system. *J. Anal. Appl. Pyrolysis* **82,** 240–247 (2008).
43. Zhao, L., Cao, X., Mašek, O. & Zimmerman, A. Heterogeneity of biochar properties as a function of feedstock sources and production temperatures. *J. Hazard. Mater.* **256,** 1–9 (2013).
44. Fu, P. *et al.* Effects of pyrolysis temperature on characteristics of porosity in biomass chars. *2009 Int. Conf. Energy Environ. Technol. ICEET 2009* **1,** 109–112 (2009).
45. Bruun, E. W., Müller-Stöver, D., Ambus, P. & Hauggaard-Nielsen, H. Application of biochar to soil and N2O emissions: potential effects of blending fast-pyrolysis biochar with anaerobically digested slurry. *Eur. J. Soil Sci.* **62,** 581–589 (2011).
46. Mašek, O., Brownsort, P., Cross, A. & Sohi, S. Influence of production conditions on the yield and environmental stability of biochar. *Fuel* **103,** 151–155 (2013).
47. Song, W. & Guo, M. Quality variations of poultry litter biochar generated at different pyrolysis temperatures. *J. Anal. Appl. Pyrolysis* **94,** 138–145 (2012).
48. Spokas, K. A. *et al.* Biochar: a synthesis of its agronomic impact beyond carbon sequestration. *J. Environ. Qual.* **41,** 973–989 (2012).
49. Klüpfel, L., Keiluweit, M., Kleber, M. & Sander, M. Redox properties of plant biomass-derived carbon black (biochar). *Env. Sci Technol* **48,** 5601–5611 (2014).
50. Major, J., Lehmann, J., Rondon, M. & Goodale, C. Fate of soil-applied black carbon: Downward migration, leaching and soil respiration. *Glob. Chang. Biol.* **16,** 1366–1379 (2010).
51. Hanafi, M. M., Eltaib, S. M. & Ahmad, M. B. Physical and chemical characteristics of controlled release compound fertiliser. *Eur. Polym. J.* **36,** 2081–2088 (2000).
52. Mortain, L. Development of new composites materials, carriers of active agents, from biodegradable polymers and wood. *Comptes Rendus Chim.* **7,** 635–640 (2004).
53. Oh, T.-K., Shinogi, Y., Lee, S.-J. & Choi, B. Utilization of biochar impregnated with anaerobically digested slurry as slow-release fertilizer. *J. Plant Nutr. Soil Sci.* **177,** 97–103 (2014).
54. Yao, Y., Gao, B., Chen, J. & Yang, L. Engineered biochar reclaiming phosphate from aqueous solutions: Mechanisms and potential application as a slow-release fertilizer. *Environ. Sci. Technol.* **47,** 8700–8708 (2013).
55. Kim, P., Hensley, D. & Labbé, N. Nutrient release from switchgrass-derived biochar pellets embedded with fertilizers. *Geoderma* **232–234,** 341–351 (2014).
56. Uchimiya, M., Wartelle, L. H., Klasson, K. T., Fortier, C. a. & Lima, I. M. Influence of pyrolysis temperature on biochar property and function as a heavy metal sorbent in soil. *J. Agric. Food Chem.* **59,** 2501–2510 (2011).
57. Mohan, D. *et al.* Sorption of arsenic, cadmium, and lead by chars produced from fast pyrolysis of wood and bark during bio-oil production. *J. Colloid Interface Sci.* **310,** 57–73 (2007).
58. Lebrero, R., Rodríguez, E., García-Encina, P. a. & Muñoz, R. A comparative assessment of biofiltration and activated sludge diffusion for odour abatement. *J. Hazard. Mater.* **190,** 622–630 (2011).

59. Bagreev, A. & Bandosz, T. J. H2S adsorption/oxidation on unmodified activated carbons: importance of prehumidification. *Carbon N. Y.* **39,** 2303–2311 (2001).
60. Azargohar, R. & Dalai, A. K. The direct oxidation of hydrogen sulphide over activated carbons prepared from lignite coal and biochar. *Can. J. Chem. Eng.* **89,** 844–853 (2011).
61. Shang, G., Shen, G., Liu, L., Chen, Q. & Xu, Z. Kinetics and mechanisms of hydrogen sulfide adsorption by biochars. *Bioresour. Technol.* **133,** 495–499 (2013).
62. Chmiola, J. *et al.* Anomalous increase in carbon capacitance at pore sizes less than 1 nanometer. *Science (80-.).* **313,** 1760–1763 (2006).
63. Jiang, J. *et al.* Highly ordered macroporous woody biochar with ultra-high carbon content as supercapacitor electrodes. *Electrochim. Acta* **113,** 481–489 (2013).
64. Zhang, L., Jiang, J., Holm, N. & Chen, F. Mini-chunk biochar supercapacitors. *J. Appl. Electrochem.* **44,** 1145–1151 (2014).
65. Chen, F., Yang, J., Bai, T., Long, B. & Zhou, X. Biomass waste-derived honeycomb-like nitrogen and oxygen dual-doped porous carbon for high performance lithium-sulfur batteries. *Electrochim. Acta* **192,** 99–109 (2016).
66. R., A. & A. K., D. Biochar As a Precursor of Activated Carbon. *Appl. Biochem. Biotechnol.* **131,** 762–773 (2006).
67. Hassler, J. W. Purification with activated carbon; industrial, commercial, environmental. (1974).
68. McDougall, G. J. Physical nature and manufacture of activated carbon. *J. South African Inst. Min. Metall.* **91,** 109–120 (1991).
69. Marsh, H. & Reinoso, F. R. *Activated carbon*. (Elsevier, 2006).
70. Rouquerol, J. *et al.* Recommendations for the characterization of porous solids (Technical Report). *Pure Appl. Chem.* **66,** 1739–1758 (1994).
71. Klobes, P., Meyer, K. & Munro, R. G. Porosity and specific surface area measurements for solid materials. (2006).
72. Li, Z. *et al.* Mesoporous nitrogen-rich carbons derived from protein for ultra-high capacity battery anodes and supercapacitors. *Energy Environ. Sci.* **6,** 871–878 (2013).
73. Dutta, S. *et al.* Hierarchically porous carbon derived from polymers and biomass: effect of interconnected pores on energy applications. *Energy Environ. Sci.* **8,** 1576–1583 (2014).
74. Shams, S. S., Zhang, L. S., Hu, R., Zhang, R. & Zhu, J. Synthesis of graphene from biomass: A green chemistry approach. *Mater. Lett.* **161,** 476–479 (2015).
75. Ioannidou, O. & Zabaniotou, A. Agricultural residues as precursors for activated carbon production-A review. *Renew. Sustain. Energy Rev.* **11,** 1966–2005 (2007).
76. Hoseinzadeh Hesas, R., Wan Daud, W. M. A., Sahu, J. N. & Arami-Niya, A. The effects of a microwave heating method on the production of activated carbon from agricultural waste: A review. *J. Anal. Appl. Pyrolysis* **100,** 1–11 (2013).
77. Wang, J. & Kaskel, S. KOH activation of carbon-based materials for energy storage. *J. Mater. Chem.* **22,** 23710 (2012).
78. Liu, M. *et al.* Biomass-derived Activated Carbon for Rechargeable Lithium-Sulfur Batteries. *Bioresources* **10,** 155–168 (2015).
79. Zhang, J. *et al.* Biomass derived activated carbon with 3D connected architecture for rechargeable lithium - Sulfur batteries. *Electrochim. Acta* **116,** 146–151 (2014).
80. Raja, M., Angulakshmi, N. & Stephan, A. M. Sisal-derived activated carbons for cost-effective lithium–sulfur batteries. *RSC Adv.* **6,** 13772–13779 (2016).
81. Kyotani, T. Control of pore structure in carbon. *Carbon N. Y.* **38,** 269–286 (2000).

82. Lima, I. M., Boateng, A. A. & Klasson, K. T. Physicochemical and adsorptive properties of fast-pyrolysis bio-chars and their steam activated counterparts. *J. Chem. Technol. Biotechnol.* **85,** 1515–1521 (2010).
83. Yahya, M. A., Al-Qodah, Z. & Ngah, C. W. Z. Agricultural bio-waste materials as potential sustainable precursors used for activated carbon production: A review. *Renew. Sustain. Energy Rev.* **46,** 218–235 (2015).
84. Li, W. *et al.* Effects of carbonization temperatures on characteristics of porosity in coconut shell chars and activated carbons derived from carbonized coconut shell chars. *Ind. Crops Prod.* **28,** 190–198 (2008).
85. Wennerberg, A. N. & O'Grady, T. M. Active carbon process and composition. 7 (1978).
86. Otowa, T., Tanibata, R. & Itoh, M. Production and adsorption characteristics of MAXSORB: High-surface-area active carbon. *Gas Sep. Purif.* **7,** 241–245 (1993).
87. Lillo-Ródenas MA, Cazorla-Amorós D, & Linares-Solano A. Understanding chemical reactions between carbons and NaOH and KOH: An insight into the chemical activation mechanism. *Carbon N. Y.* **41,** 267–275 (2003).
88. Romanos, J. *et al.* Nanospace engineering of KOH activated carbon. *Nanotechnology* **23,** 15401 (2011).
89. Hayashi, J., Kazehaya, A., Muroyama, K. & Watkinson, A. P. Preparation of activated carbon from lignin by chemical activation. *Carbon N. Y.* **38,** 1873–1878 (2000).
90. Nieto-Delgado, C. & Rangel-Mendez, J. R. In situ transformation of agave bagasse into activated carbon by use of an environmental scanning electron microscope. *Microporous Mesoporous Mater.* **167,** 249–253 (2013).
91. Ma, Y. Comparison of Activated Carbons Prepared from Wheat Straw via ZnCl2 and KOH Activation. *Waste and Biomass Valorization* **8,** 549–559 (2017).
92. Qian, Q., MacHida, M., Aikawa, M. & Tatsumoto, H. Effect of ZnCl2 impregnation ratio on pore structure of activated carbons prepared from cattle manure compost: Application of N 2 adsorption-desorption isotherms. *J. Mater. Cycles Waste Manag.* **10,** 53–61 (2008).
93. Demiral, H., Demiral, I., Tümsek, F. & Karabacakoğlu, B. Pore structure of activated carbon prepared from hazelnut bagasse by chemical activation. *Surf. Interface Anal.* **40,** 616–619 (2008).
94. Linden, D. & Reddy, T. B. Handbook of battery. (2001).
95. Bock, D. C., Marschilok, A. C., Takeuchi, K. J. & Takeuchi, E. S. Batteries used to power implantable biomedical devices. *Electrochim. Acta* **84,** 155–164 (2012).
96. Crowther, O., Meyer, B., Morgan, M. & Salomon, M. Primary Li-air cell development. *J. Power Sources* **196,** 1498–1502 (2011).
97. Reddy, T. B. Linden's handbook of batteries 4th edition. (2010).
98. Yang, S. & Knickle, H. Design and analysis of aluminum/air battery system for electric vehicles. *J. Power Sources* **112,** 162–173 (2002).
99. Herbert, D. & Ulam, J. US Patent 3,043,896 (1962). *Ger. Pat.* **1,** (1962).
100. Manthiram, A., Fu, Y., Chung, S., Zu, C. & Su, Y. Rechargeable Lithium − Sulfur Batteries. *Chem. Rev.* **114,** 11751–87 (2014).
101. Skotheim, T. A. High capacity cathodes for secondary cells. (1995).
102. Chu, M.-Y. Rechargeable positive electrodes. (1997).
103. Peramunage, D. & Licht, S. A solid sulfur cathode for aqueous batteries. *Science (80-.).* **261,** 1029–1033 (1993).
104. Mikhaylik, Y. V, Skotheim, T. A. & Trofimov, B. A. Lithium batteries. (2005).

105. Choi, Y. J. *et al.* Effects of carbon coating on the electrochemical properties of sulfur cathode for lithium/sulfur cell. *J. Power Sources* **184,** 548–552 (2008).
106. Kolosnitsyn, V. S. & Karaseva, E. V. Lithium-sulfur batteries: Problems and solutions. *Russ. J. Electrochem.* **44,** 506–509 (2008).
107. Wang, D.-W. *et al.* Carbon-sulfur composites for Li-S batteries: status and prospects. *J. Mater. Chem. A* **1,** 9382–9394 (2013).
108. Zhang, S. S., Foster, D. & Read, J. A high energy density lithium/sulfur-oxygen hybrid battery. *J. Power Sources* **195,** 3684–3688 (2010).
109. Dahl, C., Prange, A. & Steudel, R. Metabolism of natural polymeric sulfur compounds. *Biopolym. Online* (2005).
110. Diao, Y., Xie, K., Xiong, S. & Hong, X. Analysis of Polysulfide Dissolved in Electrolyte in Discharge-Charge Process of Li-S Battery. *J. Electrochem. Soc.* **159,** A421 (2012).
111. Barchasz, C., Leprêtre, J. C., Alloin, F. & Patoux, S. New insights into the limiting parameters of the Li/S rechargeable cell. *J. Power Sources* **199,** 322–330 (2012).
112. Cheon, S.-E. *et al.* Rechargeable Lithium Sulfur Battery I. *J. Electrochem. Soc.* **150,** A800 (2003).
113. Ji, X. & Nazar, L. F. Advances in Li–S Batteries. *J. Mater. Chem.* **20,** 9821 (2010).
114. Evers, S. & Nazar, L. F. Lithium À Sulfur Battery Cathodes. **46,** 1135–1143 (2013).
115. Rauh, R. D., Shuker, F. S., Marston, J. M. & Brummer, S. B. Formation of lithium polysulfides in aprotic media. *J. Inorg. Nucl. Chem.* **39,** 1761–1766 (1977).
116. Yamin, H. & Peled, E. Electrochemistry of a nonaqueous lithium/sulfur cell. *J. Power Sources* **9,** 281–287 (1983).
117. Rao, B. M. L. & Shropshire, J. A. Effect of Sulfur Impurities on Li/TiS2 Cells. *J. Electrochem. Soc.* **128,** 942–945 (1981).
118. Yang, Y. *et al.* Improving the performance of lithium-sulfur batteries by conductive polymer coating. *ACS Nano* **5,** 9187–9193 (2011).
119. Xiao, L. *et al.* A Soft Approach to Encapsulate Sulfur: Polyaniline Nanotubes for Lithium-Sulfur Batteries with Long Cycle Life. *Adv. Mater.* **24,** 1176–1181 (2012).
120. Yin, Y.-X. X., Xin, S., Guo, Y.-G. G. & Wan, L.-J. J. Lithium-Sulfur Batteries: Electrochemistry, Materials, and Prospects. *Angew. Chemie Int. Ed.* **52,** 13186–13200 (2013).
121. Herbert, D. U. J. Electric dry cells and storage battery US Pat, 3043896. (1962).
122. Azimi, N., Weng, W., Takoudis, C. & Zhang, Z. Improved performance of lithium–sulfur battery with fluorinated electrolyte. *Electrochem. commun.* **37,** 96–99 (2013).
123. Suo, L., Hu, Y.-S., Li, H., Armand, M. & Chen, L. A new class of solvent-in-salt electrolyte for high-energy rechargeable metallic lithium batteries. *Nat. Commun.* **4,** 1481 (2013).
124. Gao, J., Lowe, M. A., Kiya, Y. & Abruña, H. D. Effects of liquid electrolytes on the charge–discharge performance of rechargeable lithium/sulfur batteries: electrochemical and in-situ X-ray absorption spectroscopic studies. *J. Phys. Chem. C* **115,** 25132–25137 (2011).
125. Lin, Z., Liu, Z., Fu, W., Dudney, N. J. & Liang, C. Phosphorous pentasulfide as a novel additive for high-performance lithium-sulfur batteries. *Adv. Funct. Mater.* **23,** 1064–1069 (2013).
126. Park, J.-W., Ueno, K., Tachikawa, N., Dokko, K. & Watanabe, M. Ionic liquid electrolytes for lithium–sulfur batteries. *J. Phys. Chem. C* **117,** 20531–20541 (2013).
127. Liang, X. *et al.* Improved cycling performances of lithium sulfur batteries with LiNO 3-modified electrolyte. *J. Power Sources* **196,** 9839–9843 (2011).

128. Lin, F. *et al.* Nonflammable electrolyte for rechargeable lithium battery with sulfur based composite cathode materials. *J. Power Sources* **223,** 18–22 (2013).
129. Marmorstein, D. *et al.* Electrochemical performance of lithium/sulfur cells with three different polymer electrolytes. *J. Power Sources* **89,** 219–226 (2000).
130. Lin, Z., Liu, Z., Fu, W., Dudney, N. J. & Liang, C. Lithium Polysulfidophosphates: A Family of Lithium-Conducting Sulfur-Rich Compounds for Lithium–Sulfur Batteries. *Angew. Chemie* **125,** 7608–7611 (2013).
131. Hassoun, J. & Scrosati, B. Moving to a Solid-State Configuration: A Valid Approach to Making Lithium-Sulfur Batteries Viable for Practical Applications. *Adv. Mater.* **22,** 5198–5201 (2010).
132. Zhu, X., Wen, Z., Gu, Z. & Lin, Z. Electrochemical characterization and performance improvement of lithium/sulfur polymer batteries. *J. Power Sources* **139,** 269–273 (2005).
133. Rao, M., Geng, X., Li, X., Hu, S. & Li, W. Lithium-sulfur cell with combining carbon nanofibers–sulfur cathode and gel polymer electrolyte. *J. Power Sources* **212,** 179–185 (2012).
134. Huang, J.-Q. *et al.* Ionic shield for polysulfides towards highly-stable lithium–sulfur batteries. *Energy Environ. Sci.* **7,** 347 (2014).
135. Li, W. *et al.* V2O5 polysulfide anion barrier for long-lived Li–S batteries. *Chem. Mater.* **26,** 3403–3410 (2014).
136. Chung, S.-H. & Manthiram, A. High-performance Li–S batteries with an ultra-lightweight MWCNT-coated separator. *J. Phys. Chem. Lett.* **5,** 1978–1983 (2014).
137. Huang, C. *et al.* Manipulating surface reactions in lithium–sulphur batteries using hybrid anode structures. *Nat. Commun.* **5,** (2014).
138. Ma, G. *et al.* Hollow polyaniline sphere@ sulfur composites for prolonged cycling stability of lithium–sulfur batteries. *J. Mater. Chem. A* **2,** 10350–10354 (2014).
139. Ma, G. *et al.* A lithium anode protection guided highly-stable lithium–sulfur battery. *Chem. Commun.* **50,** 14209–14212 (2014).
140. Yang, Y., Zheng, G. & Cui, Y. Nanostructured sulfur cathodes. *Chem. Soc. Rev.* **42,** 3018–3032 (2013).
141. Yuan, L., Yuan, H., Qiu, X., Chen, L. & Zhu, W. Improvement of cycle property of sulfur-coated multi-walled carbon nanotubes composite cathode for lithium/sulfur batteries. *J. Power Sources* **189,** 1141–1146 (2009).
142. Wang, H. *et al.* Graphene-Wrapped Sulfur Particles as a Rechargeable Lithium – Sulfur Battery Cathode Material with High Capacity and Cycling Stability. *History* **11,** 1–4 (2011).
143. Cao, Y. *et al.* Sandwich-type functionalized graphene sheet-sulfur nanocomposite for rechargeable lithium batteries. *Phys. Chem. Chem. Phys.* **13,** 7660–7665 (2011).
144. Yang, J. *et al.* Novel nitrogen-doped hierarchically porous coralloid carbon materials as host matrixes for lithium-sulfur batteries. *Electrochim. Acta* **159,** 8–15 (2015).
145. Lv, W. *et al.* Peanut shell derived hard carbon as ultralong cycling anodes for lithium and sodium batteries. *Electrochim. Acta* **176,** 533–541 (2015).
146. Wang, J. *et al.* Phosphorus-doped porous carbon derived from rice husk as anode for lithium ion batteries. *RSC Adv.* **5,** 55136–55142 (2015).
147. Wu, J. *et al.* Preparation of biomass-derived hierarchically porous carbon/Co3O4 nanocomposites as anode materials for lithium-ion batteries. *J. Alloys Compd.* **656,** 745–752 (2016).
148. Long, C., Chen, X., Jiang, L., Zhi, L. & Fan, Z. Porous layer-stacking carbon derived from

in-built template in biomass for high volumetric performance supercapacitors. *Nano Energy* **12,** 141–151 (2015).
149. Lacey, M. J. *et al.* Porosity Blocking in Highly Porous Carbon Black by PVdF Binder and Its Implications for the Li-S System. *J. Phys. Chem. C* **118,** 25890–25898 (2014).
150. Wang, J., Yang, J., Xie, J. & Xu, N. A novel conductive polymer-sulfur composite cathode material for rechargeable lithium batteries. *Adv. Mater.* **14,** 963–965 (2002).
151. Wang, J. *et al.* Sulphur-polypyrrole composite positive electrode materials for rechargeable lithium batteries. *Electrochim. Acta* **51,** 4634–4638 (2006).
152. Li, W. Y. *et al.* High-performance hollow sulfur nanostructured battery cathode through a scalable, room temperature, one-step, bottom-up approach. *Proc. Natl. Acad. Sci. U. S. A.* **110,** 7148–7153 (2013).
153. Chen, H., Dong, W., Ge, J., Wang, C. & Wu, X. Ultrafine Sulfur Nanoparticles in Conducting Polymer Shell as Cathode Materials for High Performance Lithium/Sulfur Batteries. *Sci. Rep.* **3,** 1910 (2013).
154. Nguyen, D. & Yoon, H. Recent Advances in Nanostructured Conducting Polymers: from Synthesis to Practical Applications. *Polymers (Basel).* **8,** 118 (2016).
155. Lestriez, B. Functions of polymers in composite electrodes of lithium ion batteries. *Comptes Rendus Chim.* **13,** 1341–1350 (2010).
156. Fransson, L., Eriksson, T., Edström, K., Gustafsson, T., & Thomas, J. O.. Influence of carbon black and binder on Li-ion batteries. *J. Power Sources* **101,** 1–9 (2001).
157. Das, P. R., Komsiyska, L., Osters, O. & Wittstock, G. PEDOT: PSS as a Functional Binder for Cathodes in Lithium Ion Batteries. *J. Electrochem. Soc.* **162,** A674–A678 (2015).
158. Pan, J. *et al.* PAA/PEDOT:PSS as a multifunctional, water-soluble binder to improve the capacity and stability of lithium-sulfur batteries. *RSC Adv.* **6,** 40650–40655 (2016).
159. Milroy, C. & Manthiram, A. An Elastic, Conductive, Electroactive Nanocomposite Binder for Flexible Sulfur Cathodes in Lithium-Sulfur Batteries. *Adv. Mater.* (2016). doi:10.1002/adma.201601665
160. Zhao, H. *et al.* Toward practical application of functional conductive polymer binder for a high-energy lithium-ion battery design. *Nano Lett.* **14,** 6704–6710 (2014).
161. Fang, C. H. *et al.* A flexible and hydrophobic polyurethane elastomer used as binder for the activated carbon electrode in capacitive deionization. *Desalination* **399,** 34–39 (2016).
162. Cheng, P. *et al.* Biomass-Derived Carbon Fiber Aerogel as a Binder-Free Electrode for High-Rate Supercapacitors. *J. Phys. Chem. C* **120,** 2079–2086 (2016).
163. Zhai, P. Y. *et al.* Calendering of free-standing electrode for lithium-sulfur batteries with high volumetric energy density. *Carbon N. Y.* **111,** 493–501 (2017).
164. Wang, J., Yao, Z., Monroe, C. W., Yang, J. & Nuli, Y. Carbonyl-β-Cyclodextrin as a Novel Binder for Sulfur Composite Cathodes in Rechargeable Lithium Batteries. *Adv. Funct. Mater.* **23,** 1194–1201 (2013).
165. He, M., Yuan, L.-X. X., Zhang, W.-X. X., Hu, X.-L. L. & Huang, Y.-H. H. Enhanced cyclability for sulfur cathode achieved by a water-soluble binder. *J. Phys. Chem. C* **115,** 15703–15709 (2011).
166. Schneider, H. *et al.* Influence of different electrode compositions and binder materials on the performance of lithium–sulfur batteries. *J. Power Sources* **205,** 420–425 (2012).
167. Lacey, M. J., Jeschull, F., Edström, K. & Brandell, D. Functional, water-soluble binders for improved capacity and stability of lithium–sulfur batteries. *J. Power Sources* **264,** 8–14 (2014).

168. Seh, Z. W. *et al.* SD Stable cycling of lithium sulfide cathodes through strong affinity with a bifunctional binder. *Chem. Sci.* **4,** 3673 (2013).
169. Zhou, W., Yu, Y., Chen, H., DiSalvo, F. J. & Abruña, H. D. Yolk–shell structure of polyaniline-coated sulfur for lithium–sulfur batteries. *J. Am. Chem. Soc.* **135,** 16736–16743 (2013).
170. Seh, Z. W. *et al.* Sulphur–TiO2 yolk–shell nanoarchitecture with internal void space for long-cycle lithium–sulphur batteries. *Nat. Commun.* **4,** 1331 (2013).
171. Bucur, C. B. *et al.* Ultrathin tunable ion conducting nanomembranes for encapsulation of sulfur cathodes. *Energy Environ. Sci.* **6,** 3286–3290 (2013).
172. Chen, H., Bi, X. Y., Zhang, L. J. & Shen, Y. Temperature-Graded Ferroelectric Thin Films under Two Boundary Conditions. in *Advanced Materials Research* **750,** 1910–1913 (Trans Tech Publ, 2013).
173. Tang, Q. *et al.* Nafion coated sulfur–carbon electrode for high performance lithium–sulfur batteries. *J. Power Sources* **246,** 253–259 (2014).
174. Zhou, X. *et al.* Improving the performance of lithium–sulfur batteries by graphene coating. *J. Power Sources* **243,** 993–1000 (2013).
175. Evers, S., Yim, T. & Nazar, L. F. Understanding the nature of absorption/adsorption in nanoporous polysulfide sorbents for the Li–S battery. *J. Phys. Chem. C* **116,** 19653–19658 (2012).
176. Pang, Q., Kundu, D., Cuisinier, M. & Nazar, L. F. Surface-enhanced redox chemistry of polysulphides on a metallic and polar host for lithium-sulphur batteries. *Nat. Commun.* **5,** (2014).
177. Tao, X. *et al.* Strong Sulfur Binding with Conducting Magnéli-Phase Ti n O2 n–1 Nanomaterials for Improving Lithium–Sulfur Batteries. *Nano Lett.* **14,** 5288–5294 (2014).
178. Zhou, J. *et al.* Rational design of a metal–organic framework host for sulfur storage in fast, long-cycle Li–S batteries. *Energy Environ. Sci.* **7,** 2715–2724 (2014).
179. Zheng, J. *et al.* Lewis acid–base interactions between polysulfides and metal organic framework in lithium sulfur batteries. *Nano Lett.* **14,** 2345–2352 (2014).
180. Yao, H. *et al.* Improving lithium–sulphur batteries through spatial control of sulphur species deposition on a hybrid electrode surface. *Nat. Commun.* **5,** (2014).
181. Zheng, J. *et al.* Controlled nucleation and growth process of Li2S2/Li2S in lithium-sulfur batteries. *J. Electrochem. Soc.* **160,** A1992–A1996 (2013).
182. Su, Y.-S., Fu, Y., Cochell, T. & Manthiram, A. A strategic approach to recharging lithium-sulphur batteries for long cycle life. *Nat. Commun.* **4,** (2013).
183. Yang, Y., Zheng, G. & Cui, Y. A membrane-free lithium/polysulfide semi-liquid battery for large-scale energy storage. *Energy Environ. Sci.* **6,** 1552–1558 (2013).
184. Shi, Y., Wan, Y. & Zhao, D. Ordered mesoporous non-oxide materials. *Chem. Soc. Rev.* **40,** 3854 (2011).
185. Li, W., Yue, Q., Deng, Y. & Zhao, D. Ordered mesoporous materials based on interfacial assembly and engineering. *Adv. Mater.* **25,** 5129–5152 (2013).
186. Evers, S. & Nazar, L. F. New approaches for high energy density lithium-sulfur battery cathodes. *Acc. Chem. Res.* **46,** 1135–1143 (2013).
187. Raccichini, R., Varzi, A., Passerini, S. & Scrosati, B. The role of graphene for electrochemical energy storage. *Nat. Mater.* **14,** 271–9 (2015).
188. Zhang, B., Qin, X., Li, G. R. & Gao, X. P. Enhancement of long stability of sulfur cathode by encapsulating sulfur into micropores of carbon spheres. *Energy Environ. Sci.* **3,** 1531

(2010).
189. Liang, C., Dudney, N. J. & Howe, J. Y. Hierarchically structured sulfur/carbon nanocomposite material for high-energy lithium battery. *Chem. Mater.* **21,** 4724–4730 (2009).
190. Li, X. *et al.* Optimization of mesoporous carbon structures for lithium-sulfur battery applications. *J. Mater. Chem.* **21,** 16603–16610 (2011).
191. He, G., Mandlmeier, B., Schuster, J., Nazar, L. F. & Bein, T. Bimodal Mesoporous Carbon Nano fi bers with High Porosity: Freestanding and Embedded in Membranes for Lithium − Sulfur Batteries. *Chem. Mater.* **26,** 3879–3886 (2014).
192. Tao, X. *et al.* Highly mesoporous carbon foams synthesized by a facile, cost-effective and template-free Pechini method for advanced lithium-sulfur batteries. *J. Mater. Chem. A* **1,** 3295–3301 (2013).
193. Li, D. *et al.* High Sulfur Loading Cathodes Fabricated Using Peapodlike , Large Pore Volume Mesoporous Carbon for Lithium − Sulfur Battery. **M,** (2013).
194. Shinkarev, V. V., Fenelonov, V. B. & Kuvshinov, G. G. Sulfur distribution on the surface of mesoporous nanofibrous carbon. *Carbon N. Y.* **41,** 295–302 (2003).
195. Steijns, M. & Mars, P. The adsorption of sulfur by microporous materials. *J. Colloid Interface Sci.* **57,** 175–180 (1976).
196. Li, Z., Huang, Y., Yuan, L., Hao, Z. & Huang, Y. Status and prospects in sulfur-carbon composites as cathode materials for rechargeable lithium-sulfur batteries. *Carbon N. Y.* **92,** 41–63 (2015).
197. Wang, D.-W. *et al.* A microporous–mesoporous carbon with graphitic structure for a high-rate stable sulfur cathode in carbonate solvent-based Li–S batteries. *Phys. Chem. Chem. Phys. Phys. Chem. Chem. Phys* **14,** 8703–8710 (2012).
198. Xin, S. *et al.* Smaller Sulfur Molecules Promise Better Lithium − Sulfur Batteries. *J. Am. Chem. Soc.* **134,** 2–5 (2012).
199. Shao, C. *et al.* Deformation-induced linear chain-ring transition and crystallization of living polymer sulfur. *Macromolecules* **40,** 9475–9481 (2007).
200. Wang, D.-W. *et al.* Carbon–sulfur composites for Li–S batteries: status and prospects. *J. Mater. Chem. A* **1,** 9382 (2013).
201. Ding, B. *et al.* Encapsulating sulfur into hierarchically ordered porous carbon as a high-performance cathode for lithium-sulfur batteries. *Chem. - A Eur. J.* **19,** 1013–1019 (2013).
202. Liu, M., Ye, F., Li, W., Li, H. & Zhang, Y. Chemical routes toward long-lasting lithium/sulfur cells. *Nano Res.* **9,** 94–116 (2016).
203. Niu, S. *et al.* N and S co-doped porous carbon spheres prepared using l-cysteine as a dual functional agent for high-performance lithium–sulfur batteries. *Chem. Commun.* **51,** 17720–17723 (2015).
204. Yan, J., Liu, X., Wang, X. & Li, B. Long-life, high-efficiency lithium/sulfur batteries from sulfurized carbon nanotube cathodes. *J. Mater. Chem. A* **3,** 10127–10133 (2015).
205. Ji, L. *et al.* Graphene Oxide as a Sulfur Immobilizer in High Performance Lithium/Surfur cells. *J. Am. Chem. Soc.* **133,** 18522–18525 (2011).
206. Yang, C. *et al.* Insight into the E ff ect of Boron Doping on Sulfur / Carbon Cathode in Lithium − Sulfur Batteries. (2014).
207. Wang, C. *et al.* Sulfur–amine chemistry-based synthesis of multi-walled carbon nanotube–sulfur composites for high performance Li–S batteries. *Chem. Commun.* **50,** 1202–1204 (2014).

208. Yang, J. *et al.* Functionalized n-doped porous carbon nanofiber webs for a lithium-sulfur battery with high capacity and rate performance. *J. Phys. Chem. C* **118,** 1800–1807 (2014).
209. Pang, Q. *et al.* A Nitrogen and Sulfur Dual-Doped Carbon Derived from Polyrhodanine@Cellulose for Advanced Lithium-Sulfur Batteries. *Adv. Mater.* **27,** 6021–6028 (2015).
210. Xu, G. *et al.* Biomass-derived porous carbon materials with sulfur and nitrogen dual-doping for energy storage. *Green Chem.* **17,** 1668–1674 (2015).
211. Lee, J. S. & Manthiram, A. Hydroxylated N-doped carbon nanotube-sulfur composites as cathodes for high-performance lithium-sulfur batteries. *J. Power Sources* **343,** 54–59 (2017).
212. Song, J. *et al.* Nitrogen-Doped Mesoporous Carbon Promoted Chemical Adsorption of Sulfur and Fabrication of High-Areal-Capacity Sulfur Cathode with Exceptional Cycling Stability for Lithium-Sulfur Batteries. *Adv. Funct. Mater.* **24,** 1243–1250 (2014).
213. Zhou, L., Lin, X., Huang, T. & Yu, A. Nitrogen-doped porous carbon nanofiber webs/sulfur composites as cathode materials for lithium-sulfur batteries. *Electrochim. Acta* **116,** 210–216 (2014).
214. Song, J. *et al.* Strong lithium polysulfide chemisorption on electroactive sites of nitrogen-doped carbon composites for high-performance lithium-sulfur battery cathodes. *Angew. Chemie - Int. Ed.* **54,** 4325–4329 (2015).
215. Zhou, W. *et al.* Tailoring Pore Size of Nitrogen-Doped Hollow Carbon Nanospheres for Confining Sulfur in Lithium-Sulfur Batteries. *Adv. Energy Mater.* **5,** 1–8 (2015).
216. Sun, X. G., Wang, X., Mayes, R. T. & Dai, S. Lithium-sulfur batteries based on nitrogen-doped carbon and an ionic-liquid electrolyte. *ChemSusChem* **5,** 2079–2085 (2012).
217. Sun, F. *et al.* High Efficiency Immobilization of Sulfur on Nitrogen-Enriched Mesoporous Carbons for Li−S Batteries. *ACS Appl. Mater. Interfaces* **5,** 5630–8 (2013).
218. Qiu, Y. *et al.* High-Rate, Ultralong Cycle-Life Lithium/Sulfur Batteries Enabled by Nitrogen-Doped Graphene. 1–7 (2014).
219. Seh, Z. W. *et al.* Facile synthesis of Li2S–polypyrrole composite structures for high-performance Li2S cathodes. *Energy Environ. Sci.* **7,** 672 (2014).
220. Guo, J., Yang, Z., Yu, Y. & Archer, L. A. Lithium − Sulfur Battery Cathode Enabled by Lithium − Nitrile Interaction. *J. Am. Chem. Soc.* **135,** 763–767 (2013).
221. Rybarczyk, M. K. *et al.* Porous carbon derived from rice husks as sustainable bioresources: insights into the role of micro-/mesoporous hierarchy in hosting active species for lithium–sulphur batteries. *Green Chem.* **18,** 5169–5179 (2016).
222. Ou, J. *et al.* Nitrogen-rich porous carbon derived from biomass as a high performance anode material for lithium ion batteries. *J. Mater. Chem. A* **3,** 6534–6541 (2015).
223. Chen, L. *et al.* Hierarchically porous nitrogen-rich carbon derived from wheat straw as an ultra-high-rate anode for lithium ion batteries. *J. Mater. Chem. A* **2,** 9684–9690 (2014).
224. Li, J. *et al.* Mesoporous carbon from biomass: one-pot synthesis and application for Li–S batteries. *J. Mater. Chem. A* **2,** 13916 (2014).
225. Zhu, Y. *et al.* Hierarchical porous carbon derived from soybean hulls as a cathode matrix for lithium-sulfur batteries. *J. Alloys Compd.* **695,** 1–7 (2016).
226. Yang, K. *et al.* Biomass-Derived Porous Carbon with Micropores and Small Mesopores for High-Performance Lithium-Sulfur Batteries. *Chem. - A Eur. J.* **100191,** 3239–3244 (2016).
227. Li, Y. *et al.* Hierarchical Porous Carbon Materials Derived from Self-Template Bamboo Leaves for Lithium–Sulfur Batteries. *Electrochim. Acta* **229,** 352–360 (2017).

CHAPTER 3: EXPERIMENTAL AND CHARACTERIZATION METHODS

This chapter consists of the methodology that is followed to perform the experimental work and the characterization. Herein, preparation and activation methods of biochar are described followed by the preparation of sulfur-activated biochar composite and lithium-sulfur coin cell. Later, physical and chemical characterization (such as moisture content analysis, ash content measurement, elemental analysis, scanning electron microscopy, surface area, and porosity analysis, thermogravimetric analysis, RAMAN and FTIR spectroscopy) and electrochemical characterization (galvanostatic charge-discharge measurement and cyclic voltammetry) are discussed.

3.1 EXPERIMENTAL SECTION

This section includes two biochar preparation methods (such as slow pyrolysis and fast pyrolysis) followed by two biochar activation methods (KOH and $ZnCl_2$ activation). Then, the synthesis process to obtain sulfur-activated biochar composite followed by assembly process of 2032 Li-S coin cell is described. Table 3.1 shows the sample name and brief description of the samples that were prepared or used for this thesis work.

Table 3.1: Sample name and a brief description of the samples.

Sample Name	Description
C-BM	Canola meal biomass
D-BM	Douglas-fir wood biomass
CF-BC	Fast pyrolysis biochar derived from C-BM at 500°C
CS-BC	Slow pyrolysis biochar derived from C-BM at 500°C
DF-BC	Fast pyrolysis biochar derived from D-BM at 500°C
DS-BC	Slow pyrolysis biochar derived from D-BM at 500°C
CF-AB	Activated biochar from CF-BC using KOH at 800°C
CS-AB	Activated biochar from CS-BC using KOH at 800°C
CF-ABZ	Activated biochar from CF-BC using $ZnCl_2$ at 600°C
DF-AB	Activated biochar from DF-BC using KOH at 800°C
DS-AB	Activated biochar from DS-BC using KOH at 800°C
CB	Commercial conductive carbon black, Super-P
CF-AB -S	Composite of CF-AB and sulfur
CF-AB -S-T	CF-AB-S after washed by toluene
CS-AB-S	Composite of CS-AB and sulfur
DF-AB-S	Composite of DF-AB and sulfur
CB-S	Composite of CB and sulfur

3.1.1 Biochar Preparation

Two types of biomass (canola meal and Douglas-fir wood chips) were used as the precursor of biochar in this project. Biochar samples from two biomass sources were prepared through fast pyrolysis and slow pyrolysis. Douglas-fir biomass (0.8 mm crumbles from chips) was obtained from Forest Concepts, LLC. (Auburn, Washington). Canola meal was purchased from Ranch-Way Feeds (Fort Collins, Colorado). Both the biomass samples were stored in cold storage at 4˚C temperature, and dried overnight at 50˚C before pyrolysis to obtain moisture content less than 10% by weight. In Figure 3.1, digital images of canola meal (left) and Douglas-fir (right) are shown.

Figure 3.1: Canola meal (left) and Douglas-fir wood chips (right) biomass

(i) Slow Pyrolysis Method

The slow pyrolysis of biochar was performed in a fixed bed reactor. At first, biomass sample was placed in a stainless steel tube reactor, and the tubular reactor was placed inside a furnace which was heated at 500°C with a heating rate of 5°C/min and hold for 2 hours. The purging of industrial grade nitrogen gas (Airgas) from the bottom of the reactor at 0.2 LPM (liter per minute) was started at least 30 min before starting of heating. Nitrogen purging was continued

until the tube reached at room temperature after the pyrolysis was completed. The reactor setup is shown in Figure 3.2.

Once the tube reached room temperature, biochar samples were collected from the tube, and bio-oil with aqueous phase was collected from the condenser. Biochar and bio-oil samples were stored at 4˚C and -20˚C, respectively for further analysis. A similar procedure was followed to prepare other batches of biochar.

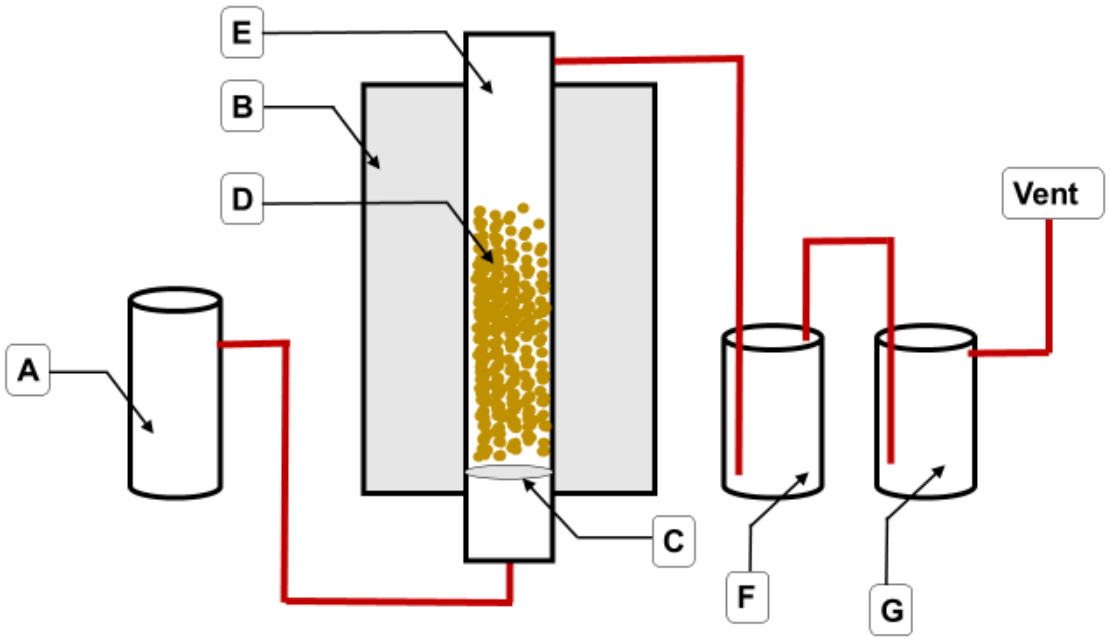

Figure 3.2: Fixed bed reactor setup for slow pyrolysis process

(A: nitrogen tank, B: furnace, C: stainless-steel 316 mesh, D: biomass, E: stainless-steel 316 tube, F: condenser to collect liquids, G: water at room temperature to confirm flowing and capture water soluble gases, Red line: tube connector)

(ii) Fast Pyrolysis Method

The advantages of fluidized-bed design are the high heating rates and short vapor residence times, which are essential to produce a high liquid yield. Therefore, a bubbling fluidized-bed was selected for fast pyrolysis reactor in this study. Fast pyrolysis experiments were carried out using a bench scale bubbling fluidized bed reactor shown in Figure 3.3, which was used in previous pyrolysis and gasification studies [1–4]. The set-up is consisted of a biomass hopper equipped with a twin screw auger, an injection screw, a bubbling fluidized bed reactor, a high-temperature filter (HTF) maintained at 350°C, two condensers in series cooled by a mixture of ethylene glycol and water maintained below 3°C by a circulating chiller, an electrostatic precipitator (ESP) with a 20 kV supply to the rod and a bio-oil collector attached to the bottom of ESP. The fluidized bed reactor was consisted of the main reactor with 50 mm (2 in.) diameter and 0.58 m (22.75 in.) length and the freeboard with 100 mm (4 in.) diameter and 0.20 m (8 in.) length. The total height of the reactor is 0.78 m (30.75 in). The biomass was stored in the hopper and fed into the reactor with the help of the auger feeder.

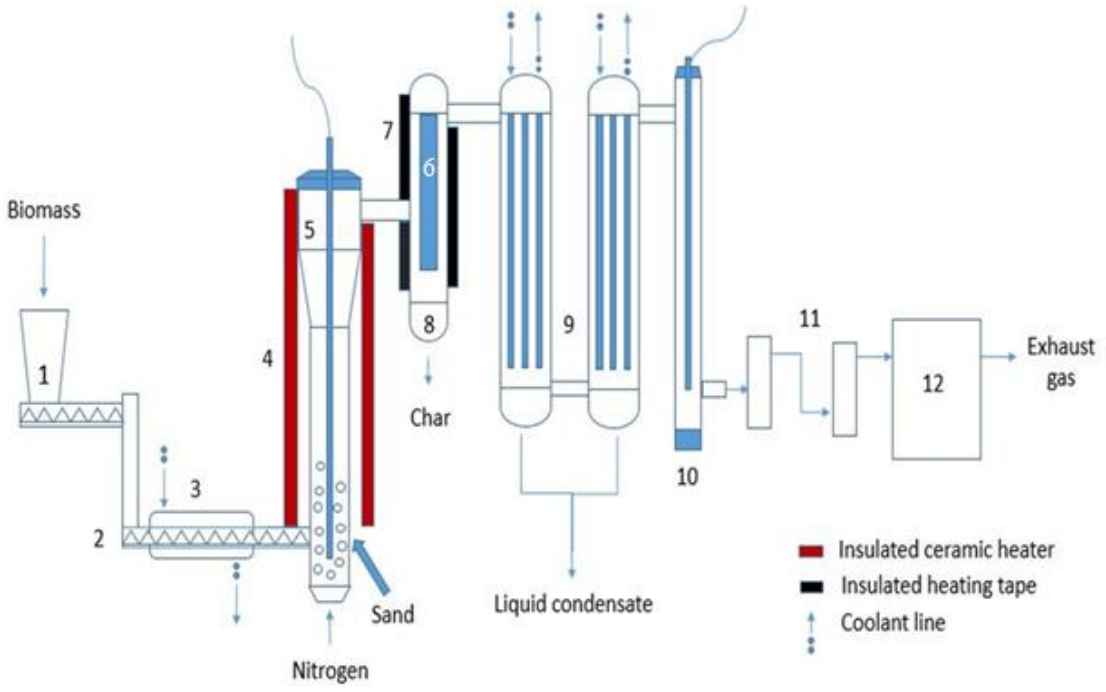

Figure 3.3: Schematic of bench-scale fluidized bed reactor setup for fast pyrolysis process[2].

(1-biomass hopper, 2-injection screw; 3-heat exchanger, 4-reactor heaters, 5-fluidized bed reactor tube, 6-high temperature filter, 7-high temperature filter heaters, 8-char collector, 9-condensers, 10-electrostatic precipitator, 11-moisture absorber and 12-gas analyzer)

In the experiments, washed and dried sand (7062-06, Macron Fine Chemicals) was used as bed materials. At first, 1000 g of bed materials were placed in the reactor. The heater was turned on to heat up the sand bed at around 500°C, and the air was blown at 12 LPM for the fluidization of bed material by fluidization. Chiller temperature was set below 3˚C. As soon as the sand temperature was around target temperature on both the bottom and middle part of the reactor, nitrogen flow at 12 LPM was introduced to achieve an inert environment for pyrolysis. A NOVA gas analyzer was used to ensure oxygen-limited environment. Once O_2 levels reached $\leq 0.1\%$, the auger feeder was started at a feed rate of 7.7 g/min for canola meal and 1.5 g/min for Douglas-fir. The O_2, H_2, CH_4, CO and CO_2 content were frequently checked to ensure successful pyrolysis and leakage/oxygen free environment. Once all the biomass was tranferred to the reactor, the feeder

was turned off. Still, the reactor heater (at 500˚C) was kept for 10 mins to ensure conversion of the biomass of reactor tube. After 30 mins, the entire systems including ESP, HTF heater and chiller were turned off, and nitrogen purging was stopped. Then, bio-oil was collected and stored at -20°C freezer. Biochar was collected once the system reached to room temperature. Two types of char were collected; sand mixed char from the reactor tube and clean char from HTF filter. In the current work, HTF filter char were used as fast pyrolysis char.

3.1.2 Activation of Biochar

Among physical and chemical activation methods, the latter method is selected in this thesis work. Activation methods of biochar using two chemical agents such as KOH and $ZnCl_2$ are discussed in this section.

(i) KOH Activation

For biochar activation using KOH as a chemical activation agent, 105˚C oven-dried biochar and KOH were mixed at 1:3 weight ratio. At first, KOH solution was prepared using KOH pellets (Sigma-Aldrich, Regent Grade) and distilled water (3 ml water for each 1g KOH) in a glass flask and kept on magnetic stirring for 30 mins. Later, 15 g biochar was mixed gradually to 45 g KOH solution and kept on magnetic stirring for another 2 hours at room temperature. The mixture was dried in PTFE crucible overnight at 105˚C. For the ease of operation and homogeneity, the mixture was not completely dried as fully dried mixture would have KOH on the top and would require further grinding. Then, the mixture was placed on the stainless tube identical to the one used for slow pyrolysis and heated up in a nitrogen environment. At first, nitrogen gas were purged for 30 min at 0.3 LPM before heating but reduced to 0.05 LPM once the temperature is 375˚C. The

temperature was kept at 375˚C for 1 hour to avoid carbon loss by a direct attack from the steam[5,6]. Then the mixture was heated up to 800˚C at hold at this temperature for 2 hours. Throughout the process, the heating rate was kept at 5˚C. Nitrogen gas was purged at 0.05 LPM until the reactor reached room temperature which usually took overnight. The reactor setup for biochar activation is shown in Figure 3.4.

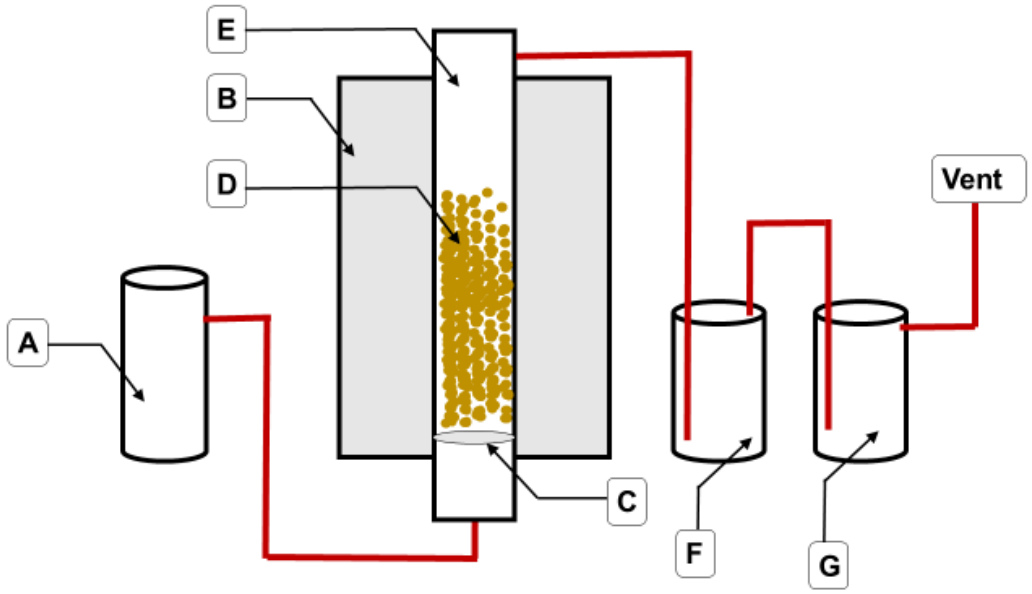

Figure 3.4: Fixed bed reactor for biochar activation

(A: nitrogen tank, B: furnace, C: stainless-steel 316 mesh, D: biomass and activation agent mixture, E: stainless-steel 316 tube, F: condenser to collect liquids, G: water at room temperature to confirm flowing and capture water soluble gases, Red line: tube connector)

The heat-treated mixture was washed with 500 ml HCl of 0.75 M followed by distilled water using vacuum filtration (VWR® glass fiber filters) to remove residual KOH. Washing with distilled water was continued until the pH became same as the pH of distilled water. After drying this sample at 105˚C overnight, activated carbon or activated biochar was obtained, which was stored in glass vials at room temperature.

(ii) $ZnCl_2$ Activation

For activation using $ZnCl_2$ as a chemical activation agent, biochar and $ZnCl_2$ were mixed at 1:3 for HTF biochar by weight. At first, the 15 g $ZnCl_2$ powder was added to 45 ml distilled water in a glass flask and kept on magnetic stirring for 15 mins to prepare $ZnCl_2$ solution. Later, biochar or biomass samples were mixed gradually to the $ZnCl_2$ solution and kept on magnetic stirring for another 4 hours at room temperature. The mixture was dried overnight at 105˚C. For ease of operation and homogeneity, the mixture was not completely dried as fully dried mixture would have $ZnCl_2$ on the top and would require further grinding.

Then, the mixture was placed in a stainless steel tube and heated under a nitrogen environment. At first, nitrogen gas was purged for 15 min at 0.5 LPM before heating. Then the mixture was heated up to 600˚C and hold at this temperature for 2 hours. Throughout the process, the heating rate was kept at 5˚C/min. Nitrogen gas was purged at 0.5 LPM until the reactor reached room temperature, which usually took overnight. Later, the mixture was added to 1000 ml HCl of 0.1 M and kept for 1 h in magnetic stirring for conversion of activation by-product water-insoluble ZnO to convert into water-soluble $ZnCl_2$ (Eq.15).

$$ZnO + 2HCl \rightarrow ZnCl_2 + H_2O \qquad \text{(Eq 15)}$$

The mixture then was washed with distilled water and dried following the identical method as KOH activation.

3.1.3 Synthesis of Sulfur-Carbon (S/C) Composites

Different amounts of sublimed sulfur (sulfur powder, sublimed, -100 mesh, 99.5%, Alfa Aesar) were mixed with the carbon (such as activated biochar or carbon black) samples for 15 h using ball milling at 350 RPM to produce a dark mixture. Carbon black was purchased from Alfa

Aesar (Carbon black, Super P® Conductive, 99+ %). All the carbon samples were dried at 105˚C before ball milling and weighing. These mixtures were then sealed into a 15 ml size borosilicate glass tube (Pressure Tubes with Ace-Thred and Front Seal Plugs, Ace Glass) with argon gas and heated at 155°C for 24 hours in an oven at 5˚C/min heating rate. Glass tube was wrapped with aluminum foil for an uniform heat transfer. The melted sulfur has the lowest viscosity at 155°C, which facilitates the sulfur molecules to enter the nanopores of carbon by capillary action[7]. Also at the lowest viscosity, a substantial ring scission of cyclo-S_8 could take place. Therefore, chain-like sulfur molecules could migrate into the carbon micropores. Once the sulfur molecules diffuse into the carbon micropores, they could not go back to S_8 rings due to the spatial confinement of carbon micropores, but maintain as small $S_{2\text{-}4}$ molecules[8]. After heating, there will be no bulk sulfur in the mixture. Therefore, chain-like sulfur molecules could migrate into the carbon after cooling to room temperature. The biochar-sulfur composites with different sulfur contents were obtained using this procedure. The weight ratio of sulfur/carbon were adjusted to accommodate the volume expansion of the pore content on full lithiation to Li_2S. (Detailed calculation is provided in Appendix A)

(i) Removing excess sulfur from the surface of S/C composite

In ambient conditions sulfur is soluble into a few substances, such as carbon disulfide CS_2 (35% solubility at RT), benzene (1.2% at RT) and toluene (2% at RT). Although CS_2 can dissolve sulfur easily, it was avoided due to its extremely toxic nature and low evaporation temperature. Thus, toluene was chosen in this thesis work to wash off the excess sulfur from the surface of S/C composite. At room temperature, 1 g S/C composite was added to 15 g toluene in a glass vial and magnetically stirred for 15 minutes. Later, the toluene with dissolved sulfur was removed by

centrifugation. Washed S/C composite was vacuum dried at 112°C to remove remained toluene fully. CF-AB-S S/C composite was washed in this thesis work and named CF-AB-S-T after toluene wash.

3.2 CHARACTERIZATION

This section includes the methods utilized for physical, chemical and electrochemical characterization of the samples. Characterization methods are divided into three sections such as (a) physical characterization (b) chemical characterization and (c) electrochemical characterization.

3.2.1 Physical Characterization

Physical characterization methods such as moisture content analysis, ash content analysis and sulfur loading using thermogravimetric analysis (TGA), scanning electron microscope (SEM), and surface area and porosity analysis were utilized to analyze the physical properties of the samples. A brief introduction of the physical characterization methods and characterization conditions are discussed below.

(i) Moisture Content Analysis

Moisture content (MC) analysis is essential to ensure the required dryness of the biomass feedstock before pyrolysis. It is also important in the calculation of carbon or nitrogen weight percentage. The moisture content in percentage is determined followed by the Eq. 16:

$$\text{MC}\ (\%) = \frac{\text{weight of sample before drying} - \text{weight of sample after drying}}{\text{weight of sample before drying}} \times 100\% \quad \text{(Eq. 16)}$$

Moisture content analysis was performed using Mettler Toledo moisture analyzer (Model: MJ33). About 1 g sample was placed in an aluminum pan that is placed inside the instrument. Samples were heated up to 105°C to obtain the moisture content percentage following Eqn. 3.1.

(ii) Thermogravimetric Analysis (TGA)

In TGA, the mass of a sample specimen is monitored as a function of temperature or time as the substance is subjected to a controlled temperature program in a controlled atmosphere[9]. TGA includes a sample pan that is supported by a precision balance and resides in a furnace. The sample environment is being controlled by purging inert or a reactive gas that flows over the sample and exits through an exhaust.

TGA is used in the current study to determine the ash content of activated biochar, carbon black, biochar and biomass. The following heating condition mentioned at Table 3.2 was followed in 20 ml/min air flow rate using dried alumina pan for ash content measurement. About 10-15 mg of each sample was taken into an alumina pan and dried at 105˚C for 30 min at first in air environment while flowing air at 20 ml/min. Once the sample was dried, it was heated up and hold for 90 min at 750˚C.

Table 3.2: TGA temperature profile for ash content measurement.

Step	Target temperature (˚C)	Heating rate (˚C/min)	Hold time (min)
First	105	10	30
Second	750	10	60

TGA and CHNS elemental analyzer were used to determine the exact sulfur content in the porous carbon-sulfur composite. At the around 444°C, a sharp decline of mass can be observed due to vaporization of sulfur. At nitrogen or argon environment, all the sulfur would vaporize leaving behind porous carbon when the temperature is near 444°C. The change of mass measured by TGA would determine the percentage of sulfur in a sulfur-porous carbon composite, which is essential to estimate the specific capacity of a Li-S battery. In this research work, TGA analysis was performed using nitrogen environment and alumina sample pan. Temperature program used for TGA to determine the S content is shown in Table 3.3.

Table 3.3: TGA temperature profile for sulfur content measurement.

Step	Target temperature ˚C	Heating rate ˚C/min	Hold time min
First	105	10	30
Second	600	10	10

(iii) Surface Area and Porosity Analysis

Physical properties such as the specific surface area (area per unit mass), the specific pore volume (pore volume per unit mass), and the pore size distribution play a significant role in many processing applications including the electrochemical behavior of Li-S batteries and the overall performance of activated carbon and biochar. Specific surface area is a material property of solids which measures the total surface area per unit of mass with units of m^2/g. It is a standard practice to derive surface area from physisorption isotherm data by applying Brunauer-Emmett-Teller (BET) method at P/P_0 less than or equal to 0.3 [10].

Pore size (generally, pore width) is the distance between two opposite walls of the pore (diameter of cylindrical pores, the width of slit-shaped pores).[11] Pore size distribution is expressed by the derivatives dA_p/dr_p or dV_p/dr_p as a function of r_p, where A_p, V_p, and r_p are the wall area, volume, and radius of the pores, respectively. Biochar and activated biochar typically has slit-shaped pores and, thus, r_p should be replaced by the width.[11]

These physical properties were determined from N_2 adsorption-desorption isotherms at 77 K using a gas sorption analyzer (Quantachrome Autosorb iq). Before each analysis, activated biochars were outgassed following pressure controlled (limit: 0.075 torrs) heating (conditions mentioned in Table 3.4) in a vacuum state.

Table 3.4: Outgassing profile for activated biochars

Temperature (°C)	Heating rate (°C/min)	Soak time (hours)
80	2	0.5
120	2	0.5
300	2	13

The specific surface area was measured using a Brunauer-Emmet-Teller (BET) method at P/P_0 = 0.05 to 0.3 at correlation coefficient value, r ≥0.997. Total pore volume was obtained at P/P_0 = 0.995

(iv) Scanning Electron Microscopy (SEM)

Scanning Electron Microscope (SEM) scans a sample specimen with a focused beam of high-energy electrons and delivers images with the topographical and compositional information of the sample. The electron beam is produced at the top of the microscope by an electron gun. The beam follows a vertical path and travels through electromagnetic fields and focusing lenses, which

focus the beam down toward the sample. X-rays and electrons are ejected from the sample once the beam hits the sample. Detectors collect these X-rays, backscattered electrons, and secondary electrons and convert them into a signal that is sent to the computer which generates a real-time image displaying the morphology of the sample.

In this thesis work, a Zeiss EVO 50 Variable Pressure Scanning Electron Microscope (Auburn University Research Instrumentation Facility) is used to obtain microscopic images for morphological characterization of samples. The samples were coated with gold for achieving higher resolution.

3.2.2 Chemical Characterization

For analyzing the chemical properties of the samples, chemical characterization methods such as elemental analysis or CHNS analysis, FTIR spectroscopy and Raman spectroscopy were performed. A brief introduction of the chemical characterization methods along with the characterization conditions is described below.

(i) Elemental Analysis

Elemental analysis was performed to obtain a quantitive measurement of carbon, nitrogen, hydrogen and sulfur content of samples. Elementar vario MICRO cube CHNS analyzer was used to perform the elemental analysis.

(ii) Fourier transform infrared spectroscopy (FTIR)

FTIR is the preferred method of infrared spectroscopy that offers qualitative analysis of organic and inorganic samples. It is an effective analytical instrument for detecting functional

groups and characterizing covalent bonding information. FTIR identifies chemical bonds in a molecule by producing an infrared absorption spectrum. When IR radiation is passed through a sample, some radiation is absorbed by the sample and some passes through (i.e. transmitted). The resulting signal at the detector is a spectrum representing a molecular 'fingerprint' of the sample. The usefulness of infrared spectroscopy arises because different chemical structures (molecules) produce different spectral fingerprints. The Fourier Transform converts the detector output to an interpretable spectrum and generates spectra with patterns that provide structural insights. For Fourier transform infrared spectroscopy (FTIR, Thermo Scientific), the samples were mixed with KBr and ground on agate mortar. The samples then were directly put into the IR chamber and examined in the range of 4000–1000 cm^{-1} at a resolution of 4 cm^{-1}.

(iii) Raman Spectroscopy

Raman spectroscopy is the most sensitive to highly symmetric covalent bonds with little or no natural dipole moment. The carbon-carbon bonds that make up these materials fit this criterion perfectly. Thus, Raman spectroscopy is highly sensitive to these materials and able to provide a wealth of information about their structure. Raman spectroscopy is capable of discerning even slight changes in structure making it a valuable tool for the characterization of carbon nanomaterials[12]. Measurements of Raman spectra were performed on a Renishaw InVia Raman Spectrometer under a backscattering geometry (λ= 532 nm).

3.2.3 Electrochemical Characterization

Electrochemical Characterizations such as galvanostatic charge-discharge measurements and cyclic voltammetry were performed to evaluate electrochemical performance of the as

prepared Li-S cell. In this section, coin cell assembly process and electrochemical characterization methods are described below.

(i) Assembling of Li-S coin cell

The components of Li-S 2032-coin cell are shown in Figure 3.5. Negative cap, spring, spacers and positive cap were purchased from MTI Corporation, the USA for 2032-coin cell systems. Lithium anode (Lithium Chip, 15.6 mm diameter and 0.25 mm thickness) and Li-ion Battery Separator Film (25 μm thick x 85 mm W x 60 m L, Celgard) were obtained from MTI Corporation, USA. Lithium anode and separator films were punched to 11 mm and 20 mm diameter disk respectively.

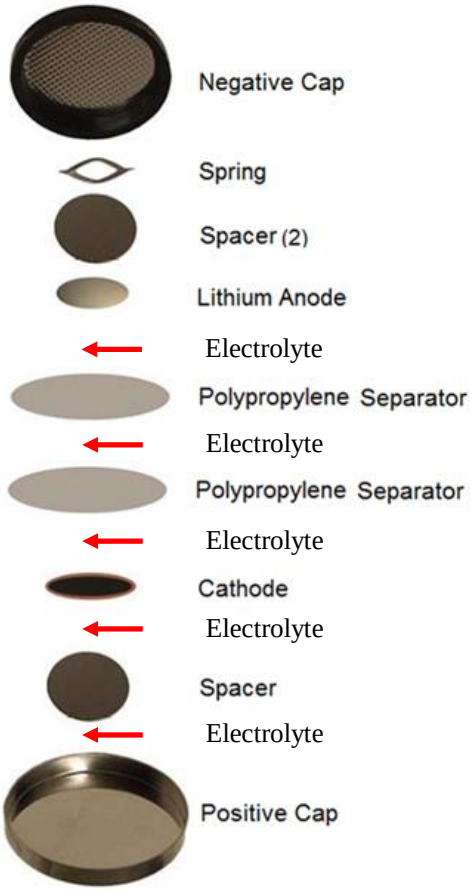

Figure 3.5: Li-S coin cell assembly (2032-coin cell)

Cathode electrode and electrolyte were prepared in the labs of Auburn University. The first step of cathode electrode preparation was for the preparation of cathode slurry. The slurry and electrode preparation method has a significant influence on the electrochemical performance of lithium based batteries[13–16]. Initially, the electrode slurry was prepared by mixing 70% as-synthesized S/C composites with 20% Super-P conductive carbon black and 10% polyvinylidene fluoride (PVDF) binder in N-methyl-2-pyrrolidinone (NMP). At first binder solution were prepared with 5% polyvinylidene fluoride (PVDF) in NMP solution (5 g PVDF for 95 g NMP) using 30 min ultrasonicator followed by overnight magnetic stirring for homogeneous dispersion and stored in a dark glass bottle. Before making binder solution, PVDF was dried at 120°C for 12 hours. Before preparation of the slurry, the conductive carbon black (Super-P) was dried at 120°C overnight. Then 70% S/C composite and 20% carbon black were mixed in an agate mortar for 30 mins. The materials were added partially rather than all at a time to obtain better homogeneity. Later this mixture was taken at a glass vial and kept for magnetic stirring for at least 12 h at room temperature. The casting of the electrode was performed following the doctor blade coating (DBC) technique which is widely used in the textile, paper, photographic film, printing, and ceramic industries to create highly uniform flat films over large areas. In DBC technique, an immobilized blade applies a unidirectional shear force to a slurry, which passes through a small gap between the blade and the substrate[17]. For casting the electrode, a flat plate of stainless steel with a smooth surface was placed on the table. The plate surface was cleaned using alcohol solution and kimwipes. Before spreading the thing aluminium foil on the plate, a trace amount of NMP solvent was spread on the plate to hold the Al foil to the plate tightly. Trace NMP was also spread on the surface of the Al foil to clean and improve the wettability of the slurry with Al foil. The trace NMP on the Al surface was wiped using kimwipes before casting an electrode. Electrical vinyl tapes

were used to control the thickness and hold the aluminum foil in place. After placing electrical tapes, the casting surface was further cleaned for NMP using kimwipes. The slurry was poured on the casting surface and spread out using a scraper blade. The ratio of the height of the blade and the final electrode thickness (in the dry state) was set approximately 3:1 of the final target thickness. Then, the laminate was dried at 65°C overnight under vacuum to prepare the sulfur cathodes. The electrodes were cut into a small disk of 15 mm in diameter with a punch and then assembled into CR2032 coin cells with lithium metal as the negative electrodes in an Ar-filled glove box. Two Celgard 2400 polypropylene membrane (20 mm diameter) was used as the separator. The electrolyte solution was 1.0 M lithium bis-(trifluoromethanesulfonyl) imide (LiTFSI) salt in a solvent mixture of dimethoxyethane (DME) and 1,3-dioxolane (DOL) (V/V = 1:1), including 0.1 M $LiNO_3$ as an additive. After assembling the Li-S coin cells, they were taken out of glove box and wiped with alcohol before putting for testing. Cyclic voltammetry (CV) and Galvanostatic charge-discharge were performed to characterize the electrochemical performance of prepared cells.

(ii) Cyclic Voltammetry (CV)

Cyclic voltammetry is one of the most commonly used techniques for the characterization of the electrochemical system. During CV experiment, the potentiostat applies a potential ramp to the working electrode to change the potential gradually. When CV reaches a set potential, the working electrode's potential ramp is reversed and returns to the initial potential. For plotting the CV graph, the current at the working electrode is plotted versus the applied voltage. Figure 3.6 illustrates a simplified electrochemical measurement circuit for cyclic voltammetry analysis. The circuit consists of an electrochemical cell, an adjustable voltage source (V_S), an ammeter (A_M),

and a voltmeter (V_M). The three electrodes of the electrochemical cell are the working electrode (WE), reference electrode (RE), and the counter (or auxiliary) electrode (CE). A potential scan is applied using the voltage source (V_S) between the WE and CE. The potential (E) between the reference electrode and the working electrode is measured with the voltmeter, and the overall voltage (V_S) is adjusted to maintain the desired potential at the WE with respect to the RE. The resulting current (i) flowing to or from the WE is measured with the ammeter (A_M). The following procedure can be performed to obtain cyclic voltammetry plot:

1. Select a potential (E) for RE with respect to WE.
2. Adjust the voltage across the entire cell (CE to WE) to get desired E (closed loop control).
3. Measure the resultant current (i).
4. Select (step) a new E and repeat procedure until the scan is finished. If the procedure is a single sweep between two potentials, this is called linear sweep voltammetry. In case of cycle voltammetry, the sweep is reversed when the potential reaches at a certain point. This cycle may be repeated multiple times during an experiment.
5. Plot the measured currents as a function of the potential to obtain cyclic voltammetry graph.

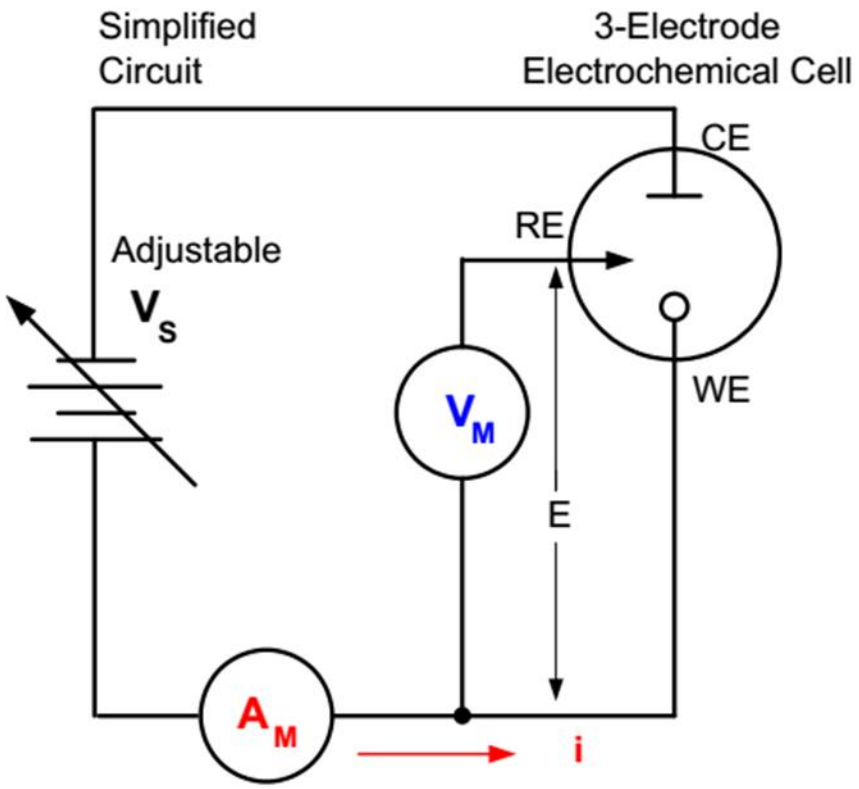

Figure 3.6: Simplified measurement circuit for performing cyclic voltammetry[18].

An example of CV is shown in Figure 3.7 that includes four voltage points: E1 (initial potential), E2 (second, switching potential), E3 (third, switching potential), and E4 (final potential). The voltage peaks in the waveform are the anodic (Epa) and the cathodic (Epc) peak potentials. In this example, the scan begins at E1 and the potential becomes increasing more positive causing the anodic current to rise rapidly and peak at the anodic peak potential (Epa). At E2, the scan direction reverses to negative for the reverse scan. As the current becomes more negative, cathodic current will flow as the electrode process is reduced. A cathodic peak potential occurs at Epc. At the third potential, E3, the direction is reversed again and the voltage is swept until it reaches E4. From the potential sweep, important information about the experiment can be derived and analyzed.

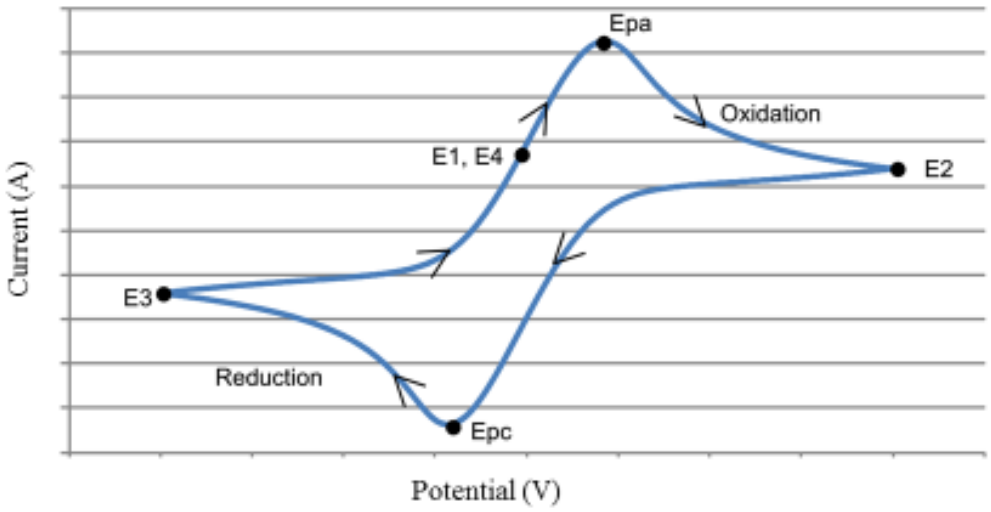

Figure 3.7: Example of cyclic voltammogram[18].

In this study, the CV measurements were performed from 1.5 to 3.0 V at a scanning rate of 0.2 mV s^{-1} by using Gamry Potentiostat. Sulfur-carbon cathode composite was used as working electrode whereas lithium was used as reference and counter electrode.

(iii) Galvanostatic Charging/Discharging Measurement

Galvanostatic charge-discharge measurement is one of the most popular characterization techniques of batteries to evaluate cycle performance of the battery. During galvanostatic charge/discharge measurement, a constant current is applied to the working electrode, and its resulting potential is measured against a reference electrode as a function of time. The constant anodic/cathodic current applied to the electrode causes the electroactive species to be oxidized/reduced at a constant current, and the electrode potential varies with time. The number of electrons transferred is counted from the start to the end of the cycle. The cycle ends when the

voltage reaches the target voltage set by the user. The C-rate is a measure of the rate at which a cell is charged or discharged with respect to its maximum capacity. For Li-S battery, assuming completely theoretical 100% utilization of sulfur, one gram of sulfur in a battery would take 1675 mA to discharge in one hour. Thus, the maximum capacity of Li-S cell is 1675 mAh g^{-1} and 1 C-rate = 1675 mA g^{-1}.

Charge or Discharge capacity is calculated followed by

$$\text{Capacity} = \text{Current rate} \times \text{time} \qquad \text{(Eq. 17)}$$

For example, a cathode weight of 10 mg with 70% carbon-sulfur composite and 60% sulfur loading on the composite, will have 0.70 × 10 mg × 0.60 = 4.2 mg sulfur. For 1 C = 1675 mA g^{-1}, maximum theoretical current rate for the cathode electrode will be 1675×4.2/1000 = 7.035 mA. At 1 C-rate and 0.2 C, current will be 7.035 mA and 1.407mA, respectively. For 4 h discharge time at 1 C-rate, specific capacity will be:

7.035 mA × 4 h = 28.14 mAh/cathode or 28.14/0.042 = 670 mAh/g based on sulfur weight.

Another important parameter is Coulombic efficiency which can be defined as the ratio of discharge and charge capacity of a cell.

$$\text{Coulombic efficiency} = (\text{discharge capacity} / \text{charge capacity}) \times 100\% \qquad \text{(Eq. 18)}$$

In the current study, the galvanostatic charge-discharge cycling was performed in a coin cell (CR 2032) on Land Instruments. In the case of Li-S cell, fresh cells were at first discharged to 1.7 V vs. Li/Li^+ followed by charging to 2.8 V vs. Li/Li^+.

References

1. Sadhwani, N., Adhikari, S. & Eden, M. R. Biomass Gasification Using Carbon Dioxide: Effect of Temperature, CO2/C Ratio, and the Study of Reactions Influencing the Process. *Ind. Eng. Chem. Res.* **55,** 2883–2891 (2016).
2. Abdoulmoumine, N., Kulkarni, A. & Adhikari, S. Effects of temperature and equivalence ratio on pine syngas primary gases and contaminants in a bench-scale fluidized bed

gasifier. *Ind. Eng. Chem. Res.* **53,** 5767–5777 (2014).
3. Kulkarni, A., Baker, R., Abdoulmomine, N., Adhikari, S. & Bhavnani, S. Experimental study of torrefied pine as a gasification fuel using a bubbling fluidized bed gasifier. *Renew. Energy* **93,** 460–468 (2016).
4. Thangalazhy-Gopakumar, S. *et al.* Physiochemical properties of bio-oil produced at various temperatures from pine wood using an auger reactor. *Bioresour. Technol.* **101,** 8389–8395 (2010).
5. Otowa, T., Nojima, Y. & Miyazaki, T. Development of KOH activated high surface area carbon and its application to drinking water purification. *Carbon N. Y.* **35,** 1315–1319 (1997).
6. Wennerberg, A. N. & O'Grady, T. M. Active carbon process and composition. 7 (1978).
7. Ji, X., Lee, K. T. & Nazar, L. F. A highly ordered nanostructured carbon-sulphur cathode for lithium-sulphur batteries. *Nat. Mater.* **8,** 500–506 (2009).
8. Xin, S. *et al.* Smaller Sulfur Molecules Promise Better Lithium − Sulfur Batteries. *J. Am. Chem. Soc.* **134,** 2–5 (2012).
9. Perkin Elmer. A Beginner's Guide Introduction. *Perkin Elmer* 3–19 (2004). doi:10.1198/tech.2005.s328
10. Klobes, P., Meyer, K. & Munro, R. G. Porosity and specific surface area measurements for solid materials. (2006).
11. Rouquerol, J. *et al.* Recommendations for the characterization of porous solids (Technical Report). *Pure Appl. Chem.* **66,** 1739–1758 (1994).
12. Hodkiewicz, J. Characterizing carbon materials with Raman spectroscopy. *Thermo Sci. Appl. Note* **51946,** (2010).
13. Gao Liu, H. Z. & V. S. B. Fabrication procedure for LiMn2O4/Graphite-based Lithium-ion Rechargeable Pouch Cells. *Lithium* 1–7 (2007). doi:10.2172/909518
14. Lee, G. W., Ryu, J. H., Han, W., Ahn, K. H. & Oh, S. M. Effect of slurry preparation process on electrochemical performances of LiCoO2 composite electrode. *J. Power Sources* **195,** 6049–6054 (2010).
15. Li, J., Daniel, C. & Wood, D. Materials processing for lithium-ion batteries. *J. Power Sources* **196,** 2452–2460 (2011).
16. Kim, K. M., Jeon, W. S., Chung, I. J. & Chang, S. H. Effect of mixing sequences on the electrode characteristics of lithium-ion rechargeable batteries. *J. Power Sources* **83,** 108–113 (1999).
17. Yang, H. & Jiang, P. Large-scale colloidal self-assembly by doctor blade coating. *Langmuir* **26,** 13173–13182 (2010).
18. Tektronix. *Performing Cyclic Voltammetry Measurements Using Model 2450-EC or 2460-EC Electrochemistry Lab System*.

CHAPTER 4: RESULTS AND DISCUSSION

This chapter includes the results that have been obtained during the thesis work along with the discussion of the significant results. Initially, physical and chemical characterization results are presented and discussed followed by the analysis of electrochemical characterization results.

4.1 PHYSICAL AND CHEMICAL CHARACTERIZATION

Samples were characterized to evaluate their physical and chemical characteristics. Physical properties such as surface area, porosity, scanning electron microscopy and sulfur loading within the sulfur-carbon (S/C) composite were evaluated. Chemical characterization such as carbon, nitrogen, hydrogen and sulfur content measurement, Raman and FTIR spectroscopy are discussed here.

4.1.1 Elemental Analysis

The ash content of samples was determined using TGA analysis. The ash content was calculated based on the weight of the sample remained after heating at 750˚C and presented in Table 4.1. From Figure 4.1 and Table 4.1, it can be found that the ash content in biomass, biochar and activated biochar derived from Douglas-fir did not have significant variation in comparison to the biomass, biochar and activated biochar derived from canola meal. Canola meal biomass and

activated biochars have lower ash content than the biochars. From Figure 4.1c, it can be observed that all four activated biochars have similar ash content and thermal decomposition characteristics.

Carbon and nitrogen contents in the samples (Table 4.1) were determined using a CHNS analyzer. Canola meal has 5.79% nitrogen, which is due to the high protein content in canola meal. Most of the nitrogen containing groups was decomposed during the KOH activation at 800°C. Thus, the nitrogen content of CF-AB and CS-AB were significantly lower than the canola meal biomass and biochars. Douglas-fir biomass itself has very low nitrogen content, and thus the biochar and activated biochar derived from Douglas-fir have insignificant nitrogen content. In the case of carbon content, a similar trend can be seen in both canola meal and Douglas-fir derived samples. Biochar samples have a higher carbon content than the biomass sample, and activated biochar samples contain significantly a higher carbon content than other samples due to a significant decomposes of non-carbon elements at high temperature (500-800°C).

Table 4.1: Elemental analysis of samples based on dry weight.

Sample	N (%)	C (%)	H (%)	S (%)	Ash (%)
C-BM	5.79 ±0.02	45.76 ±0.03	8.20 ±0.14	0.85 ±0.25	6.51 ±0.11
D-BM	0.03 ±0.01	46.36 ±0.03	7.17 ±0.13	0.84 ±0.37	1.23 ±0.04
CF-BC	5.47 ±0.10	58.71 ±0.73	2.85 ±0.10	0.94 ±0.14	25.71 ±0.18
CS-BC	6.74 ±0.11	62.57 ±0.84	4.13 ±0.07	0.56 ±0.18	19.39 ±0.23
DF-BC	0.15 ±0.01	81.66 ±0.65	3.46 ±0.09	0.23 ±0.06	1.77 ±0.05
DS-BC	0.11 ±0.02	88.39 ±0.95	3.39 ±0.04	0.26 ±0.08	2.37 ±0.09
CF-AB	0.34 ±0.01	88.65 ±0.31	0.81 ±0.02	0.27 ±0.08	3.06 ±0.06
CS-AB	1.02 ±0.06	89.47 ±0.76	1.09 ±0.01	0.47 ±0.24	1.91 ±0.04
DF-AB	0.32 ±0.01	91.65 ±0.57	0.69 ±0.03	0.38 ±0.16	2.03 ±0.09
DS-AB	0.18 ±0.0	88.41 ±0.07	1.42 ±0.15	0.55 ±0.33	1.72 ±0.05

Percentage of C, H, N and S content included ash content

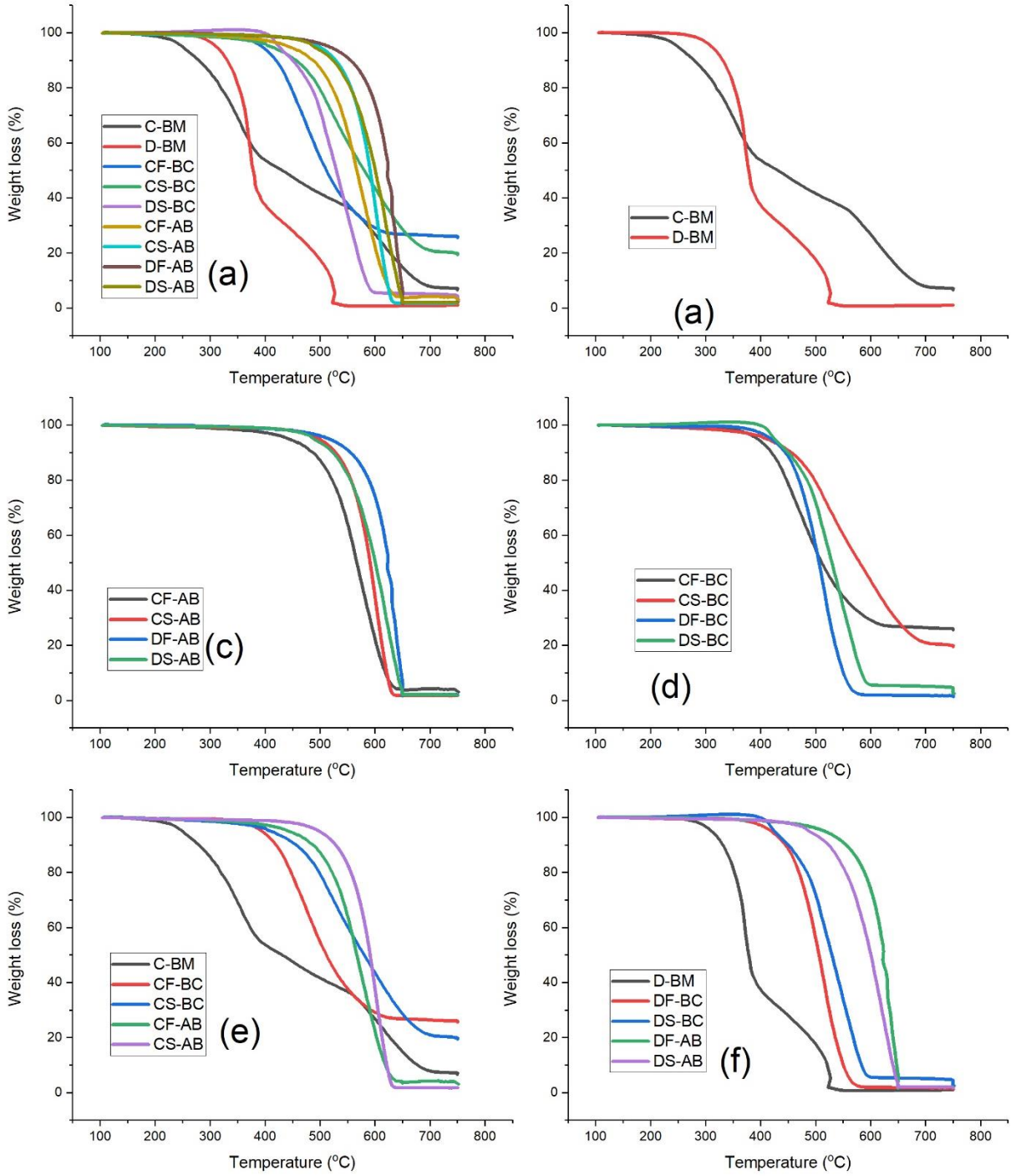

Figure 4.1: Determining ash content using the thermal decomposition of samples in air using TGA. Decomposition of (a) all samples, (b) C-BM and D-BM biomass, (c) activated biochar, (d) biochar, (e) canola meal derived samples, and (f) Douglas-fir derived samples.

4.1.2 Surface Area and Porosity Analysis

Table 4.2 shows the specific surface area, pore volume and average pore size of activated biochars and carbon black samples. Before conducting surface area and porosity analysis, samples were ball milled for 15 hours at 350 RPM for two reasons. First, for preparing the S/C composite, sulfur and activated biochar or carbon black samples were ball milled together for homogenous mixing. Thus, the surface area and pore volume of ball milled activated biochars or carbon black were required for calculating the maximum sulfur content that can be loaded with the activated biochar sample. This is why the ball milled samples were used for the surface area and porosity analysis. Second, similar particle size obtained by ball milling confirmed uniformity among all the analyzed samples. The specific surface area was determined following Brunauer–Emmett–Teller (BET) method at P/P_0 = 0.05 to 0.3 and correlation coefficient (r) value higher than 0.9975. It was found that activated biochar prepared from fast pyrolysis showed more than twice specific surface area in comparison to the activated biochar from slow pyrolysis. A similar trend can be observed in the total pore volume of the sample. Micropore volume was obtained with a Horvath–Kawazoe (HK) method considering pore width less than 2 nm. Total pore volume was obtained at P/P_0 = 0.99. Mesopore volumes were calculated by subtracting the micropore volume from the total pore volume. Macropores were broken down into smaller pores of pore width less than 40 nm due to ball milling, which can be confirmed from the pore size distribution graphs shown in Figure 4.3. Pore size distributions were obtained following N_2-NLDFT method for slit type pores. Activated biochars from fast pyrolysis (such as CF-AB and DF-AB) mainly consist of micropores and small mesopores with pore width less than 4 nm (Figure 4.3a and 4.3c). Pore size distribution of CF-AB and DF-AB were consistent with the N_2 adsorption- desorption isotherms that indicates Type I isotherm of the highly microporous structure. However, activated biochar derived from slow

pyrolysis biochar (CS-AB and DS-AB) have a significant amount of larger mesopores along with micropores (Figure 4.3b and 4.3d). From Figure 4.2b and 4.2d, it can be observed that CS-AB and DS-AB have the H4 type of hysteresis which indicates narrow slit-like pores with internal voids of irregular shape and broad pore size distribution. The pore size distribution and isotherms of CS-AB and DS-AB were consistent with each other. Carbon black has very low specific surface area and pore volume (Table 4.2). Carbon black sample (CB) has insignificant porosity in comparison to the activated biochars. From Figure 4.2e, it can be seen that CB has the H3 type of hysteresis loop[1] which indicates CB sample consists of the plate like particles forming slit-like mesopores[1], which can be confirmed from the pore size distribution of CB shown in Figure 4.3e.

Table 4.2: Specific surface area, pore volume and average pore size of activated biochar and carbon black.

Sample	Specific Surface Area	Pore Volume			Average Pore Size
		Micropore	Mesopore	Total	
	$m^2 g^{-1}$	$cm^3 g^{-1}$	$cm^3 g^{-1}$	$cm^3 g^{-1}$	nm
CF-AB	3355±114	1.1±0.06	0.48±0.01	1.58±0.07	2.09±0.03
CS-AB	1655±39	0.69±0.01	0.11±0.01	0.80±0.01	2.19±0.13
DF-AB	3227±163	1.26±0.05	0.23±0.01	1.49±0.01	2.05±0.06
DS-AB	1045±42	0.50±0.02	0.03±0.02	0.53±0.02	2.24±0.13
CB	58±2	0.02±0.01	0.15±0.01	0.12±0.01	6.55±0.11

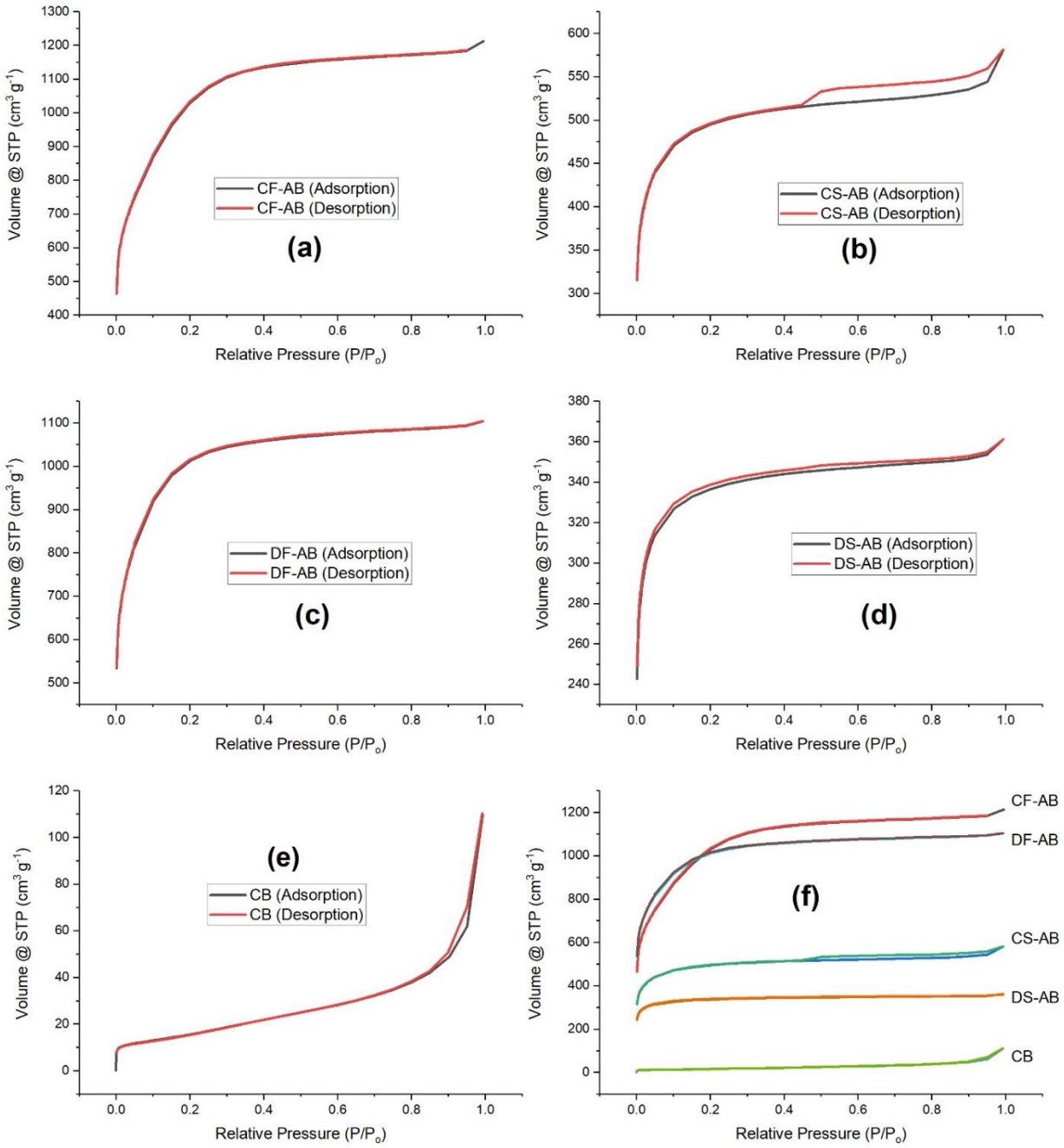

Figure 4.2: N_2 adsorption-desorption isotherms of activated biochar and carbon black

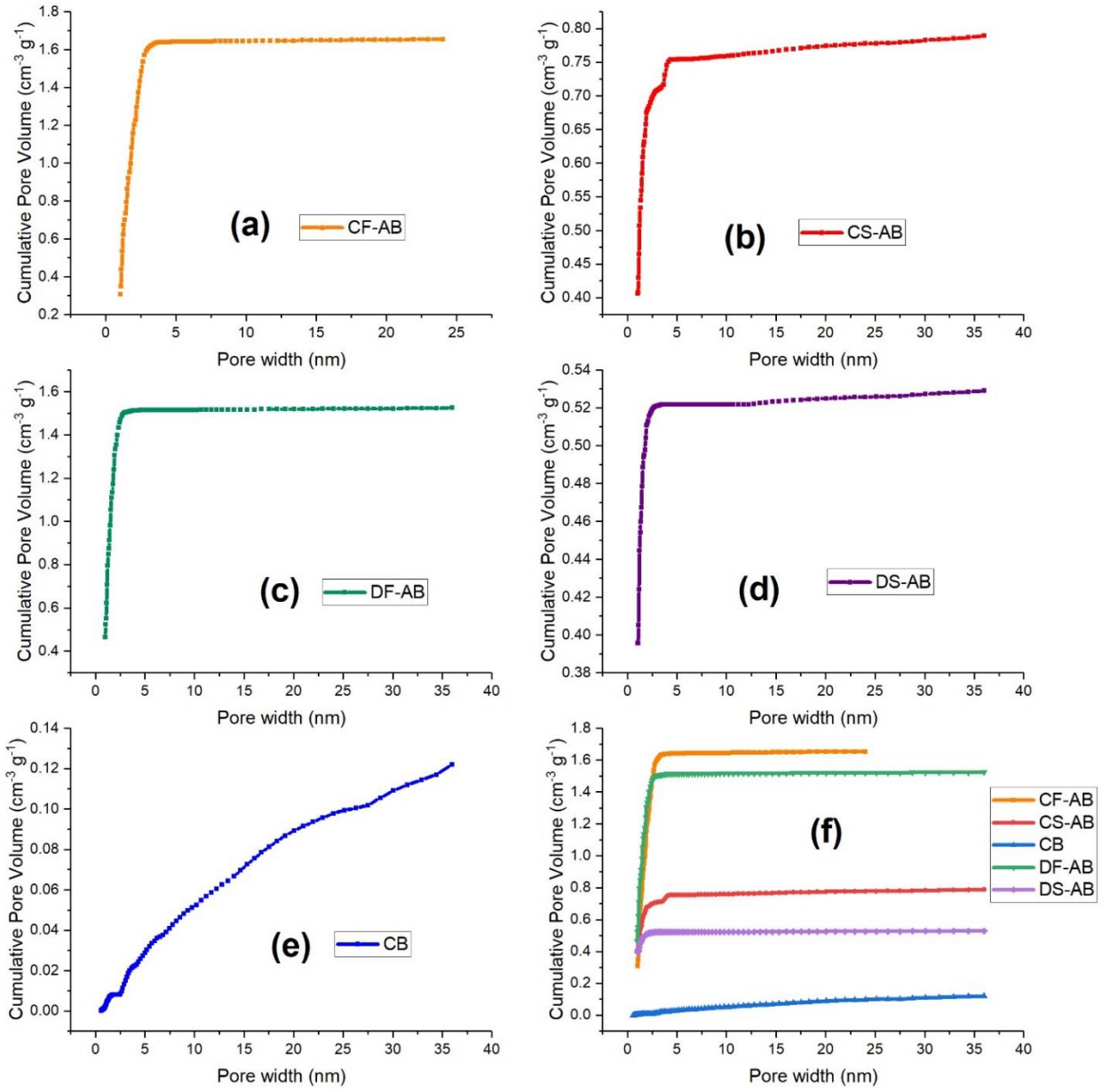

Figure 4.3: Pore size distribution of activated biochars and carbon black sample.

4.1.3 Scanning Electron Microscopy (SEM)

Scanning electron microscopy (SEM) was performed to investigate the morphological characteristics of the samples which are shown in Figure 4.4 to 4.10. In Figure 4.4a and 4.4b, SEM images of biochar derived from canola meal (a) and Douglas-fir (b) is shown. Canola meal derived

biochar does not have any visible macrostructure like the Douglas-fir derived biochar. In Figure 4.5a and 4.6a, the SEM images of CF-AB and CS-AB are shown, where the presence of macrostructure is visible. However, after ball milling, the macrostructure broken down to smaller structure and thus, the pores were not visible in Figure 4.5b and 4.6b. The similar morphological structure change due to ball milling can be observed for Douglas-fir derived activated biochar (DF-AB and DS-AB) in Figure 4.7 and 4.8.

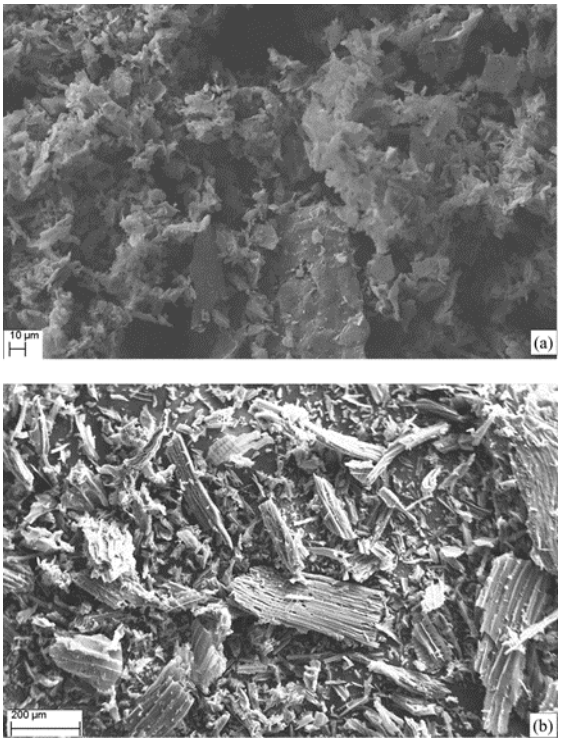

Figure 4.4: SEM images of (a) canola meal biochar and (b) Douglas-fir biochar

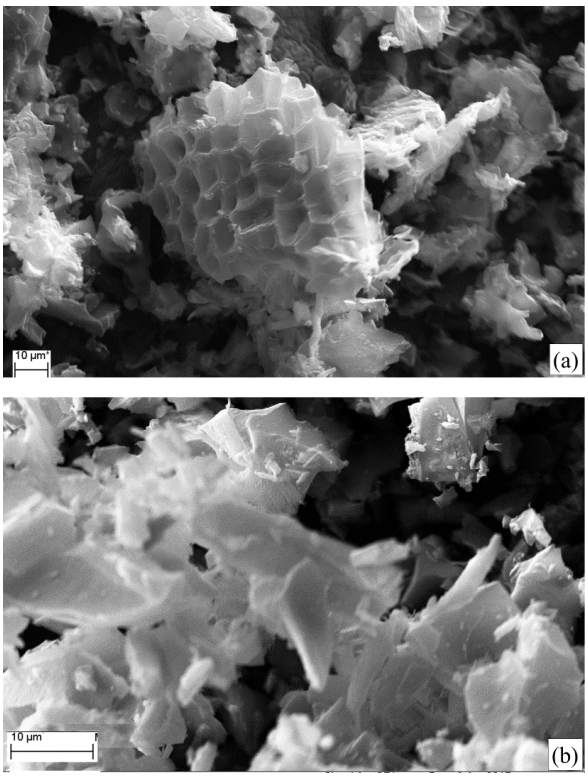

Figure 4.5: SEM images of CF-AB (a) before ball milling and (b) after ball milling

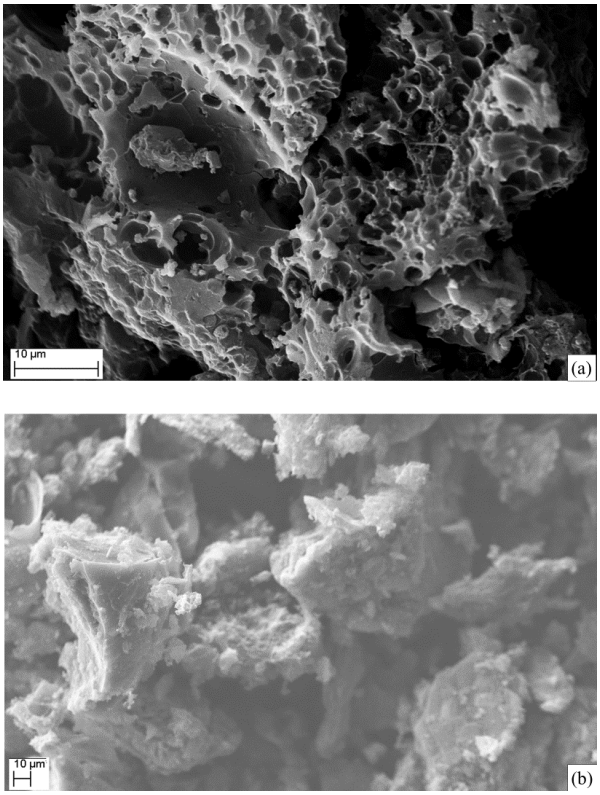

Figure 4.6: SEM images of CS-AB (a) before ball mill and (b) after ball mill

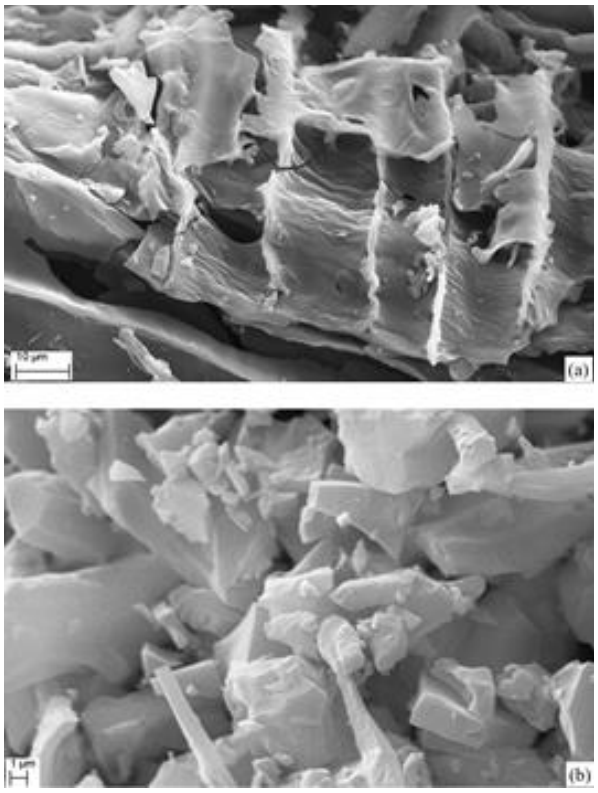

Figure 4.7: SEM image of DF-AB (a) before ball mill and (b) after ball mill

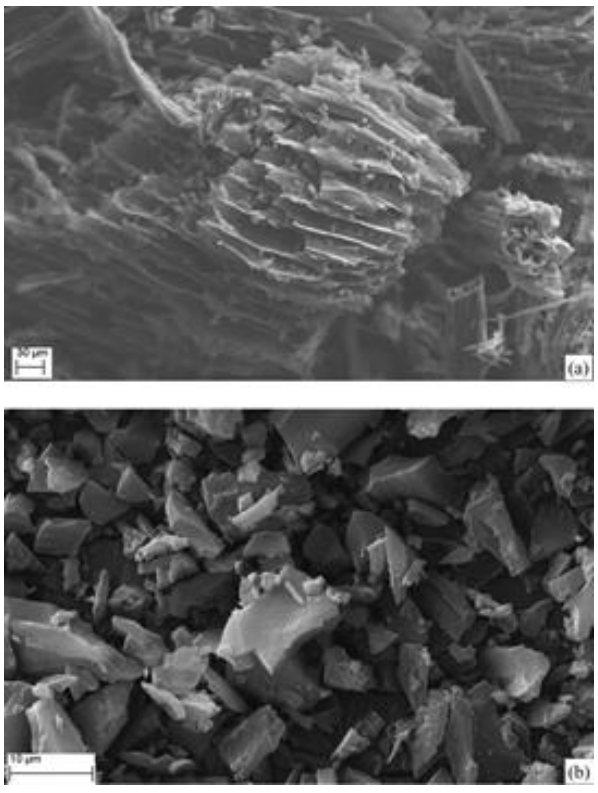

Figure 4.8: SEM image of DS-AB (a) before ball mill and (b) after ball mill

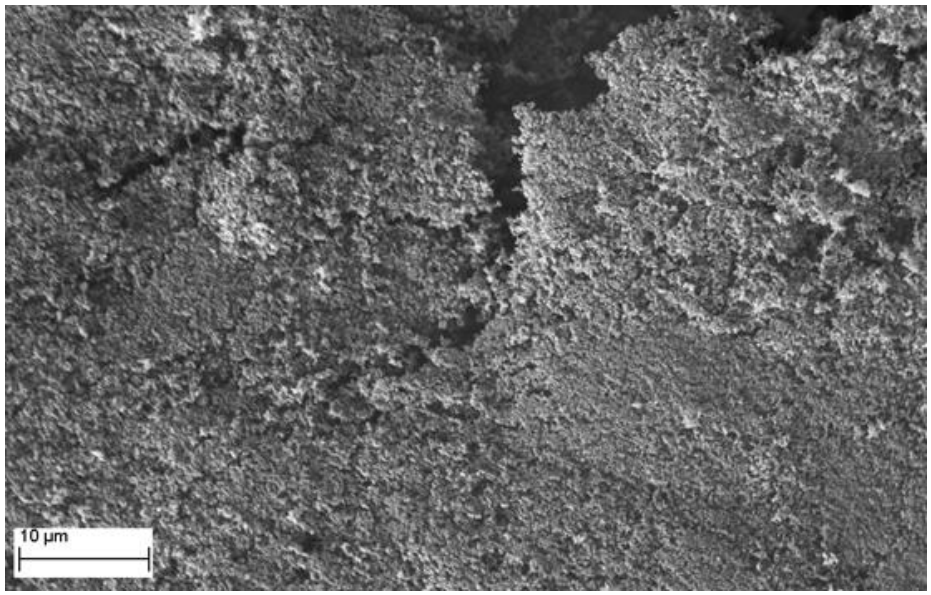

Figure 4.9: SEM image of CB without ball mill

Figure 4.9 shows the morphological structure of carbon black sample which does not have any significant macrostructure. In Figure 4.10, the change of sulfur-carbon surface before heat treatment (a) and after heat treatment (b) at 155°C is shown. Before heat treatment, sulfur particles can be easily observed on the surface of porous CS-AB activated biochar (Figure 4.10a). After heat treatment, pores on the porous carbon got covered and filled with sulfur. The white flakes were activated biochar particles covered with sulfur.

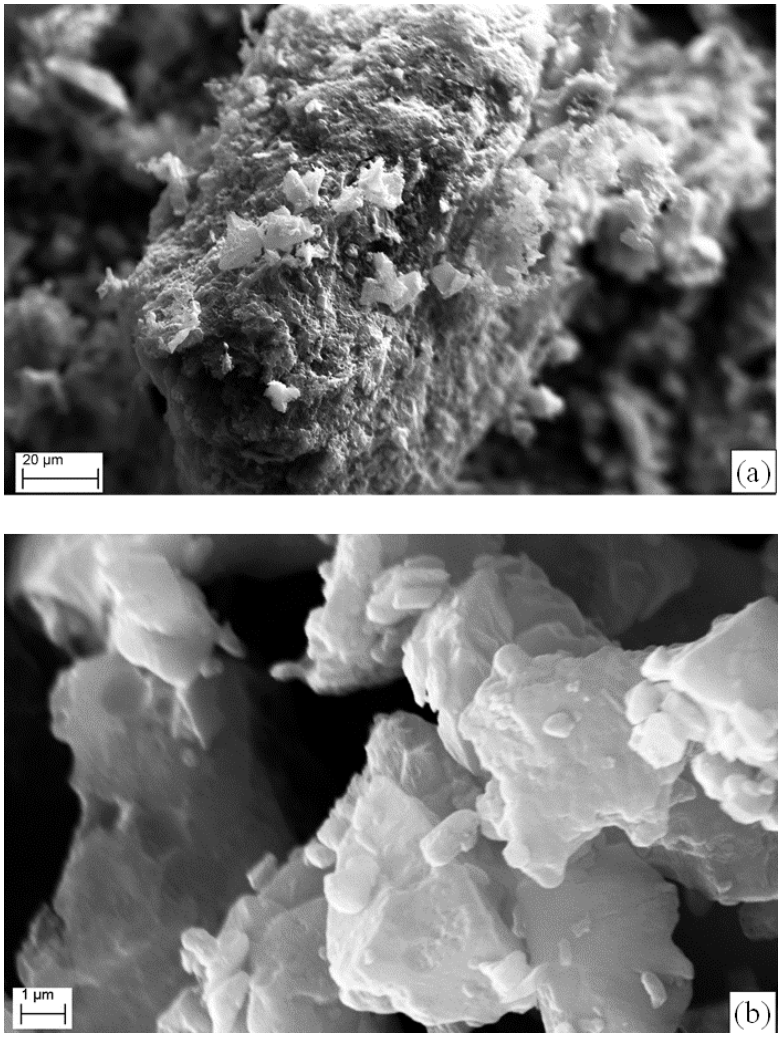

Figure 4.10: SEM images of sulfur and CS-AB (a) before heat treatment and (ii) after heat treatment

4.1.4 Sulfur Loading in Sulfur-Carbon Composites

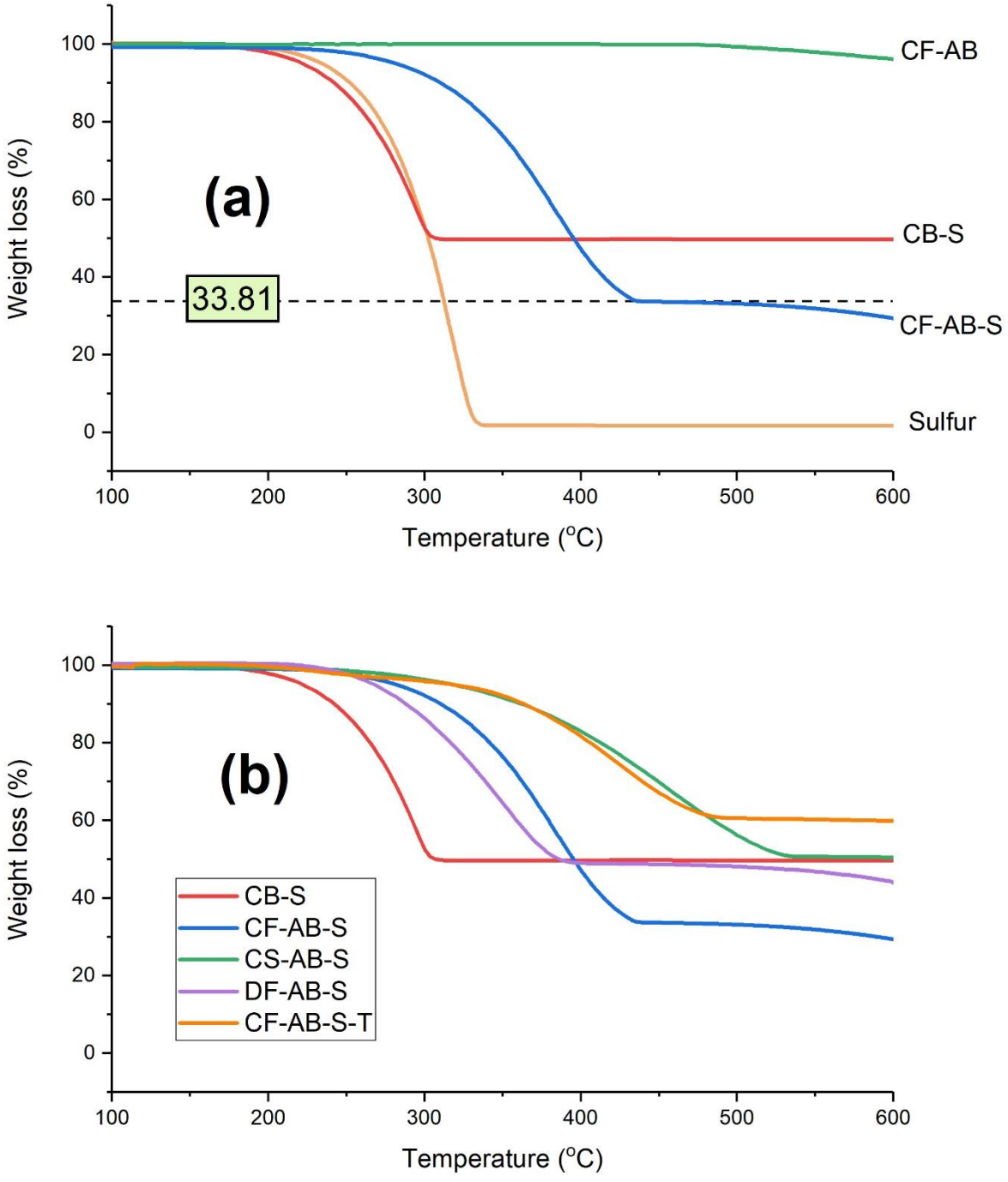

Figure 4.11: (a) Determination of the sulfur content using TGA and (b) TGA analysis of sulfur-carbon composites

For determining the amount of sulfur loaded into a sulfur-carbon composite, TG analysis was performed. Carbon materials such as activated biochar or carbon black can withstand high temperature above 600°C under nitrogen flow. Since sulfur starts to vaporize at the around 444°C, all the sulfur would vaporize leaving behind porous carbon when the temperature is near 444°C in nitrogen or argon environment. The change of mass measured by the TGA would determine the percentage of sulfur in a sulfur-carbon composite. Sulfur composition in CF-AB-S composite was determined by the change of mass (Figure 4.11a).

Figure 4.11a shows that sublimed sulfur started to vaporize at around 200°C and completely vaporized before 340°C. Due to very little porosity of carbon black, CB-S composite has all the sulfur on its surface. Thus, the sulfur of CB-S vaporized at the temperature similar to sublimed sulfur. Since activated biochar was highly porous, sulfur vaporization temperature was higher as it takes high energy to vaporize sulfur molecules that were confined within micropores (Shown in Figure 4.11a and 4.11b). Since CS-AB was mostly microporous, CS-AB-S required a higher temperature to vaporize the micropore-confined sulfur. CF-AB and DF-AB have a significant portion of mesopores. Thus, sulfur existing in CF-AB-S and DF-AB-S required lower vaporization temperature than CS-AB-S. However, CF-AB-S-T showed similar vaporization temperature as CS-AB-S. This can be attributed to the reason that the sulfur existing on the mesopores or surface of CF-AB-S were washed by toluene and only micropore-confined sulfur remained. Table 4.3 shows the sulfur loading in prepared S/C composite that is determined using TGA and CHNS. In this study, sulfur content determined using TGA was considered.

Table 4.3: Sulfur loading in prepared sulfur-carbon composites

Sample	S (%)	
	TGA	CHNS
CF-AB-S-T	39.0 ± 0.7	33.03 ± 0.6
CF-AB-S	66.2 ± 0.6	71.25 ± 1.8
CS-AB-S	49.3 ± 0.73	51.03 ± 1.1
DF-AB-S	51.8 ± 1.21	54.18 ± 1.4
CB-S	50.5 ± 0.5	52.3 ± 0.1

4.1.5 Raman Spectroscopy

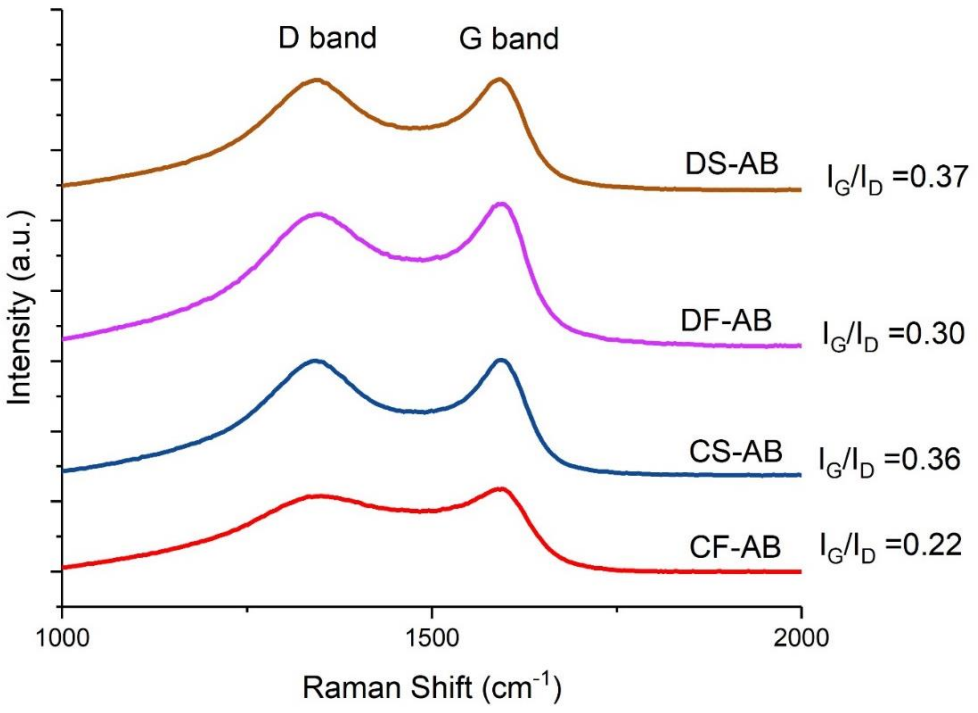

Figure 4.12. : Raman spectroscopy of activated biochars

Table 4.4: Raman spectroscopy data

Sample	D band (cm^{-1})	G band (cm^{-1})	I_G/I_D
CF-AB	1350	1595	0.22
CS-AB	1340	1592	0.36
DS-AB	1344	1592	0.37
DF-AB	1350	1589	0.30

Raman spectroscopy is an excellent tool for analyzing carbon materials as their Raman spectra have been shown to be sensitive to changes in the microscopic structure of the material[2]. In Raman spectrum for carbon materials, the G band corresponds to the allowed Raman transition for large graphite crystals and is thus indicative of graphitic layers, while the D band corresponds to disordered carbon or defective graphitic structures[2–4]. The characteristic D and G peaks were observed at 1340-1350 cm^{-1} and 1589-1595 cm^{-1}, respectively (Figure 4.12).

The relative intensity ratio I_G/I_D ratio is proportional to the ordered graphitic structure of the carbon material[3,5]. Higher graphitic structure indicates higher conductivity of a carbon material[3]. The I_G/I_D ratio obtained (by area) for the prepared activated biochars were in the order: CF-AB < DF-AB < CS-AB < DS-AB. Through KOH activation, more defects and pore structure is generated on activated biochar. CF-AB has the lowest I_G/I_D ratio or highest defective graphitic structure or amorphous carbon, which is consistent with the results from the surface area and porosity analysis.

4.1.6 Fourier Transform Infrared Spectroscopy (FTIR)

FTIR spectroscopy is performed to investigate the presence of surface functionalities. Biomass and biochar have surface functionalities as shown in Figure 4.13. However, FTIR spectra of activated biochar show diminishing surface functionalities in comparison to biomass and biochar[6]. A common peak at around 2400 cm^{-1} is due to CO_2 impurities.

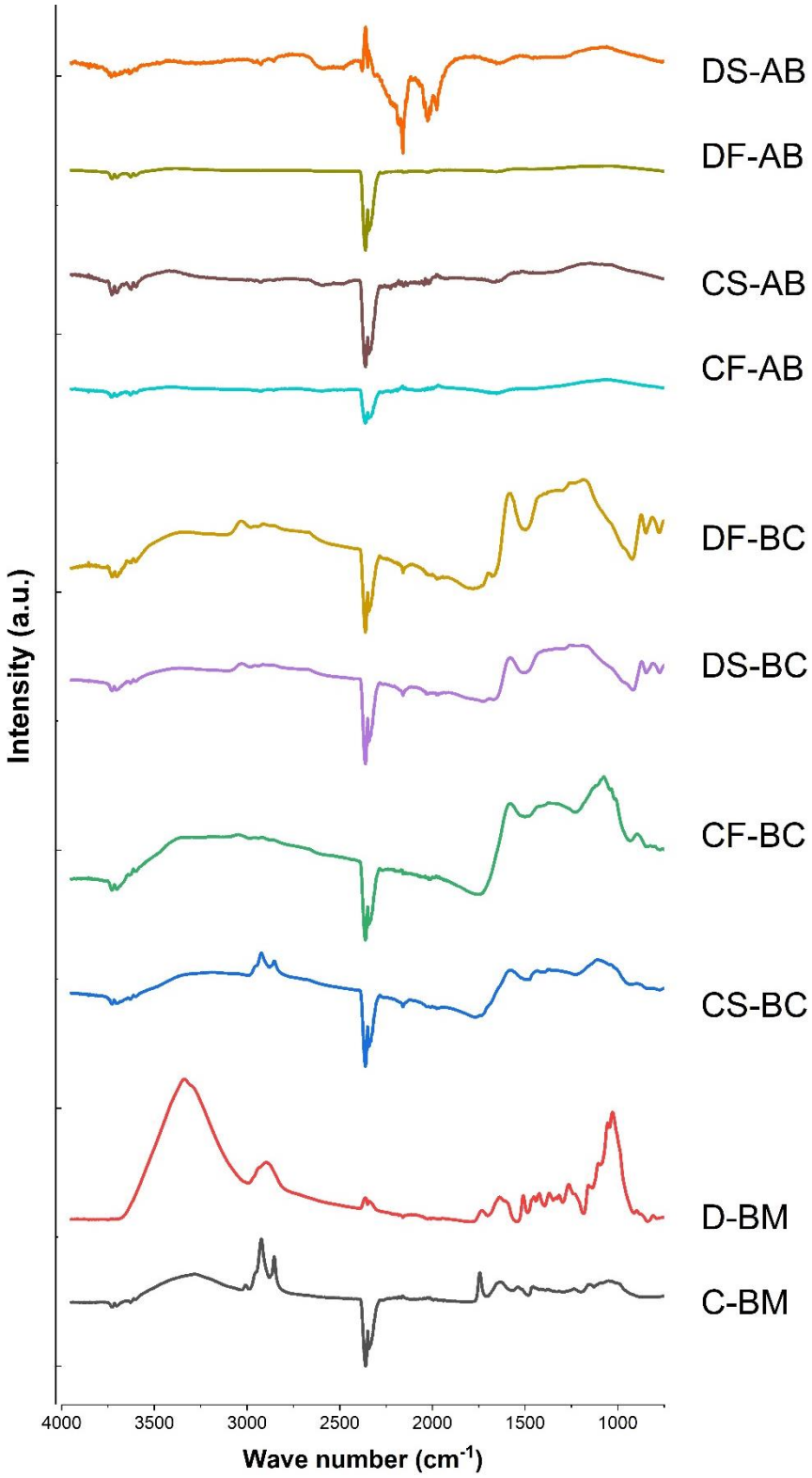

Figure 4.13: FTIR spectra of biomass, biochar and activated biochar sample from canola meal and Douglas-fir.

4.2 ELECTROCHEMICAL CHARACTERIZATION

Electrochemical characterization such as galvanostatic charge-discharge measurement and cyclic voltammetry was performed to evaluate the performance and to investigate electrochemical characteristics of prepared Li-S cells. Additionally, the effect of lithium anode diameter on specific discharge capacity is also discussed.

4.2.1 Galvanostatic Charge-Discharge Measurement

Electrochemical performance of prepared five Li-S cells (such as CF-AB-S, CF-AB-S-T, CS-AB-S, DF-AB-S, and CB-S) was evaluated through charge-discharge measurement at six different current density (such as 0.05 C, 0.1 C, 0.2 C, 0.5 C, 1 C and 2 C-rate). A 1 C rate, it will take 1 hour to discharge the entire battery. For Li-S cells, 1 C rate of sulfur electrode is equivalent to 1675 mA g^{-1}. All the cells that have been tested shown a decrease in specific discharge capacity with an increase of current density (Figure 4.14). At first cycle, the cells exhibited their highest performance which decreased with an increase of cycle number. This capacity reduction can be attributed to the reduction of sulfur into insoluble and insulating Li_2S leading to active material loss. Additionally, at very low current density, lithium polysulfides gets more time to get dissolved into the electrolyte and cause shuttle phenomena[7]. Coulombic efficiency of the first five cycles were among the lowest in comparison to other cycle performance (Figure 4.15) which supports the previous statement. After 6^{th} cycle, all the cells exhibited stable performance which could be attributed to the stability of the cells (Figure 4.14 and 4.15). At 2 C rate, all the prepared cells showed their lowest discharge capacity which could be attributed to increse of resistance due to incresed current density. However, the discharge capacity (Figure 4.14) of the cells incresed after

35th cycles at lower current density (0.2 C). Increment of the capacity can be attributed to the decrese of resistance.

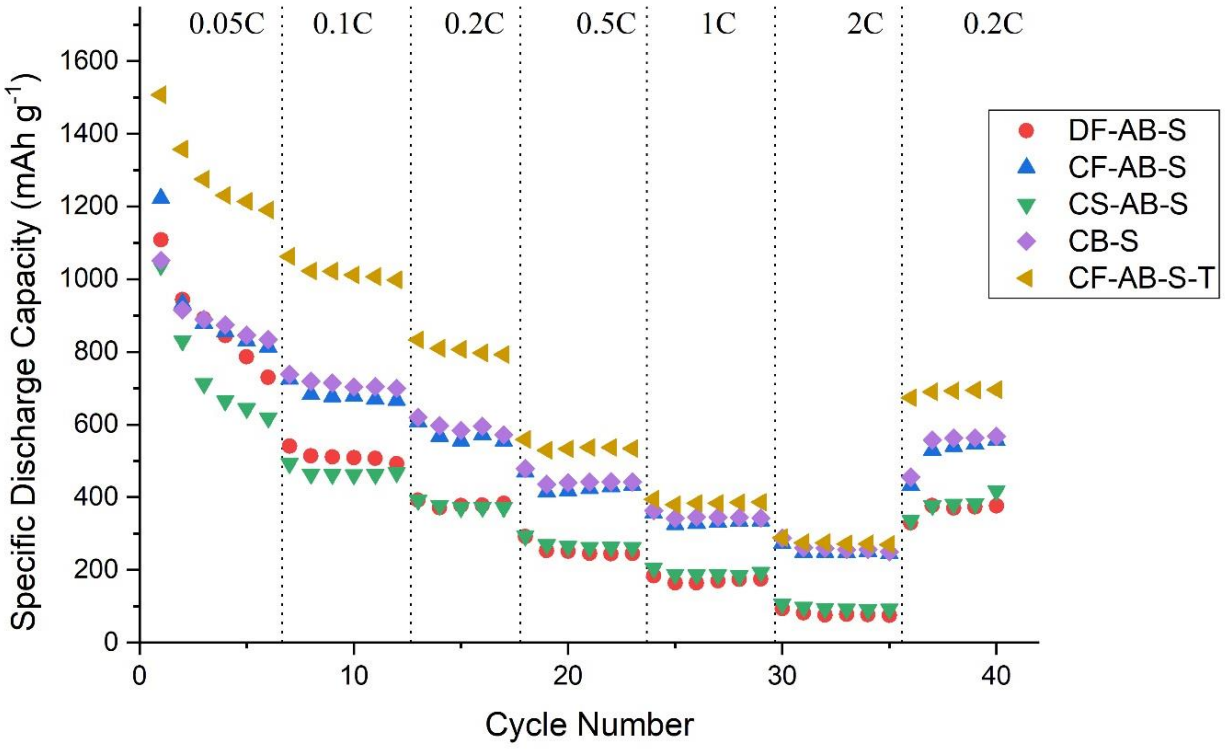

Figure 4.14: Specific discharge capacity of prepared Li-S cells at five different current density.

As shown in the Figure 4.14, CF-AB-S-T exhibited the best performance, among all the cathode composites, with an initial discharge capacity of 1507 mAh g^{-1} at 0.05 C rate. Other cathode composite exhibited significantly lower initial discharge capacity in comparison to CF-AB-S-T. CF-AB-S-T was prepared by removing sulfur from the surface of CF-AB-S by dissolving the sulfur in toluene and removed by centrifugation. This way, only the micropores-confined sulfur remained in CF-AB-S-T (39% of the composite is sulfur). This composite exhibited 288-270 mAh

g^{-1} at 2 C rate at 30-35th cycles, and then 670-695 mAh g^{-1} at 0.2 C rate at the 36-40th cycling period. This exhibited the capacity retention capability of the composite.

Another cathode composite CF-AB-S prepared using CF-AB activated biochar exhibited initial discharge capacity of 1222 mAh g^{-1}. Although CF-AB-S and CF-AB-S-T were prepared using the same CF-AB sample, CF-AB-S exhibited lower initial capacity and cycle performance which could be attributed to the high sulfur content at CF-AB-S. If the sulfur content is too high, insoluble Li_2S_2 or Li_2S having lower conductivity can readily be generated during the discharge process, resulting in lower sulfur utilization and rapid decline of specific capacity[8].

CB-S composite, prepared using commercial conductive carbon black, exhibited similar performance as CF-AB-S although carbon black has insignificant porosity in comparison to CF-AB activated biochar. The performance of the CB-S can be attributed to highly conductive nature of carbon black as insulating sulfur needs to be integrated into a composite with conducting host material.[9]

Cathode prepared from CS-AB and DF-AB activated biochar exhibited initial discharge capacity as 1037 and 1107 mAh g^{-1}. For first six cycles at 0.05 C, CS-AB and DS-AB exhibited 1037-618 mAh g^{-1} and 1107-730 mAh g^{-1}. However, the specific discharge capacity decreased with an increment of cycle number which can be attributed to the generation of insoluble Li_2S_2 or Li_2S with lower conductivity because of too high sulfur content[8].

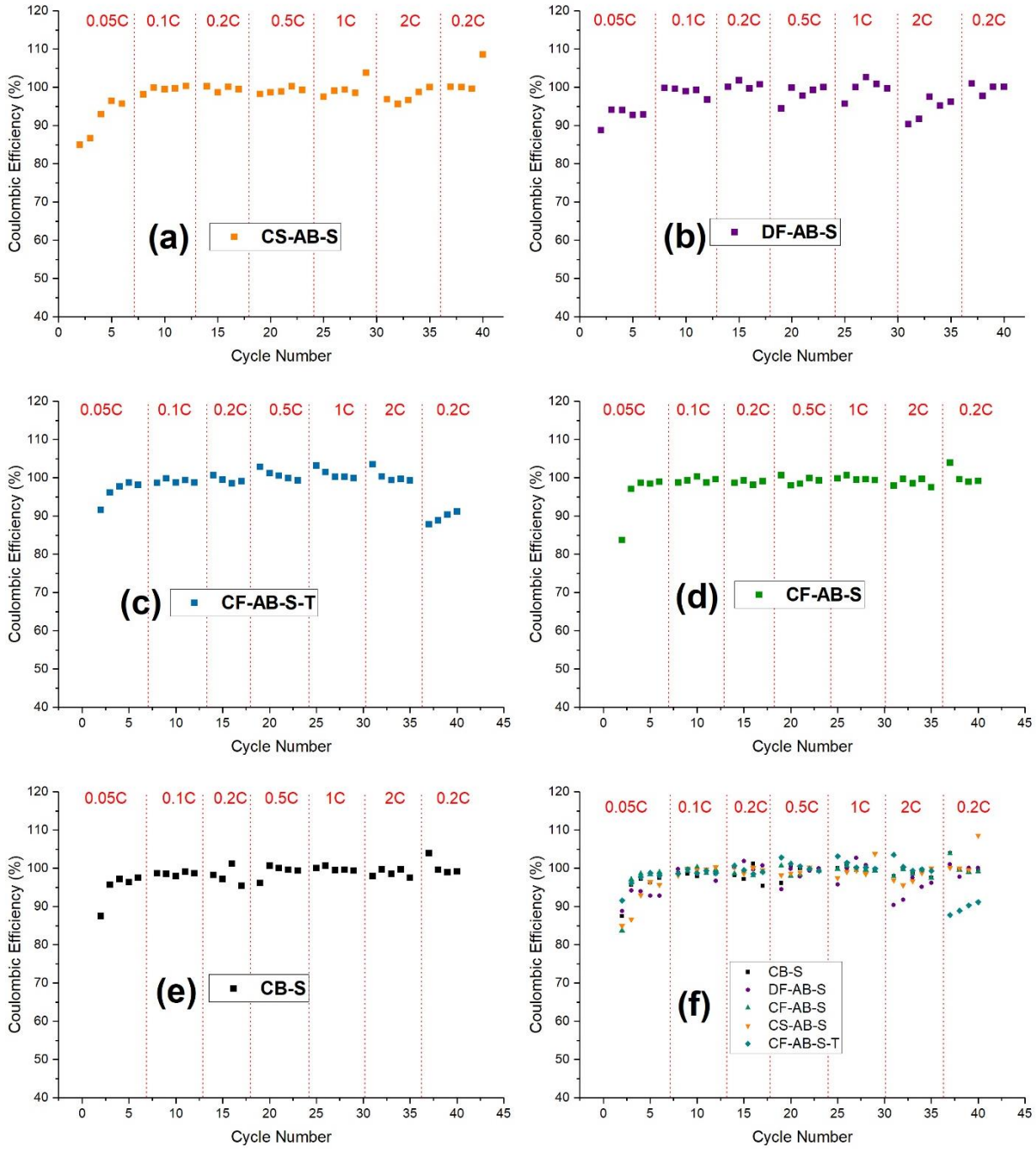

Figure 4.15: Coulombic efficiency (a) CS-AB-S, (b) DF-AB-S, (c) CF-AB-S-T, (d) CF-AB-S, (e) CB-S, and (f) all cathode composite at different current density and cycle number.

Table 4.5: Capacity loss at 0.2 C rate from 13th to 40th cycle.

Sample	Capacity loss from 13th to 40th cycle
CF-AB-S	8.34
CF-AB-S-T	16.5
CS-AB-S	-6.63
DF-AB-S	4.07
CB-S	8.31

The coulombic efficiency of the prepared cells at six different current density have been shown in Figure 4.15. Except for the first five cycles, coulombic efficiency of the prepared cells were more than 80% for other cycles. Table 4.5 shows that slow pyrolysis derived CS-AB-S exhibited lowest capacity loss among all the cathode composite tested. CS-AB-S also manitained columbic efficiency higher than 95% except for the first 6 cycles. This stable performance of this cathode composite can be attibuted to reduction of polysulfides dissolution and shuttle due to high nitrogen content[5,10].

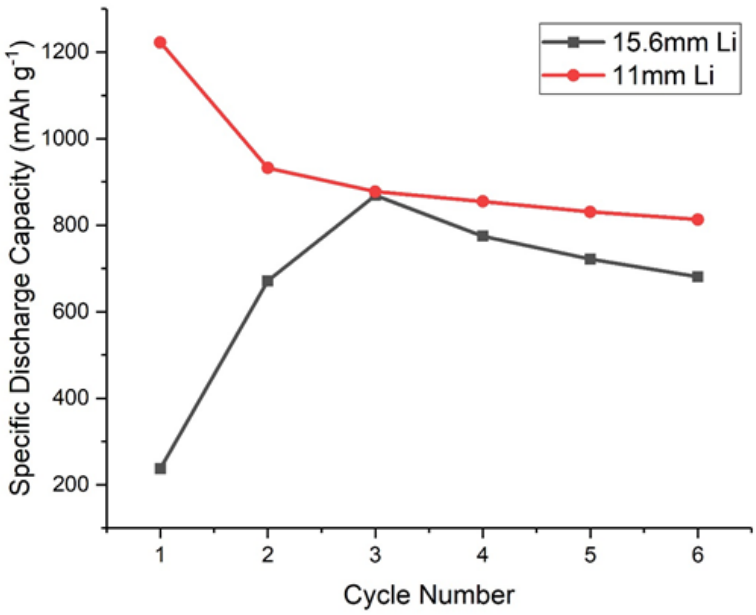

Figure 4.16: Comparison of specific discharge capacity obtained for lithium chip diameter of 15.6 mm and 11 mm.

Li-S cells were prepared using the as-received lithium chip (MTI Corporation, Richmond, CA) of 15.6 mm diameter and punched out 11 mm diameter as an anode. Figure 4.16 shows the specific discharge capacity of Li-S cell prepared using CF-AB-S cathode of 15 mm diameter and lithium anode of 15.6 mm (black line) and 11 mm (red line) diameter. In both of the cases, 3 hours wetting time was allowed before starting the charge-discharge measurements. Li-S cells with a smaller diameter of anode showed better performance than the larger anode.

4.2.2 Cyclic Voltammetry

Cyclic voltammetry experiments were conducted to investigate the electrochemical mechanisms of the prepared Li-S cells. Figure 4.17 shows the CV curves of the (a) CF-AB-S, (b) CS-AB-S, (c) CB-S, and (d) DF-AB-S electrode at a scan rate of 0.2 mV s^{-1} during first eleven cycles. In Figure 4.17d, three reduction peaks can be observed at approximately 2.3 V, 1.8 V and 1.6 V. The peak at 2.3 V corresponds to the reduction of elemental sulfur to higher order lithium

polysulfides (Li_2S_x, 4<x<8). The second peak at 1.8 V corresponds to the reduction higher order lithium polysulfides to lower order lithium polysulfides. The last peak at 1.6V can be attributed to the reduction of lower order lithium polysulfides to insoluble Li_2S[8]. In the subsequent anodic scan, two peaks at 2.5 V and 2.7 V can be observed, which corresponds to the conversion of lithium sulfides to lithium polysulfides and sulfur[8]. From the second cycles, onward the position and areas of the CV peaks remain nearly identical with increasing cycle numbers, implying good reaction reversibility and cycling stability of the DF-AB-S composite electrode after the second cycle[8]. The CV of CF-AB-S, CS-AB-S, and CB-S also showed characteristics most similar to the CV of DF-AB-S, which is similar to CV of the typical Li-S cell.

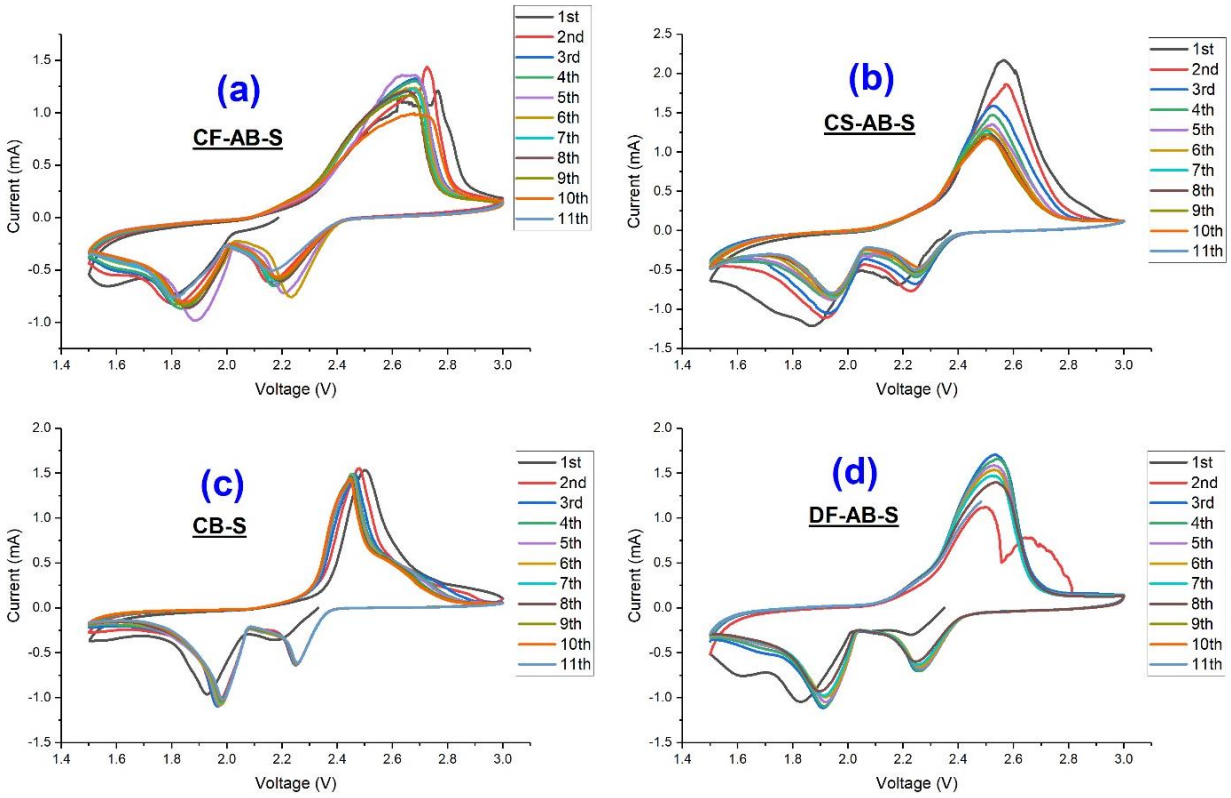

Figure 4.17: Cyclic voltammetry of Li-S cells prepared using (a) CF-AB, (b) CS-AB, (c) CB and (d) DF-AB carbon samples.

4.3 CONCLUSION

This chapter presented the physical, chemical and electrochemical characterization results that have been obtained to investigate the characteristics and properties of activated biochar for a lithium-sulfur battery application. Prepared activated biochars have a high surface area (up to 3355 m^2 g^{-1}) and pore volume (up to 1.58 cm^3 g^{-1}) which have exhibited initial specific discharge capacity up to 1507 mAh g^{-1} at 0.05 C.

References

1. Sing, K. S. W. Reporting physisorption data for gas/solid systems with special reference to the determination of surface area and porosity (Recommendations 1984). *Pure Appl. Chem.* **57,** 603–619 (1985).
2. Escribano, R., Sloan, J. J., Siddique, N., Sze, N. & Dudev, T. Raman spectroscopy of carbon-containing particles. *Vib. Spectrosc.* **26,** 179–186 (2001).
3. Genovese, M., Jiang, J., Lian, K. & Holm, N. High capacitive performance of exfoliated biochar nanosheets from biomass waste corn cob. *J. Mater. Chem. A* **3,** 2903–2913 (2015).
4. Ferrari, A. C. & Robertson, J. Interpretation of Raman spectra of disordered and amorphous carbon. *Phys. Rev. B* **61,** 14095–14107 (2000).
5. Song, J., Yu, Z., Gordin, M. L. & Wang, D. Advanced Sulfur Cathode Enabled by Highly Crumpled Nitrogen-Doped Graphene Sheets for High-Energy-Density Lithium-Sulfur Batteries. *Nano Lett.* **16,** 864–870 (2016).
6. Gray, M., Johnson, M. G., Dragila, M. I. & Kleber, M. Water uptake in biochars: The roles of porosity and hydrophobicity. *Biomass Bioenergy* **61,** 196–205 (2014).
7. Yin, Y.-X. X., Xin, S., Guo, Y.-G. G. & Wan, L.-J. J. Lithium-Sulfur Batteries: Electrochemistry, Materials, and Prospects. *Angew. Chemie Int. Ed.* **52,** 13186–13200 (2013).
8. Gu X, Wang Y, Lai C, Qiu J, Li S, Hou Y, Martens W, Mahmood N & Zhang S. Microporous bamboo biochar for lithium-sulfur batteries. *Nano Res.* **8,** 129–139 (2014).
9. Borchardt, L., Oschatz, M. & Kaskel, S. Carbon Materials for Lithium Sulfur Batteries - Ten Critical Questions. *Chem. - A Eur. J.* **22,** 7324–7351 (2016).
10. Song J, Gordin ML, Xu T, Chen S, Yu Z, Sohn H, Lu J, Ren Y, Duan Y & Wang D. Strong lithium polysulfide chemisorption on electroactive sites of nitrogen-doped carbon composites for high-performance lithium-sulfur battery cathodes. *Angew. Chemie - Int. Ed.* **54,** 4325–4329 (2015).

CHAPTER 5: CONCLUSIONS AND FUTURE RECCOMENDATION

5.1 SUMMARY

The main contribution of the present work is the utilization of low-valued biomass and biochar materials for high-value application in order to solve energy storage problem. This thesis work was performed focusing on two goals. First one was to investigate the applicability of activated biochars derived from inexpensive and abundant canola meal and Douglas-fir wood for the preparation of high-valued lithium-sulfur battery cathode composite. Protein-rich canola meal biomass was chosen to synthesize naturally nitrogen-rich activated biochar. Douglas-fir was selected as a biomass with low nitrogen content. The second goal was to utilize fast pyrolysis derived biochar for lithium-sulfur battery cathode composite. Fast pyrolysis biochar is obtained as a low-value byproduct of high-valued liquid fuel through fast pyrolysis of biomass. Some biomass derived carbons have been investigated for lithium sulfur battery already. However, fast pyrolysis derived biochar have rarely investigated for any battery application. Thus, our focus was on investigating the applicability of fast pyrolysis biochar for Li-S battery and to compare the performance with slow pyrolysis biochar and commercial conductive carbon black.

For achieving the goals, at first biochar and then, activated biochars were prepared from canola meal and Douglas-fir wood. Total four types of activated biochars were prepared from this two biomass such as CF-AB, CS-AB, DF-AB, and DS-AB. CF-AB and DF-AB are activated biochar derived from fast pyrolysis biochar of canola meal and Douglas-fir wood, respectively. CS-AB and DS-AB were the activated biochar derived from slow pyrolysis of canola meal and Douglas-

fir wood, respectively. Later based on the surface area and pore volume, CF-AB, CS-AB, and DF-AB activated biochars were used to synthesize S/C composite following melt-diffusion strategy at 155°C. For comparison, S/C composite was so synthesized following the same method using commercial conductive carbon black (CB). Samples were denoted as CF-AB-S, CS-AB-S, DF-AB-S, and CB-S. Additionally, CF-AB-S was washed with toluene to remove the sulfur that existed on the surface of CF-AB-S composite and developed another composite named as CF-AB-S-T. Physical, chemical and electrochemical characterization was performed to evaluate characteristics and performance of the samples. Key findings of the research are summarized as follows:

- Nitrogen-doped activated biochar from protein-rich canola meal was successfully prepared in this thesis work. Here, CF-AB and CS-AB contains 0.8 and 1.2% nitrogen. However, due to activation using highly corrosive KOH and at high temperature (800°) the nitrogen content reduced from 5.79% (of canola meal) to 0.34 and 1.02% in activated biochar.
- Activated biochar prepared from fast pyrolysis biochar have a significantly higher surface area in comparison to the activated biochar prepared from slow pyrolysis biochar. CF-AB and DF-AB have a specific surface area of 3355 and 3277 $m^2 g^{-1}$, whereas, CS-AB and DS-AB have 1655 and 1045 $m^2 g^{-1}$ of specific surface area.
- The total pore volume of the activated biochar prepared from fast pyrolysis biochars is also significantly higher than the activated biochar prepared from slow pyrolysis biochar. CF-AB and DF-AB have a total pore volume of 1.58 and 1.49 $cm^3 g^{-1}$ respectively, whereas, CS-AB and DS-AB have 0.80 and 0.53 $cm^3 g^{-1}$ respectively. All the four activated biochars were micropore-rich. However, Douglas-fir wood derived activated biochars have higher mesopores than the canola meal derived activated biochars.

- Total five S/C composite cathodes (such as CF-AB-S, CF-AB-S-T, CS-AB-S, DF-AB-S, and CB-S) were evaluated in 2032 coin cell setup where lithium chip was anode and S/C composite was the cathode. Table 5.1 compares the four activated biochar derived cathode composite with previously published research works based on the initial discharge capacity and sulfur loading in the cathode composite Table 5.1 indicates that the cathode composite prepared in this thesis work exhibited comparable initial discharge capacity and high sulfur loading. Among them, CF-AB-S-T exhibited highest initial discharge capacity of 1507 mAh g^{-1} with 39% of sulfur loading.
- The composite cathodes prepared from activated biochar in this thesis work have exhibited their eligibility as the cathode composite of Li-S cell up to 40 cycles and, even at a high current density of 2 C. The CV plot up to first 11 cycles also exhibited characteristics of typical Li-S battery CV plot. This indicates that the prepared cathode composite prepared using activated biochars had the potential to be considered as an inexpensive, abundant and sustainable replacement of conventional expensive porous materials such as graphene oxide, carbon nanotube and ordered mesoporous carbon CMK-3.

Table 5.1: Electrochemical performance of Li-S cells based on biomass derived carbon

Biomass Source	Initial Discharge Capacity	S% in S/C composite	Ref
Rice husk	1352 mAh g^{-1} at 0.1 C	23	1
Sisal fibers	1050 mAh g^{-1} at 0.05 C	60	2
Soybean hulls	1231 mAh g^{-1} at 0.05 C	63.7	3
Soybean meal	1185 mAh g^{-1} at 0.2 C	64.5	4
Bamboo	1262 mAh g^{-1} at 0.1 C	50	5

Canola meal (CF-AB-S-T)	1507 mAh g^{-1} at 0.05 C	39	This work
Canola meal (CF-AB-S)	1222 mAh g^{-1} at 0.05 C	66.2	This work
Canola meal (CS-AB-S)	1037 mAh g^{-1} at 0.05 C	49.3	This work
Douglas-fir wood (DF-AB-S)	1107 mAh g^{-1} at 0.05 C	51.8	This work

5.2 FUTURE DIRECTIONS

Activated biochar prepared from canola meal and Douglas-fir have been investigated for any battery application for the first time. Also, it is experimentally proven that activated biochar prepared from fast pyrolysis biochar offers significantly better physical characteristics than slow pyrolysis biochar. This study helps to build a bridge between sustainable and inexpensive carbon source for high-valued energy storage application. The knowledge gained from this thesis work would be beneficial to investigate further and explore the possibility of low-valued biomass and biochar for further development of Li-S cells and other high-valued applications. The following directions are recommended for future investigations.

- Biomass exploration

  This study was conducted using canola meal and Douglas-fir wood biomass. Nitrogen-doped activated biochar was prepared from protein-rich canola meal. There are other abundant biomass sources are available with high protein content (such as algae, food waste or poultry litter), which also can be utilized as natural nitrogen sources for activated biochar.

- Altering biochar production methods

In this study, only fast and slow pyrolysis biochar were investigated. Future work can perform to the preparation of activated biochar from canola meal and Douglas-fir using gasification, hydrothermal liquefaction or microwave pyrolysis char.

- Altering activation methods and process temperature

  This study was focused on activation using potassium hydroxide at 800°C. Zinc chloride was only performed for fast pyrolysis canola meal biochar. Further studies can be conducted to understand the effect of other activation methods (such as carbon dioxide or phosphoric acid) and temperature on activated biochar properties.

- Optimization of sulfur loading on cathode composite

  The sulfur loading can be optimized further to improve the performance of the prepared Li-S cells. In this thesis work, CF-AB was investigated for 66% and 39% sulfur, whereas CS-AB and DF-AB have been studied for around 50% sulfur. Further investigation with 30, 40 and 60% sulfur loading for CS-AB and DF-AB can be performed to find out the optimum sulfur loading at which CS-AB and DF-AB activated biochar based composite exhibit their highest performance.

- Longer cycles operation

  This study was not focused on performing longer charge-discharge cycles. Further investigation can be carried out for the longer cycle to evaluate the viability of the prepared cells for commercial application.

- Other application of prepared activated biochar

  This study was focused on utilizing the prepared activated biochar for Li-S battery only. However, due to the ultra-high surface area and pore volume of the activated biochars (especially, CF-AB and DF-AB), this activated biochar could also show excellent

performance in other applications such as supercapacitors, capacitive deionization (CDI) and adsorbents.

References

1. Vu, D.-L., Seo, J.-S., Lee, H.-Y. & Lee, J.-W. Activated carbon with hierarchical micro–mesoporous structure obtained from rice husk and its application for lithium–sulfur batteries. *RSC Adv.* **7,** 4144–4151 (2017).
2. Raja, M., Angulakshmi, N. & Stephan, A. M. Sisal-derived activated carbons for cost-effective lithium–sulfur batteries. *RSC Adv.* **6,** 13772–13779 (2016).
3. Zhu, Y. *et al.* Hierarchical porous carbon derived from soybean hulls as a cathode matrix for lithium-sulfur batteries. *J. Alloys Compd.* **695,** 1–7 (2016).
4. Chen, F., Yang, J., Bai, T., Long, B. & Zhou, X. Biomass waste-derived honeycomb-like nitrogen and oxygen dual-doped porous carbon for high performance lithium-sulfur batteries. *Electrochim. Acta* **192,** 99–109 (2016).
5. Gu, X. *et al.* Microporous bamboo biochar for lithium-sulfur batteries. *Nano Res.* **8,** 129–139 (2014).

Appendix A

Theoretical Calculations

A.1 Theoretical cell voltage of Li-S battery

Standard potential of a cell or theoretical cell voltage can be calculated from the standard electrode potentials as follows[1]:

Anode (oxidation potential) + cathode (reduction potential) = standard cell potential

For Li-S battery, overall cell reaction[2] during discharge is

$$2Li + S \rightarrow 2Li_2S$$

Anodic (oxidation potential)[1]	$Li \rightarrow Li^+ + e^-$	- (-3.01 V)
Cathode (reduction potential)[1]	$S_8 + 16e \rightarrow 8S^{2-}$	-0.48 V
Theoretical Voltage or Standard Cell Potential =		2.53 V

A.2 Theoretical Capacity of Li-S battery

The theoretical capacity of a cell is expressed as the total quantity of electricity involved in the electrochemical reaction. It can be determined by the amount of active materials in the cell. It is defined in terms of coulombs or ampere-hours. The ‘‘ampere-hour capacity’’ of a battery is directly related to the quantity of electricity obtained from the active materials. Theoretically, 1 gram-equivalent weight of material will deliver 96,487 C or 26.8 Ah. A gram-equivalent weight

is an atomic or molecular weight of the active material in grams divided by the number of electrons involved in the reaction.

The theoretical specific capacity of a battery electrode is typically reported in mAh g^{-1} and can be calculated from[1]:

$$Q = \frac{nF}{M_{electrode}}$$

Here,

F is the Faraday constant which is the magnitude of electric charge per mole of electrons.

Faraday's constant $F = e N_A$

e is the elementary charge or the magnitude of the charge of an electron

$e \approx 1.6021766 \times 10^{-19}$ C

N_A is the Avogadro constant = $N_A \approx 6.022141 \times 10^{23}$ mol^{-1}

Avogadro's number is defined as the number of elementary particles (molecules, atoms, compounds, etc.) per mole of substance.

$$F = e N_A = 96485.33289 \text{ C mol}^{-1} = 26.8 \text{ Ah mol}^{-1}$$

n = number of electron associated with the reaction

$M_{electrode}$ = the molecular weight of the electrode in g mol^{-1}

Theoretical specific capacity of lithium anode ($M_{lithium}$ = 6.94 and n=1),

$$Q_{Li} = \frac{1 \times 26.8}{6.94} = 3.862 \text{ Ah g}^{-1}$$

Theoretical specific capacity of sulfur cathode (M_{sulfur} = 32.0 and n=2):

$$Q_S = \frac{2 \times 26.8}{32} = 1.675 \text{ Ah g}^{-1}$$

The theoretical capacity of an electrochemical cell, based only on the active materials participating in the electrochemical reaction is calculated from the equivalent weight of the reactants. Hence, the theoretical capacity of the Li/S cell can be calculated as follows:

$$2Li + S \rightarrow 2Li_2S$$

(3.862 Ah g^{-1}) (1.675 Ah g^{-1})

0.259 g/Ah + 0.598 g/Ah = 0.857 g/Ah or 1.167 Ah g^{-1}

2.06 Ah cm^{-3} 3.34 Ah cm^{-3}

0.485 cm^3/Ah + 0.299 cm^3/Ah = 0.784 cm^3/Ah or 1.275 Ah cm^{-3}

Thus, the theoretical capacity of the Li/S cell is 1.167 Ah g^{-1} or 1167 mAh g^{-1}

A.3 Theoretical Energy

The theoretical energy of a specific electrochemical system can be calculated by

Theoretical energy (Watthour) = Theoretical voltage (V) × Theoretical capacity (Ah)

In the Li/S cell, the standard potential is considered[2–4] as either 2.2V or 2.15V. Theoretical watt-hour (Wh) capacity per gram of active material (theoretical gravimetric specific energy or theoretical gravimetric energy density) is:

Theoretical Specific Energy (Wh g^{-1}) = 2.15 V × 1.167 Ah g^{-1} = 2.5 Wh g^{-1} or 2500 Wh kg^{-1}

Theoretical Specific Energy (Wh cm^{-3}) = 2.15 V × 1.275 Ah cm^{-3} = 2.74 Wh cm^{-3} or 2741 Wh l^{-1}

A.4 Calculation for sulfur loading on porous carbons [5]

Density of lithium sulfide (Li_2S) is 1.66 g cm^{-3}

If total pore volume of porous carbon is PV cm^3 g^{-1}

So, 1 g of porous carbon can accommodate 1.66 × PV g of Li_2S

Molecular weight of

Lithium is 6.94 g/mol

Sulfur is 32.0 g/mol

Li_2S is 45.88 g/mol

In Li_2S, sulfur is about 0.6975%, and Lithium is 0.3025%

So, maximum sulfur loading on porous carbon = 1.66 × PV × 0.6975 g

Table A.1: Maximum sulfur loading on activated biochars

Sample	Pore Volume (cm^3 g^{-1})	Maximum Sulfur Loading (for 1 g of activated biochar)
CF-AB	1.58	1.83
CS-AB	0.80	0.93
DF-AB	1.49	1.73
DS-AB	0.53	0.61

References

1. Linden, D. & Reddy, T. B. Handbook of battery. (2001).
2. Manthiram, A., Fu, Y., Chung, S., Zu, C. & Su, Y. Rechargeable Lithium − Sulfur Batteries. *Chem. Rev.* **114,** 11751–87 (2014).
3. Bruce, P. G., Freunberger, S. a., Hardwick, L. J. & Tarascon, J.-M. Li–O2 and Li–S batteries with high energy storage. *Nat. Mater.* **11,** 172–172 (2011).
4. Xu, R., Lu, J. & Amine, K. Progress in Mechanistic Understanding and Characterization Techniques of Li-S Batteries. *Adv. Energy Mater.* **5,** 1–22 (2015).
5. Ji, X., Lee, K. T. & Nazar, L. F. A highly ordered nanostructured carbon-sulphur cathode for lithium-sulphur batteries. *Nat. Mater.* **8,** 500–506 (2009).

Appendix B

B.1 Canola Meal Derived Activated Biochar Prepared Using $ZnCl_2$

Another activated biochar material has been prepared using $ZnCl_2$ as the chemical activation agent. Fast pyrolysis derived canola meal biochar have been utilized to prepared $ZnCl_2$ activated biochar (CF-ABZ) at 600°C activation temperature.

Surface area and porosity of CF-ABZ have shown in Figure B.1. CF-ABZ has a specific surface area of 2166 m^2 g^{-1} with 1.60 cm^3 g^{-1} total pore volume (Figure B.1). From Figure B.1a, CF-ABZ has a significant amount of mesopores (40% of total pore volume) and wide pore size range. Figure B.1c shows the presence of hysteresis in the isotherm of CF-ABZ which is usually associated with capillary condensation in mesopore structures[1]. CF-ABZ shows the H4 type of isotherm which is a characteristic isotherm of narrow slit-like pores of irregular shape and broad pore size distribution[1]. Thus, in comparison with other prepared activated biochar that has mostly micropores and small mesopores, CF-ABZ have a different structure with a wide range of mesopores. Table B.1 presents elemental analysis data that indicates the highest nitrogen content (5.9%) among all the activated biochar that is prepared in this current study. CF-ABZ could retain high nitrogen content since it was prepared at lower temperature (600°C) than other activated biochars.

Table B.1: Elemental analysis of CF-ABZ

Sample	N (%)	C (%)	H (%)	S (%)	Ash (%)
CF-ABZ	5.9 ± 0.01	71.39 ± 0.63	3.50 ± 0.09	0.67 ± 0.09	6.23 ± 0.12

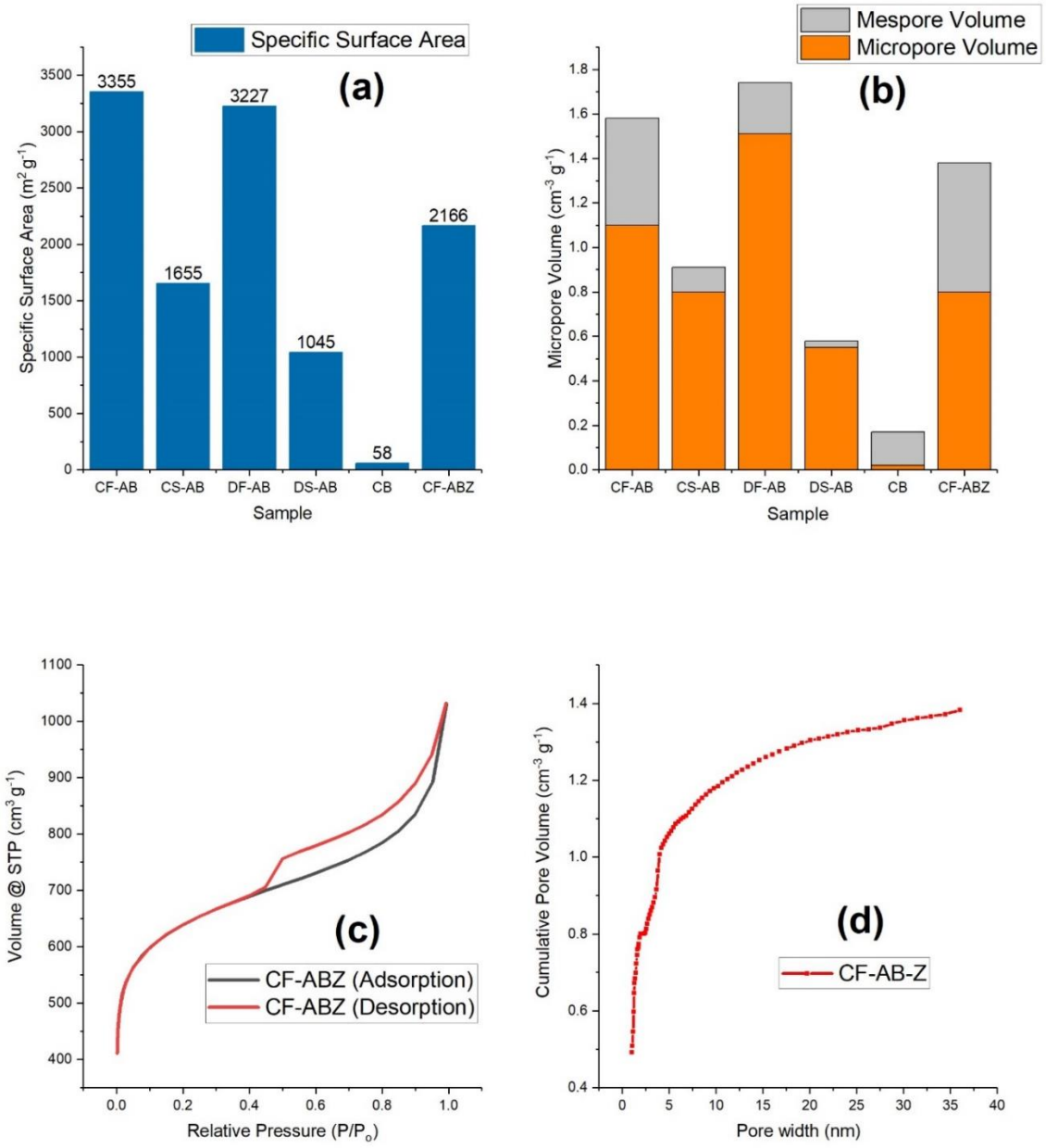

Figure B.1: (a) Surface area, (b) pore volume (c) N_2 adsorption-desorption isotherms and (d) pore size distribution of CF-ABZ activated biochar

References

1. Sing, K. S. W. *et al.* Reporting physisorption data for gas/solid systems with special reference to the determination of surface area and porosity (Recommendations 1984). *Pure Appl. Chem.* **57,** 603–619 (1985).

Appendix C

Troubleshooting

During the process of completing thesis work, numerous difficulties had to be faced for different reasons. This Appendix involves the cause of some challenges and the way to solve the problem.

C.1 Difficulties faced during biochar activation process

Biochar preparation and activation were the first steps of this thesis. Surface area and porosity analysis were chosen to determine successful activation of biochar. At an early stage of thesis work, two major difficulties had to resolve to obtain highly porous activated biochar, and proper surface area and porosity measurement.

- Reactor setup for activation

  Douglas-fir wood biomass was used at an earlier stage to prepare activated biochar using both fluidized bed reactor (Figure 3.3) and fixed bed reactor (Figure 3.2). In the case of fluidized bed reactor without fluidization media (such as sand), biochar and KOH mixture would stay at the bottom of the reactor where the temperature would not reach above 200°C. Thus, smaller sized fixed bed reactor was used later. However, when the reactor was setup vertically, the bottom part of the reactor tube would stay on the edge of the furnace, and the temperature would not reach near the target high temperature, and thus, the activation would not work. Later, quartz wool was placed in the reactor tube to restrict the biochar and KOH mixture from reaching the bottom. However, quartz wool would get melted and stuck in the tube due to the presence of KOH at high temperature (800°C). The

agglomeration of quartz wool would block the nitrogen flow. Stainless steel mesh (bought from McMaster-Carr) was used in a cone shape to restrict the mixture from reaching to low-temperature zone.

- Surface area and porosity measurement

  At an early stage of the thesis work, difficulties were also faced with surface area and porosity measurement result of activated biochars. This was due to using 20 point method and backfill degassing method. Insufficient degassing of activated biochar samples led to the unusual type of isotherms for activated biochar. This problem was resolved by using 60 adsorption and desorption points, and pressure controlled heating in a vacuum state for degassing.

C.2 Difficulties faced during the coin cell assembly process

At an early stage, more than 75% assembled cells turned into dead cell due to some reasons. Later throughout the thesis work process, these difficulties were resolved.

- Size of lithium chip anode

  Due to larger lithium chip anode of 15.6 mm in 2032 coin cell, anode would touch the conductive casing part and result in dead cells. This was resolved by punching out 11 mm lithium chip diameter instead of 15.6 mm.

- Loose connection

  Due to using only one spacer on the 2032 coin cell, the cell connection was poor and resulted in dead cells often. This was resolved by putting two spacers on the anode side and one spacer on the cathode side.

- Separator diameter

  Another reason for the dead cell was due to the smaller size of the separator (19 mm) which was resolved by using two separator of 20 mm size.